Multimaterial Fiber Electronics

by

Guillaume Lestoquoy

B.Sc., École Polytechnique, 2008
M.Sc., Materials Science, École Polytechnique, 2009
M.Sc, Electrical Engineering and Computer Science, MIT, 2012

Submitted to the Department of Electrical Engineering and Computer Science in partial fulfillment of the requirements for the degree of

Doctor of Philosophy in Electrical Engineering and Computer Science

at the

MASSACHUSETTS INSTITUTE OF TECHNOLOGY

February 2014

Author .....
Department of Electrical Engineering and Computer Science
January 15, 2014

Certified by .....
Professor Yoel Fink
Professor of Materials Science and Engineering
Professor of Electrical Engineering and Computer Science
Thesis Supervisor

Accepted by .....
Professor Leslie A. Kolodziejski
Chairman, Department Committee on Graduate Students

Multimaterial Fiber Electronics

by

Guillaume Lestoquoy

Submitted to the Department of Electrical Engineering and Computer Science on January 15, 2014, in partial fulfillment of the requirements for the degree of Doctor of Philosophy in Electrical Engineering and Computer Science

Abstract

As the number of materials that are thermally-drawable into fibers is rapidly expending, numerous new multimaterial fiber architectures can be envisioned and fabricated. High-melting temperature metals, compound materials, composite, conductive or ferroelectric polymers: the broad diversity of these materials' nature and properties, combined with various post-fabrication treatments recently developed (poling, annealing, injection, coating, capillary breakup), enable the making of novel in-fiber, stand-alone-fiber and fiber-array devices. In this thesis, we demonstrate a wide variety of novel multimaterial fiber capabilities at all these levels, focusing specifically on new electronic functions.

First, the implementation of conductive polymer as in-fiber current buses is shown to enable distributed light sensing and modulation along a single fiber, by inducing transmission-line effects in d.c. and a.c. operation. Next, the design and operation of a photosensing fiber specially treated to detect explosives is presented, and the sensitivity of this fiber device is shown to meet state-of-the-art industry standards. A novel large-interface-area design for dielectric fibers is then presented, which enables both energy storage in flexible fiber capacitors as well as enhanced acoustic transduction in piezoelectric fibers. The flexibility as well as the assembly into arrays of the latter are shown to enable the shaping of a pressure field in all three dimensions of space. Finally, a novel thermal-gradient capillary breakup process for silica-based fibers is shown, enabling the fabrication of silicon-in-silica micro spheres and rectifying devices.

Taken as a whole, these new capabilities greatly expand the breadth of functionality of multimaterial fibers, further paving the way towards highly multifunctional, wholly integrated electronic fiber devices and fabrics that can collect, store and transduce energy in all of its forms.

Thesis Supervisor: Professor Yoel Fink
Title: Professor of Materials Science and Engineering
Professor of Electrical Engineering and Computer Science

Acknowledgments

First of all, my gratitude goes to Pr. Yoel Fink, who was not simply my research supervisor during these years, but actually the person who inspired me to join MIT in the first place: a decision that has forever changed the course of my life and career. He has been a source of inspiration, support and motivation, has taught me how to make meaningful contributions in a great variety of contexts, and also how to convey the importance of our work to the rest of the world. I then want to thank Pr. Fabien Sorin, who first mentored me as an intern but who quickly became an amazing friend. Likewise, Dr. Noemie Chocat, Dr. Sylvain Danto, Dr. Lei Wei and Benjamin Grena have also been much more than just great colleagues. Their kindness, sense of humor and energy is often what kept me motivated and going, and these friendships are among of the greatest treasures I found at MIT.

Throughout the years I have worked within the Fibers@MIT group, I have been fortunate to work with many other highly-talented labmates who have all always been very kind and supportive: Dr. Zheng Wang, Dr. Sasha Stolyarov, Dr. Ofer Shapira, Dr. Dana Shemuly, Dr. Shunji Egusa, Dr. Xiaoting Jia, Dr. Nick Orf, Dr. Daosheng Deng and of course my fellow graduate students Chong Hou, Jeff Clayton, Andres Canales, Michael Rein and Tara Sarathi. Last, Tina Gilman was the kindest and most caring person I got to meet at MIT, and deserve my warmest thanks.

Many good friends have allowed to make my move from France to Boston a very pleasant adventure but my special thanks go to Randi, Andy, Sam, Fabien, Tilke, Beth, Yann and Tom with whom I have shared the nicest place I have ever lived in.

While far away, my family deserves the deepest thanks: my mother, father and brother have always believed in me and helped me find my way, and I am forever grateful to them. To my late grandmother Denise, who foresaw so much, too.

Last and most importantly, I am infinitely thankful to Anna, whose path has crossed mine at the very beginning of this journey, and whose love, support and kindness has made these years the best of my life. May our paths never part again.

Contents

Introduction

For now over a decade, a growing research effort has been focused on the development of multi-material fibers and has led to the demonstration of numerous functional designs including an ever-expanding variety of materials and increasingly complex fiber structures [1, 2, 3, 4, 5, 6, 7, 8, 9, 10]. Fibers can sense, emit, transport and transduce signals in light, electric, thermal or acoustic form. Increasingly, multimaterial fibers are also considered as reactors in which physical or chemical transformations can occur during their fabrication or after, so as to generate new structures [11, 12] and synthesize materials [13, 14].

While tremendous progress has been achieved since the idea of fabricating multimaterial fiber devices has emerged, a lot of the potential of this device fabrication approach remains untapped. In this thesis we describe the implementation of original fiber designs, materials, integration schemes and treatments with one common goal: the understanding and harnessing of how electrons flow in electronic fibers to demonstrate new functions, structures and performances. The work was articulated around several questions, sometimes asked independently and sometimes simultaneously:

- Can fibers inherently uniform along their axis resolve or modulate localized signals?
- Can functions relying on large interfaces between materials, such as acoustic transduction and energy storage be efficiently implemented in a fiber?
- Can collective effects be harnessed to develop fabrics or fiber arrays functionality?
- Can fibers' unique aspect ratio and mechanical flexibility be exploited to shape signals?
- Can we create electronic junctions involving high-melting-temperature semiconducting materials in fibers? Can we harness in-fiber capillary instabilities for that same purpose?

In Chapter 1, we present the first implementation of transmission line effects within a multi-material fiber, so as to enable a degree of axial resolution of the light distribution impinging on a photodetecting fiber. We show how an ingenuous fiber design built upon structures and materials successfully drawn in the past enables the produced fiber to retrieve the position of several incident beams of light. We then take this new transmission line approach to the a.c. regime in a different context, presented in Chapter 2. There, we show how the proper implementation of resistive current buses along an in-fiber liquid-crystal-filled channel enables the axial modulation of light either going through the fiber or being emitted radially from the fiber center.

In Chapter 3, we describe a design process and the following experimental steps taken to fabricate a peroxide-sensing fiber, that can analyze air or gas as it is pumped along the fiber hollow core. The application for explosive sensing is of the utmost importance and we show how the design process and optimized operation lead to detection results on par with the current state-of-the-art technologies available.

In Chapter 4 we functionalize two unique features of fiber devices: their flexibility and their easy assembly into arrays. After enhancing a previously demonstrated in-fiber piezoelectric structure and carefully characterizing the obtained fiber acoustic and electrical behaviors, we show how an array of such fibers can be used to direct sound in space, while a bent fiber can focus the sound at a chosen distance. We then take the structure enhancement one step further in Chapter 5 and demonstrate multilayered electrode-to-dielectric interfaces in fiber capacitors.

In Chapter 6[1], we demonstrate a novel fabrication path towards silicon microdevices. Inspired by the recent breakthroughs in controlled in-fiber capillary-instability-induced [12], we developed a thermal-gradient induced breakup process suitable for high-melting-temperature, in-silica-fiber materials. We show how the new process enables us to obtain smaller spheres than conventional uniform heating, and how spheres size obtained from a given fiber can be varied. We then take it one step further by exploiting this new breakup method to fabricate in-silica silicon p-n junctions. A silica fiber containing a p-doped and a n-doped silicon filaments is successfully processed into the first ever bi-spherical p-n junction, establishing the potential for this new microelectronic devices fabrication method.

[1]Part of the content of this chapter has previously been published in *Silicon-in-silica spheres via axial thermal gradient in-fibre capillary instabilities.* Nat. Commun. 4:2216 doi: 10.1038/ncomms3216 (2013).

Finally, in Chapter 7, we briefly present suggestions for future work, both within the high- and low- temperature drawing frameworks. Indeed, significant opportunities have been discovered while conducting the work presented in this thesis, and the ideas proposed in this final chapter all have in common to be within reasonable reach and to offer great potential for fiber electronics. We then conclude this thesis with our final remarks.

Chapter 1

Resolving optical illumination distributions along an axially symmetric photodetecting fiber

1.1 Abstract

Photodetecting fibers of arbitrary length with internal metal, semiconductor and insulator domains have recently been demonstrated. These semiconductor devices display a continuous translational symmetry which presents challenges to the extraction of spatially resolved information. Here, we overcome this seemingly fundamental limitation and achieve the detection and spatial localization of a single incident optical beam at sub-centimeter resolution, along a one-meter fiber section. Using an approach that breaks the axial symmetry through the construction of a convex electrical potential along the fiber axis, we demonstrate the full reconstruction of an arbitrary rectangular optical wave profile. Finally, the localization of up to three points of illumination simultaneously incident on a photodetecting fiber is achieved.

1.2 Introduction

Optical fibers rely on translational axial symmetry to enable long distance transmission. Their utility as a distributed sensing medium [15, 16, 17] relies on axial symmetry breaking either through the introduction of an apriori axial perturbation in the form of a bragg gratings [18], or through the use of optical time (or frequency) domain reflectometry techniques [19, 20] which measure scattering from an adhoc axial inhomogeneitie induced by the incident excitation. These have enabled the identification and localization of small fluctuations of various stimuli such as temperature [21, 22, 23] and stress [24, 25] along the fiber axis. Due to the inert properties of the silica material, most excitations that could be detected were the ones that led to structural changes, importantly excluding the detection of radiation at optical frequencies. Recently, a variety of approaches have been employed, aimed at incorporating a broader range of materials into fibers [26, 27, 28, 29, 30, 31, 32, 3, 7]. In particular, multimaterial fibers with metallic and semiconductor domains have presented the possibility of increasing the number of detectable excitations to photons and phonons [3, 7, 33, 34, 35, 8, 9], over unprecedented length and surface area. Several applications have been proposed for these fiber devices in imaging [35, 8], industrial monitoring [4, 5], remote sensing and functional fabrics [7, 33].

So far however, the challenges associated with resolving the intensity distribution of optical excitations along the fiber axis have not been addressed. Here we propose an approach that allows extraction of axially resolved information in a fiber that is uniform along its length without necessitating fast electronics or complex detection architectures. We initially establish the axial detection principle by fabricating the simplest geometry that supports a convex potential profile designed to break the fiber's axial symmetry. Then, an optimal structure which involves a hybrid solid-core/thin-film cross-sectional design is introduced that allows to impose and vary convex electrical potential along a thin-film photodetecting fiber. We demonstrate the localization of a point of illumination along a one-meter photodetecting fiber axis with a sub-centimeter resolution. Moreover, we show how the width of the incoming beam and the generated photoconductivity can also be extracted. Finally, we demonstrate the spatial resolution of three simultaneously incident beams under given constraints.

1.3 Principle of our approach

1.3.1 Principle of photodetection with fibers

Photodetecting fibers typically comprise a semiconducting chalcogenide glass contacted by metallic electrodes and surrounded by a polymer matrix [3, 7, 33]. These materials are assembled at the preform level and subsequently thermally drawn into uniform functional fibers of potentially hundreds of meters in length, as illustrated in Figure 1.1.

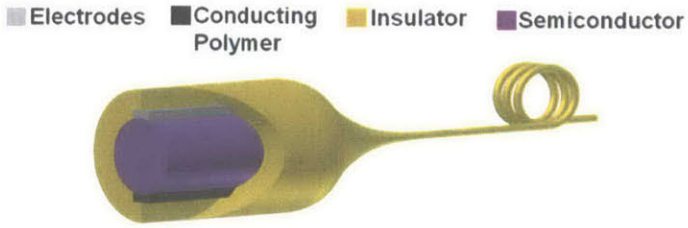

Figure 1.1: 3D Schematic of the multimaterial fiber thermal drawing fabrication approach.

An electric potential $V(z)$ across the semiconductor can be imposed along the fiber length by applying a potential drop V_0 at one end as depicted in Figure 1.2.

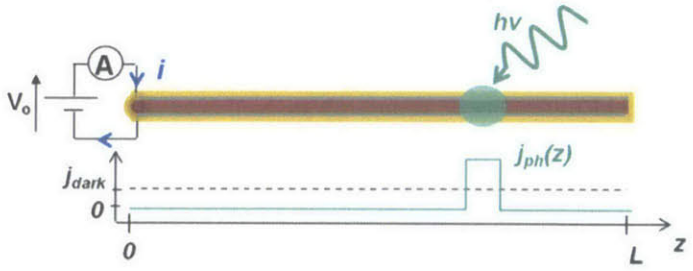

Figure 1.2: Schematic of a connected photodetecting fiber with an illumination event. The graph represents the linear current density in the dark and under the represented illumination.

As a result, a linear current density j_{dark} is generated in the semiconductor in the dark, between the electrodes. When an incoming optical wave front with an arbitrary photon flux distribution $\Phi_0(z)$ is incident on a fiber of total length L, the conductivity is locally changed and a photo-current (total current measured minus the dark current) is generated due to the photoconducting effect in semiconductors, as illustrated in Figure 1.2. The measured photo-

current in the external circuitry is the sum of the generated current density $j_{ph}(z)$ along the entire fiber length:

$$i_{ph} = C \int_0^L V(z)\sigma_{ph}(z)dz \tag{1.3.1}$$

where C depends on the materials and geometry and is uniform along the fiber axis, and σ_{ph} is the locally generated film photo-conductivity that depends linearly on $\Phi_0(z)$ in the linear regime considered [34, 35, 8, 36, 37, 38] . Note that for simplicity the integrations on the other cylindrical coordinates r and θ are not represented. Also, we neglect the diffusion of generated free carriers along the fiber axis since it occurs over the order of a micrometer, several orders of magnitude lower than the expected resolution (millimeter range).

1.3.2 Limitations and proposed solution

For the photodetecting fibers considered so far, the conductivity of the semiconductor in the dark and under illumination has been orders of magnitude lower than the one of the metallic electrodes. These electrodes could hence be considered equipotential, and $V(z) = V_0$ along the fiber axis over extend lengths. As a result, j_{dark} is also uniform as depicted on the graph in Figure 1.2. Moreover, the photo-current measured in the external circuitry integrates the photo-conductivity distribution $\sigma_{ph}(z)$ along the fiber length. This single, global current measurement does not contain any local information about the incident optical intensity distribution along the fiber axis. In particular, even the axial position of a single incoming optical beam could not be reconstructed. To alleviate this limitation, we propose an approach that breaks the axial symmetry of this fiber system and enables to impose various non-uniform electric potential distributions along the fiber axis. By doing so, we can generate and measure several global photo-currents i_{ph} where the fixed and unknown distribution $\sigma_{ph}(z)$ is modulated by different known voltage distributions $V(z)$. We will then be able to access several independent photo-current measurements from which information about the intensity distribution along the fiber axis will be extracted, as we will see.

To controllably impose a non-uniform electrical potential profile $V(z)$, we propose to replace one (or both) metallic conducts by a composite material that has a higher electrical resistivity. This electrode, or resistive channel, can no longer be considered equipotential and

the potential drop across the semiconductor will vary along the fiber axis. An ideal material for this resistive channel was found to be a composite polymer recently successfully drawn inside multimaterial fibers [9], that embeds carbon black nanoparticles inside a Polycarbonate matrix (hereafter: conducting polycarbonate or CPC) [39]. The CPC resistivity, ρ_{CPC} (1-10 $\Omega.m$ as measured post-drawing), lies in-between the low resistivity of metallic elements (typically 10^{-7} $\Omega.m$) and the high resistivity of chalcogenide glasses (typically $10^{6} - 10^{12}$ $\Omega.m$) used in multimaterial fibers. It is very weakly dependent on the optical radiations considered so that it will not interfere with the detection process.

1.3.3 Convex potential

To validate this approach we first demonstrate the drawing compatibility of these materials. We fabricated a photodetecting fiber with a semiconducting chalcogenide glass core (of composition $As_{40}Se_{50}Te_{10}$) contacted by one metallic electrode ($Sn_{63}Pb_{37}$) and by another conduct made out of the proposed CPC composite. A Scanning Electron Microscope (SEM) micrograph of the resulting fiber cross-section is shown in Figure 1.3 that demonstrate the excellent cross-sectional features obtained.

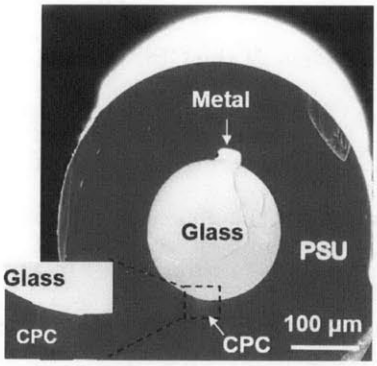

Figure 1.3: Scanning Electron Microscope micrograph of the fiber cross-section (inset: zoom-in on the contact between the core and the CPC electrode).

To first theoretically analyze this new system, we depict its equivalent circuit in Figure 1.4. The semiconducting core can be modeled as multiple resistors in parallel, while the CPC channel is comprised of resistors in series.

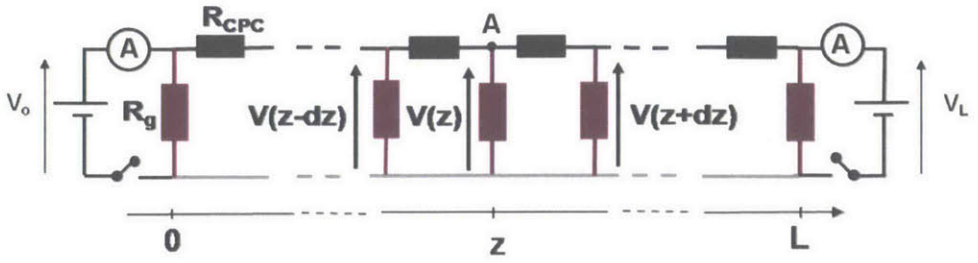

Figure 1.4: Schematic of the fiber system's equivalent circuit.

To find the voltage distribution $V(z)$ in this circuit, we can apply Kirchoff's laws at point A:

$$\frac{V(z)-V(z-dz)}{R_{CPC}} = \frac{V(z+dz)-V(z)}{R_{CPC}} - \frac{V(z)}{R_g} \quad , \text{or} \quad \frac{\partial^2 V}{\partial z^2} = \frac{R_{CPC}}{R_g dz^2} V(z) \tag{1.3.2}$$

or simply:

$$\frac{\partial^2 V}{\partial z^2} = \frac{V(z)}{\delta(z)^2} \tag{1.3.3}$$

with:

$$\delta(z) = \sqrt{\frac{\rho_g(z)}{\rho_{CPC}} \frac{\pi}{2} S_{CPC}} \tag{1.3.4}$$

where $R_{CPC} = \rho_{CPC} \dfrac{dz}{S_{CPC}}$ is the resistance of the CPC channel over an infinitesimal distance dz, S_{CPC} being the surface area of the CPC electrode in the fiber cross-section. Similarly, R_g is the resistance of a slab of cylindrical semiconducting core of length dz whose value depends on the glass geometry. The new parameter δ has the dimensionality of a length and is referred to as the characteristic length of the fiber system. It can be tuned by engineering the glass composition (hence changing ρ_g), as well as the structure and geometry of the fiber.

Two sets of boundary conditions can be defined for this system, as depicted in Figure 1.5: BC(1) where one fiber end ($z = 0$ *or* L) is brought to a potential $V^{BC(1)}(0) = V_0$ while the other ($z = L$ *or* 0) is left floating, locally resulting in $\dfrac{\partial V^{BC(1)}}{\partial z} = 0$ since no accumulation of charges is expected; and BC(2) where we apply a voltage at both fiber ends, $V^{BC(2)}(0) = V_0$ and $V^{BC(2)}(L) = V_L$.

The two potential profiles can then be derived when δ is independent of z, and are given by two *convex* functions:

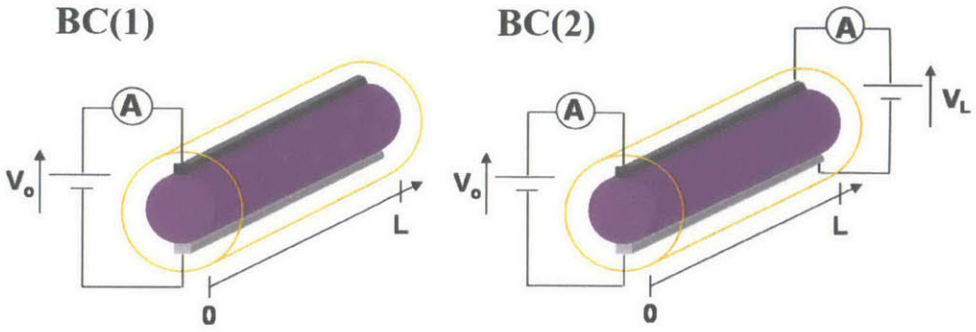

Figure 1.5: Schematic of the fiber contact for boundary conditions (1) (left) and (2) (right).

$$V^{BC1}(z) = \frac{V_0 \cosh\left(\frac{L-z}{\delta}\right)}{\cosh\left(\frac{L}{\delta}\right)} \tag{1.3.5}$$

$$V^{BC2}(z) = \frac{V_0 \sinh h\left(\frac{L-z}{\delta}\right) + V_L \sinh h\left(\frac{z}{\delta}\right)}{\sinh\left(\frac{L}{\delta}\right)} \tag{1.3.6}$$

1.3.4 Experimental results

To assess our model, we fabricated three fibers with different materials and structures. All fibers have one metallic electrode ($Sn_{63}Pb_{37}$ alloy) and one CPC electrode of same size. Two fibers have a solid-core structure like the one shown in Figure 1.3, with two different glass compositions from the chalcogenide system As-Se-Te, $As_{40}Se_{50}Te_{10}$ (referred to as AST_{10}) and $As_{40}Se_{42}Te_{18}$ (referred to as AST_{18}). The third fiber has a thin-film structure with a 500 nm layer of $As_{40}Se_{50}Te_{10}$ [34, 8]. This thin film structure is expected to have a very large characteristic length since its conductance is many orders-of-magnitude lower than the one of both metallic and CPC electrodes. In solid-core fibers however, δ should be of the order of the fiber length, inducing a significant variation in the potential profile. Separate measurement of the CPC electrode resistivity ($\rho_{CPC} = 1.4\Omega.m$ and $\rho_{CPC} = 1.2\Omega.m$ in pieces from the AST_{10} and AST_{18} fibers respectively) and the glass conductivities lead to expected δ values of 40 cm and 9 cm in the AST_{10} and AST_{18} fibers respectively, the higher conductivity of AST_{18} being responsible for the lower δ parameter [40].

We then cut a 60-cm-long piece from each fiber and made several points of contact on the CPC electrodes while contacting the metallic conduct at a single location. We applied a 50 V potential difference for both BC(1) and BC(2), and measured the potential drop between the contact points along the CPC channel and the equipotential metallic conduct, using a Keithley 6517A multimeter. The experiment was performed in the dark to ensure the uniformity of δ. The results are presented in Figure 1.6 where the data points are the experimental measurements while the curves represent the theoretical model derived above, fitted over δ.

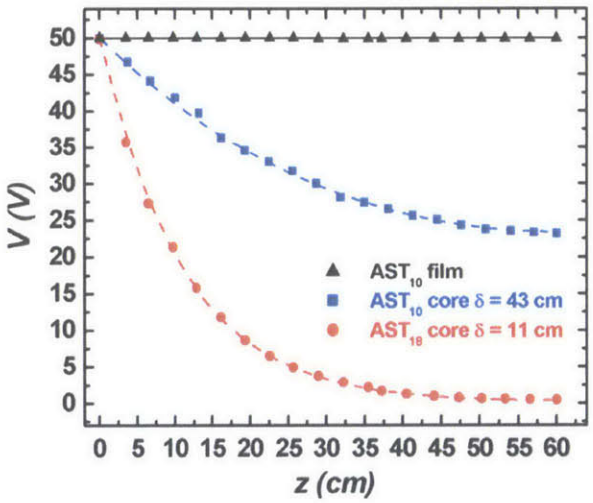

Figure 1.6: Experimental results (dots) and the fitted theoretical model (lines) of the voltage profile between the CPC electrode and the metallic conduct at different points along the fiber axis, when the fiber is under BC(1) with $V_0 = 50V$ and for different fibers: in black, AST_{10} thin-film; in blue, AST_{10} core and in red, AST_{18} core.

As we expected, the thin-film fiber maintains a uniform potential along its axis. For solid-core fibers, the fitting values (43 cm and 11 cm for BC(1), and 44 cm and 11 cm for BC(2) for AST_{10} and AST_{18}fibers respectively) match very well with the expected δ parameters given above. The discrepancy is due to errors in measuring the different dimensions in the fiber, and potential slight non-uniformity of the glass conductivity due to local parasitic crystallization during the fabrication process [10]. Noticeably, the δ values obtained for both boundary conditions are in excellent agreement, which strongly validates our model.

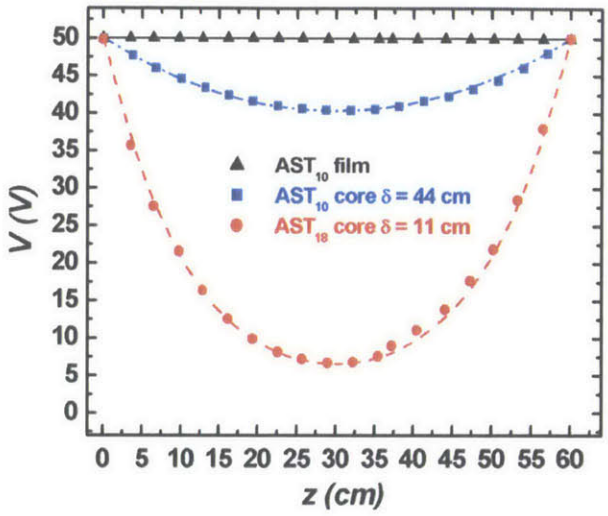

Figure 1.7: Same as Figure 1.6 but when the fiber is under BC(2) with $V_0 = V_L = 50V$.

1.4 Hybrid thin-film/solid-core fiber structure

1.4.1 Convex potential in the hybrid structure

Solid core fibers can hence support convex potential profiles that can be tuned using different glass compositions or fiber structure. When an optical signal is impingent on the fiber however, δ is no longer uniform as we considered earlier, since the glass resistivity is locally changed. This will in turn affect $V(z)$ that becomes an unknown function of the intensity distribution of the optical wave front. Moreover, thin-film structures are a more attracting system to work with in light of their better sensitivity and other advantages described in [34]. To address these observations we propose an hybrid structure that enables to impose convex potential distributions that remain unchanged under illumination, across a semiconducting thin-film that is used as the higher sensitivity detector. The fiber cross-section is shown in Figure 1.8, where a CPC electrode contacts both a solid-core and a thin-film structure.

The equivalent circuit is represented in Figure 1.9, where one can see that the two systems are in parallel. The drop of potential between the CPC channel and the metallic electrodes (both at the same potential) expressed in (1.3.2) now becomes: $V(\frac{1}{R_c} + \frac{1}{R_c})$ where R_c and R_f are the resistance of a slab of cylindrical semiconducting solid-core and thin-film respectively, of

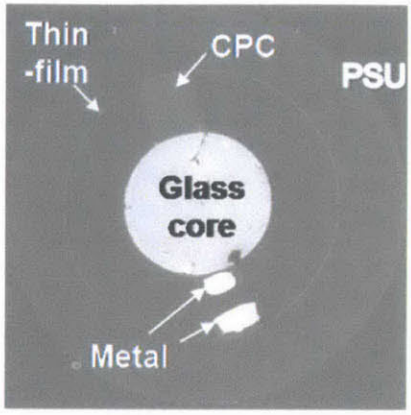

Figure 1.8: SEM micrograph of a fiber with the new thin-film/solid-core structure.

length dz. This leads to a new differential equation:

$$\frac{\partial^2 V}{\partial z^2} = V\left(\frac{1}{\delta_c^2} + \frac{1}{\delta_f^2}\right) \approx \frac{V}{\delta_c^2} \tag{1.4.1}$$

since δ_c and δ_f , the characteristic parameters for the solid-core and the thin-film respectively, verify $\delta_c << \delta_f$ as can be anticipated from earlier results. The potential distribution is hence imposed by the solid-core system, while the current flowing through the photoconducting film can be measured independently, thanks to the different metallic electrodes contacting the solid-core and the thin-film structures. Similar boundary conditions can be imposed to the solid-core sub-system as before.

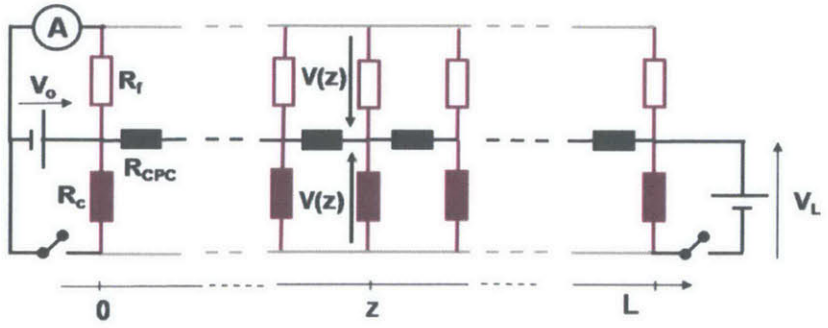

Figure 1.9: Schematic of the equivalent circuit of the hybrid-fiber with electrical connection to one fiber end and both metal conducts shorted.

1.4.2 Experimental results

To verify our approach we fabricated a fiber integrating a structure with a CPC electrode in contact with both a solid-core of AST_{10} and a thin layer of the $As_{40}Se_{52}Te_8$ glass. This glass composition was chosen for its better thermal drawing compatibility with the polysulfone (PSU) cladding used here, which results in a better layer uniformity. Note that in this fiber, the metallic electrodes were embedded inside a CPC electrode. The conductivity of this assembly is still dominated by the high conductivity of the metal. The high viscosity of CPC in contact with the thin-film is however beneficial to maintain a layer of uniform thickness [11]. The contacts between the CPC electrodes and the glasses were found to be ohmic.

We reproduced the experiment described in section 1.3.4 to measure the potential drop between the CPC and the metallic electrodes along a one-meter long fiber piece. This time however, the experiment was done under three conditions: first in the dark, then when the fiber was illuminated, at the same location, by a white light source and then by a green (532 nm) LED, with intensity so that the generated photo-current in the thin-film by both illumination was almost the same. The results are shown in Figure 1.10 and illustrate the proposed concept very well. Indeed, since the green light is almost fully absorbed in the semiconducting layer [8], a significant change of thin-film resistivity (and hence a high photo-current) can be obtained while leaving δ_c, and thus the potential distribution across the layer, unchanged. White light on the other hand penetrates much deeper in the material and will change the conductivity of both the thin-film and the fiber core, changing δ_c and the voltage distribution. From these experiments we could extract the value $\delta_c = 143$ cm for this fiber system. This value is much larger than previous ones in solid-core structure because of the increase of S_{CPC} imposed by the new structure design. Note that we used green versus white light for this proof of concept, but many fiber parameters such as the glass composition or fiber geometry can be tuned to apply this approach to a wide range of radiation frequencies.

This new fiber system can now support a fixed potential profile $V(z)$ that can be varied by changing the applied boundary conditions. Given the (1.4.1), one realizes that all possible profiles are a linear combination of the two functions:

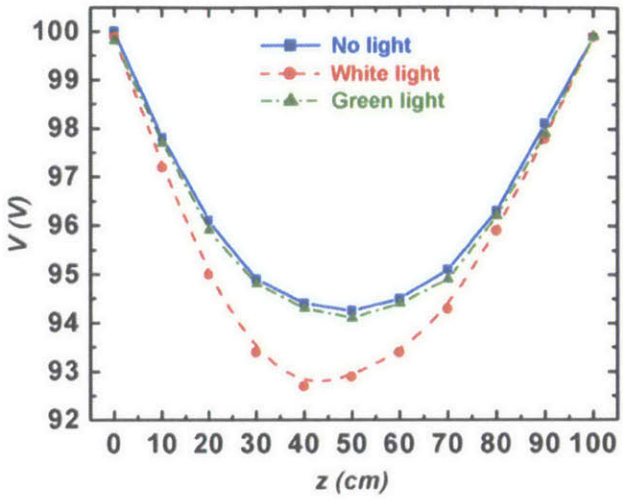

Figure 1.10: Experimental results (dots, the lines are added for clarity) of the voltage profile of a one-meter long fiber piece from panel A in the dark (in blue), and under a spot of white light (in red) and green light (in green) at the same location, same width and of similar intensity.

$$V^I(z) = \frac{V}{\sinh\left(L/\delta_c\right)} \sinh\left(\frac{L-z}{\delta}\right) \tag{1.4.2}$$

and

$$V^{II}(z) = \frac{V}{\sinh\left(L/\delta_c\right)} \sinh\left(\frac{z}{\delta}\right) \tag{1.4.3}$$

obtained for the boundary conditions $V_0 = V$ and $V_L = 0$, and vice-versa. A third independent voltage profile can also be imposed by applying a voltage between the CPC electrode and the electrode contacting the thin-film only, resulting in a nearly uniform potential $V(z) = V$, since δ_f is much larger than the fiber lengths considered. Hence, we can measure three independent photo-currents that result from the integration of the stimuli intensity profile modulated by these different voltage distributions, from which some axial information about σ_{ph} and hence Φ_0 can be extracted as we show below.

1.5 Resolving a single optical beam

1.5.1 Beam localization

Let us consider the case of an incident uniform light beam, with a rectangular optical wave front, at a position z_0 along the fiber axis, and with a width $2\Delta z$. It generates a photoconductivity profile $\sigma_{ph}(z) = \sigma_{ph}$ if $z \in [z_0 - \Delta z, z_0 + \Delta z]$, and 0 otherwise. The generated current for each configuration can be derived, integrating over the illumination width and rearranging the hyperbolic terms:

$$i_{ph}^{I} = \frac{2CV\delta_c\,\sigma_{ph}}{\sinh\left(L/\delta_c\right)} \sinh\left(\frac{L - z_0}{\delta_c\delta_c}\right) \sinh\left(\frac{\Delta z}{\delta_c}\right) \tag{1.5.1}$$

$$i_{ph}^{II} = \frac{2CV\delta_c\,\sigma_{ph}}{\sinh\left(L/\delta_c\right)} \sinh\left(\frac{z_0}{\delta_c}\right) \sinh\left(\frac{\Delta z}{\delta_c}\right) \tag{1.5.2}$$

$$i_{ph}^{III} = 2CV\sigma_{ph}\Delta z \tag{1.5.3}$$

The first two currents are a function of the beam position which can be simply extracted by taking the ratio $r = \frac{i_{ph}^{I}}{i_{ph}^{II}}$ alleviating the dependence on the beam intensity and width. We can extract z_0 from the measurement of r through the relation:

$$z_0 = \frac{\delta_c}{2} \ln\left[\frac{e^{L/\delta_c} + r}{e^{-L/\delta_c} + r}\right] \tag{1.5.4}$$

This was experimentally verified by illuminating a one-meter long piece of the fiber shown in Figure 1.8, with a 1 cm width beam from a green LED, at different locations z_0 along the fiber length, as depicted schematically in Figure 1.11.

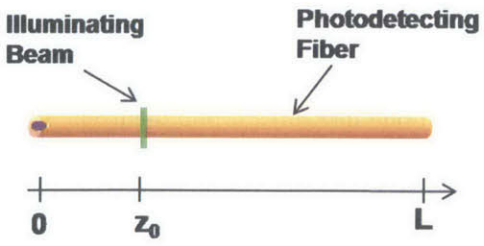

Figure 1.11: Schematic of the illuminated fiber by a single optical beam.

The position detection results are shown in Figure 1.12 where the straight line represents the experimental points of illumination of the fiber while the dots are the reconstructed positions from measuring the ratio of photo-currents r. The agreement between the experimental and measured positions is excellent, with errors made on the position smaller than $\pm$ 0.4 cm in the middle of the fiber.

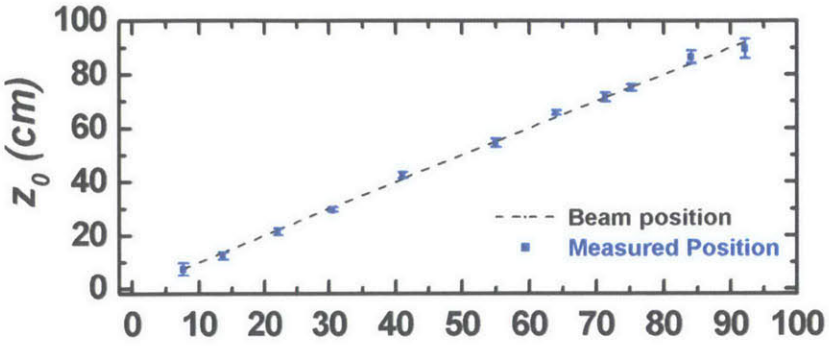

Figure 1.12: Real position (black dashed line) and reconstructed position with error bars(blue dots) of an optical beam incident on a 1 m-long fiber at different positions z_0.

1.5.2 Position error

Error over the beam position depends on a large number of parameters (Fiber length, δ_c, beam position and intensity, geometry etc...). Indeed, fluctuations of the photo-currents, that come from various sources [36, 37, 38], lead to variations on the ratio r, resulting in errors in the measured beam's position. To assess the resolution of our system, we first measured the dark current noise i_N, considered in good approximation to be the only source of noise here. We found it to be around 10 pA in our experimental conditions, using similar techniques as those explained in [34]. This noise current is the same for configurations I and II given the symmetry of the system. Intuitively, when one measures a photo-current $i_{ph}^{I,II}$, its mean value lies within the segment defined by $i_{ph}^{I,II} \pm i_N$. In a simple and conservative approach, we define the resolution of our system as the difference z_{0+} - z_{0-} of the two obtained positions z_{0+} and z_{0-} when the maximum error on the currents are made, i.e when r is given by $r_+ = \left(i_{ph}^I + i_N\right) / \left(i_{ph}^{II} - i_N\right)$ and $r_- = \left(i_{ph}^I - i_N\right) / \left(i_{ph}^{II} + i_N\right)$ respectively. These error bars are represented in the graph

of Figure 1.12. The resolution found is sub-centimetric, i.e. two orders of magnitude smaller than the fiber length. This is to the best of our knowledge the first time that a beam of light can be localized over such an extended length and with such a resolution, using a single one dimensional distributed photodetecting device requiring only four points of electrical contact.

1.5.3 Other beam characteristics

The beam position is not the only spatial information we can reconstruct with this system. Indeed, the ratio of i_{ph}^{II} and i_{ph}^{III} allows us to reconstruct Δz as z_0 is known, by measuring the ratio $\frac{\sinh(\Delta z/\delta_c)}{\Delta z/\delta_c}$. This also enables to evaluate σ_{ph}, using i_{ph}^{III} , and hence reconstruct the associated beam intensity . In Figure 1.13 we schematically depict the illumination profile for a broader light beam.

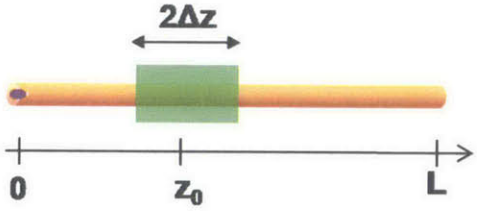

Figure 1.13: Schematic of the fiber illuminated by a rectangular optical wave front.

Figure 1.14 shows an example of experimental illumination profile of green LED light (black dashed line, centered at 43 cm, width 18 cm, with a conductivity $\sigma_{ph} = 6\sigma_{dark}$) and the reconstructed profile from current measurements (blue data points, centered at 43.5 cm, width 24 cm and $\sigma_{ph} = 4.7\sigma_{dark}$). The positioning is very accurate as expected from the results above, while a slightly larger width is measured. This error is due to the large value of δ_c compared to Δz, which results in a ratio of i_{ph}^{II} to i_{ph}^{III} more sensitive to noise than the ratio of i_{ph}^{I} over i_{ph}^{II} . It is however clear from discussions above that the fiber system can be designed to have a much better resolution for different beam width ranges, by tuning δ_c to smaller values.

Also under study is the integration time required for this system. The speed at which we can vary the potentials depends on the bandwidth associated with the equivalent circuit, taking into account transient current effects in amorphous semiconductors. In this proof-of-concept, measurements were taken under DC voltages applied, varying the boundary conditions after

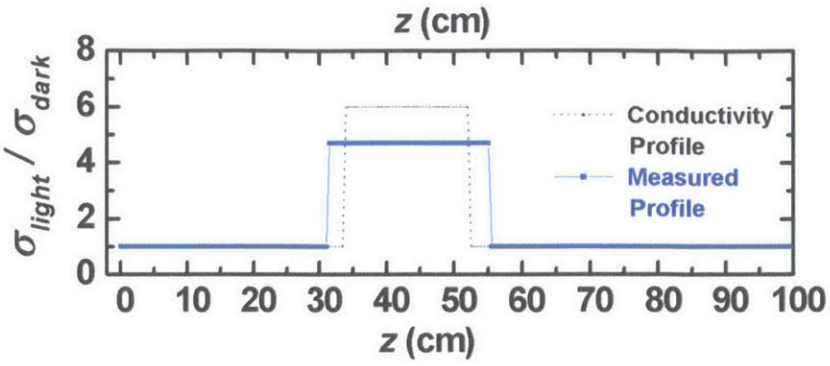

Figure 1.14: Real profile (black doted line) and reconstructed profile (blue dots) for a rectangular wave front incident on the same fiber as in Figure 1.12.

transient currents are stabilized (typically after a few seconds). Novel designs, especially fibers where the semiconducting material has been crystallized through a post-drawing crystallization process [10], and integrating rectifying junctions that have proven to have several kHz of bandwidth [13], could result in significant improvement in device performance and speed.

1.6 Extracting axial information from multiple incoming beams

When more than one beam are incident on the fiber, each one brings a set of three unknown parameters to be resolved (its axial position, width and power). Since our detection scheme provides three independent photo-currents, some prior knowledge on the stimuli is then required to localize each beam along the fiber axis. For example, we can localize two similar illumination events (with approximately same width and power), that are incident at different axial positions.

1.6.1 Two identical beams

Let us consider the simpler case where two such beams impinging the fiber have a width $2\Delta z$ - as depicted in Figure 1.15 - much smaller than the solid-core characteristic length δ_c, so that

$$\frac{\sinh(\frac{\Delta z}{\delta_c})}{\frac{\Delta z}{\delta_c}} \approx 1 \tag{1.6.1}$$

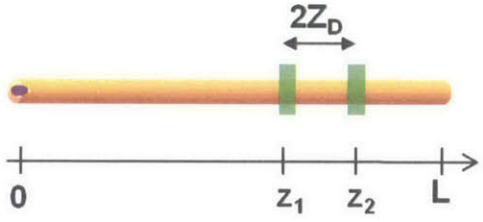

Figure 1.15: Schematic of photodetecting fiber illuminated by two similar, narrow optical beams.

They each generate a photo-conductivity σ_{ph} at their positions $z_1 < z_2$. The photo-currents measured are the sum of the measured currents with individual beams. Defining $Z_m = \frac{z_1 + z_2}{2}$ and $Z_D = \frac{z_2 - z_1}{2}$, we can derive:

$$i_{ph}^{I} = \frac{4CV\delta_c\,\sigma_{ph}}{\sinh\left(L/\delta_c\right)} \sinh\left(\frac{\Delta z}{\delta_c}\right) \sinh\left(\frac{L - Z_m}{\delta_c}\right) \sinh\left(\frac{Z_D}{\delta_c}\right) \tag{1.6.2}$$

$$i_{ph}^{II} = \frac{4CV\delta_c\,\sigma_{ph}}{\sinh\left(L/\delta_c\right)} \sinh\left(\frac{\Delta z}{\delta_c}\right) \sinh\left(\frac{Z_m}{\delta_c}\right) \sinh\left(\frac{Z_D}{\delta_c}\right) \tag{1.6.3}$$

$$i_{ph}^{III} = 4CV\sigma_{ph}\Delta z \tag{1.6.4}$$

Following the same approach as in the single beam case, we can reconstruct Z_m and Z_D, and hence z_1 and z_2. On Figure 1.16, we show the experimental illumination of a fiber with two identical beams of width 6 cm from the same green LED (dashed black curve) at positions 54 cm and 75 cm. The blue dots represent the reconstructed beam position, with measured position 51 $\pm$ 3 cm and 78 $\pm$3 cm for the two beams. The error on the positions were computed in a similar fashion as before.

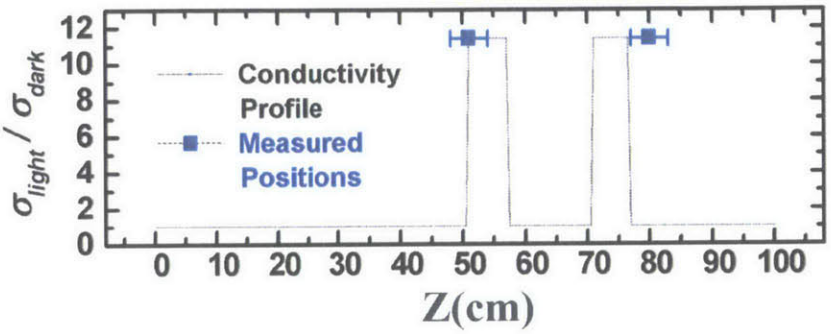

Figure 1.16: Position measurements of the two beams. In black doted line is the conductivity profile generated by the two incoming beams while the blue dots are the reconstructed positions with the error bars.

1.6.2 Three identical, regularly-spaced beams

An optical signal made out of three beams requires even more additional constraints to be resolved. For example, three similar beams equidistant from one to the next can be detected and localized with our system. Indeed, here again only two unknowns have to be found: the central beam position and the distance between two adjacent beams. The derivation of the algorithm to extract these positions from the different current measurements is very similar to what has been derived above. In Figure 1.17 we show experimental results of the localization of three incoming beams of same width (Δz = 6 cm) and intensity (generating a photo-conductivity $\sigma_{ph} = 8.5\sigma_{dark}$) at positions z_1 = 35.5 cm, z_2 = 55.5 cm, and z_3 = 75.5 cm. The generated conductivity pattern is represented by a black doted line on the graph. The reconstructed positions from photo-current measurements were 30 $\pm$4 cm, 51.5 $\pm$ 4 cm and 73 $\pm$ 4 cm, in very good agreement with the real beams locations. Note that in these two multiple beams cases, we

could only extract the position of the beams but not their intensity nor width. If we knew the width of each beam however, we would be able to extract the position and intensity assuming that this intensity is the same.

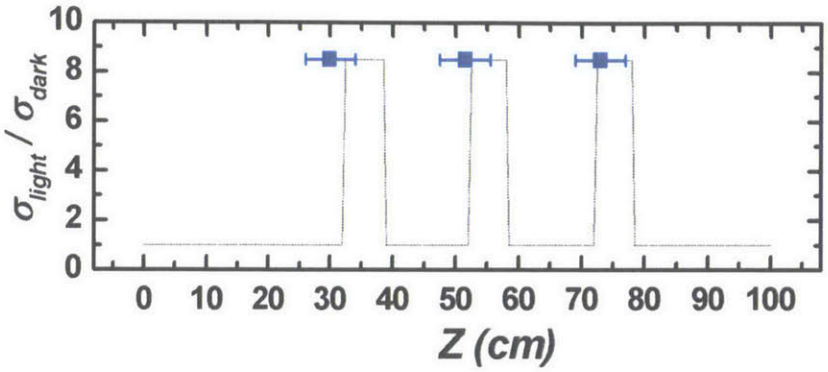

Figure 1.17: Position measurements of the three beams. In black doted line is the conductivity profile generated by the three incoming beams while the blue dots are the reconstructed positions with the error bars.

1.7 Conclusion

In conclusion, axially resolved optical detection was achieved in an axially symmetric multimaterial fiber. A fiber architecture that combines insulating and semiconducting domains together with conductive metallic and polymeric materials was demonstrated. This architecture supports a convex electric potential profile along the fiber axis that can be varied by changing the boundary conditions. As a result, the position, width and the intensity of an arbitrary incoming rectangular optical wavefront could be reconstructed. Under given constraints, two and three simultaneously incident beams could also be spatially resolved. The ability to localize stimuli along an extended fiber length using simple electronic measurement approaches and with a small number of electrical connections, presents intruiging opportunities for distributed sensing.

Chapter 2

Fabrication and characterization of fibers with built-in liquid crystal channels and electrodes for transverse incident-light modulation

2.1 Abstract

We report on an all-in-fiber liquid crystal (LC) structure designed for the modulation of light incident transverse to the fiber axis. A hollow cavity flanked by viscous conductors is introduced into a polymer matrix, and the structure is thermally drawn into meters of fiber containing the geometrically scaled microfluidic channel and electrodes. The channel is filled with LCs, whose director orientation is modulated by an electric field generated between the built-in electrodes. Light transmission through the LC-channel at a particular location can be tuned by the *driving frequency of the applied field*, which directly controls the potential profile along the fiber.

2.2 Introduction

Photonic structures employing liquid crystals (LCs) are the subject of ongoing investigations. In addition to their ubiquitous presence in display technologies [41], LCs are used to tailor laser emission [42, 43, 44, 45], in spatial light modulators [46, 47], as tunable wavelength filters [48], and in a host of other applications [49, 50, 51, 52, 53]. In recent years, LC-infiltrated fiber structures have been explored for modulating *axially* propagating light through the application of externally generated fields [27, 54, 55, 56, 57]. Here we report on the fabrication and characterization of a polymer fiber LC device for modulating *transversely* incident light. This regime of operation is particularly interesting for large-area flexible display applications, such as, e.g., in fabrics. The fiber contains an axially uniform, rectangular LC-filled microchannel flanked on two opposing sides by built-in conductive polymeric electrodes. We investigate the effect of the applied voltage driving frequency on the transversely transmitted intensity as a function of fiber length. In accordance with our model, the high resistivity of the electrodes imposes an axial electric potential drop over a length controlled by the driving frequency. Therefore, by contacting the electrodes at multiple locations along their length, individual pixels along axially symmetric fibers could be addressed.

2.3 Fabrication of a Liquid-Crystal-infiltrated fiber

The fabrication of this fiber is realized by constructing a macroscopic version of the desired structure and subsequently scaling it down to the microscopic dimensions by thermal drawing. The fabrication process flow is depicted in Figure 2.1.

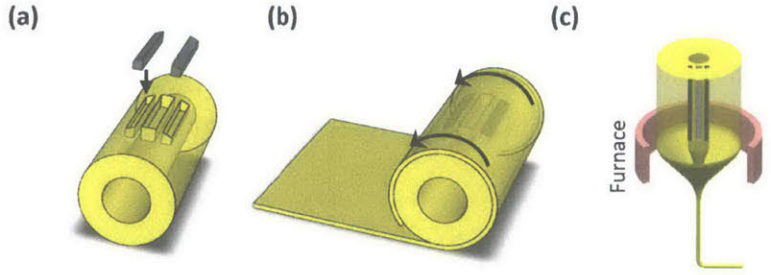

Figure 2.1: Fiber fabrication process flow.

Initially, 75 μm thick polycarbonate (PC, Lexan 104) is rolled onto a mandrel to a desired outer diameter and consolidated under vacuum at $\sim 190^oC$. Subsequently, a group of three parallel pockets are milled into the structure at prescribed locations and dimensions. The outer two pockets are filled by geometrically-matched strips of conductive carbon-loaded polyethylene (CPE), which are prepared through thermal pressing of individual 100 μm thick CPE films, and the central pocket is left empty. To confine the hollow pocket and neighboring conductors, the structure is clad with additional 75 μm thick PC films and reconsolidated. With the mandrel removed, the preform is thermally drawn at $\sim 250^oC$ into hundreds of meters of flexible fiber containing a hollow microchannel flanked by conducting electrodes. The optical micrograph in Figure 2.2 depicts the cross section of the fiber structure.

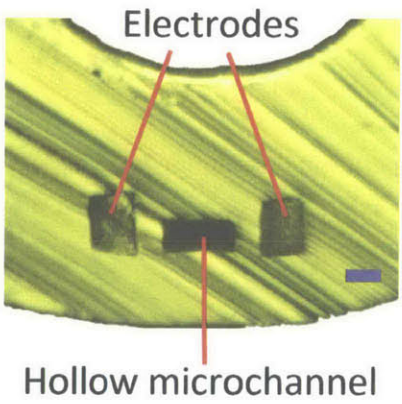

Figure 2.2: Optical micrograph of the fiber structure containing a hollow microchannel flanked by conducting electrodes. Scale bar is 20 μm.

Post-draw, LCs (Merck MLC-2058, n_e=1.71, n_o=1.51 at 589 nm) are infiltrated into the microchannel through capillary action by dipping the fiber tip into a droplet of the LC mixture at room temperature. Although no alignment layer is applied to the microchannel walls prior to LC infiltration, the LC director orients itself along the fiber axis for several centimeters, as has also been observed in the microchannels of photonic crystal fibers [57]. (Note that since the index of refractive of polycarbonate (n_{pc} = 1.58) is lower than the extraordinary index of the LC, the LC channel could also function as a waveguide under an appropriate voltage bias and input polarization conditions, which we plan to investigate in future work.)

2.4 Principle of light-transmission frequency modulation

2.4.1 Transverse light modulation

In this letter, we explore the properties of the in-fiber LC channel as a variable attenuator for light transmitting perpendicular to its axis. The fiber is characterized in a microscope equipped with a bottom illuminator, polarizer and analyzer pair, and a top mounted CCD camera. The spatial arrangement of the setup is shown schematically in Figure 2.3.

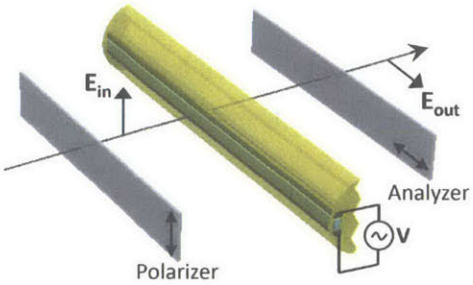

Figure 2.3: Schematic of the experimental setup used to measure light transmitting though the LC-channel normal to the fiber axis. The voltage is applied directly to the in-fiber electrodes (black) which flank the LC-channel (blue).

Randomly polarized white light first passes through a polarizer with the transmission axis aligned perpendicular to the fiber axis. With the absence of an applied voltage, the linearly polarized light only interacts with the ordinary index of the LC, hence no change in polarization state occurs when the light passes through the fiber. Since the analyzer is fixed with its transmission axis aligned parallel to the fiber axis, no light is transmitted. Upon applying a voltage above a threshold voltage, the LC director rotates in the direction of the applied field, causing the incoming wave to experience both the ordinary and extraordinary indices of the LC molecules. This interaction leads to a change in the initial linear polarization state of the light passing through the microchannel, which translates into partial transmission through the analyzer [58]. An image captured on the CCD camera with the voltage off and on (100 V_{rms} at 100 Hz) is depicted in Figure 2.4 for a 5-cm long fiber.

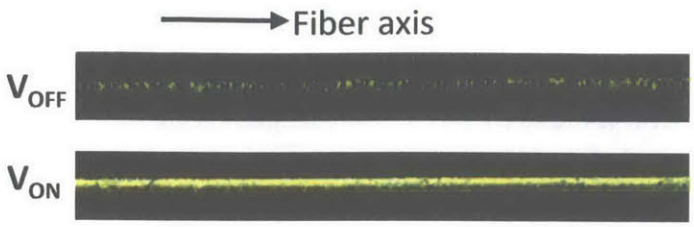

Figure 2.4: Images of the fiber with voltage OFF (0 V) and ON (100 V). The randomly distributed white specks seen in the OFF state arise from imperfections in the LC alignment near the microchannel wall.

Note that for this fiber length and driving frequency, the electrodes are equipotential along their entire length. Figure 2.5 displays the dependence of the transmission intensity on driving voltage, demonstrating continuous tunability of the transversely-transmitted intensity. No change in transmission is observed below a threshold voltage of ~25 V. Above 25 V, the transmission increases with increasing voltage up to the maximum applied voltage of 140 V.

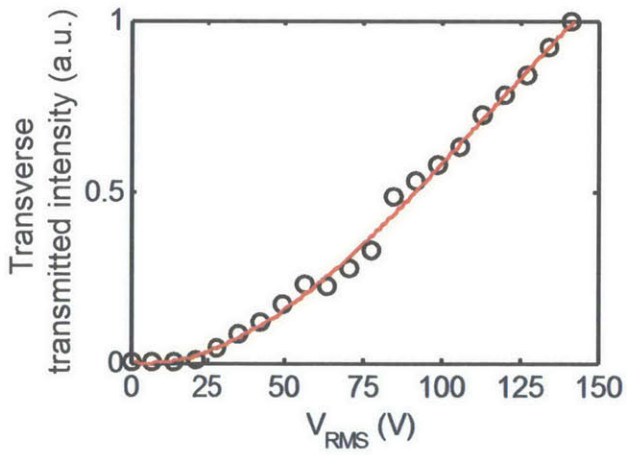

Figure 2.5: A characteristic transmission vs. applied voltage spectrum obtained at a driving frequency of 100 Hz. The red curve is an empirical fit to the data using a 6th order polynomial. (Note that the sole purpose of this polynomial function is to relate the experimentally measured transmission dependence on the applied voltage, which we use in Figure 2.11.)

Note that, should the applied voltage continue to grow, we expect the transmission would reach a maximum (when the LC director is oriented at 45 degrees relative to the fiber axis) and then begin to decrease back to zero as the LC director approaches 90 degrees. Although the limitations of our voltage source precluded measuring this full transmission range, we have observed a saturation in transmission intensity when characterizing fibers in which the electrodes are separated by a slightly smaller distance, as shown in Figure 2.6.

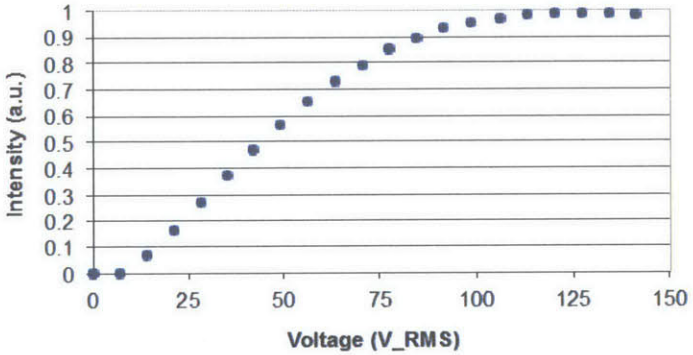

Figure 2.6: An example data set of transmission intensity vs. applied voltage showing a saturation in transmission intensity. The maximum applied voltage is 140 V.

2.4.2 Frequency-controlled voltage profile

An interesting feature of this LC channel emerges when considering extended fiber lengths. The CPE electrodes and the PC-enclosed LC channel which they flank form a distributed RC circuit in a transmission line fashion, in which each unit length of fiber Δz has a series resistance from the CPE electrodes (R_{CPE}) and a parallel capacitance from the PC and LC (C_{eq}). These can be estimated from the structure as illustrated in Figure 2.7 and are expressed as:

$$C_{eq} = \epsilon_{PC}\left(\frac{w_E}{2h_{PC}+h_{LC}} + \frac{h_{LC}\left(1-\frac{\epsilon_{PC}}{\epsilon_{LC}}\right)w_{LC}}{(2h_{PC}+h_{LC})\left(2h_{PC}+h_{LC}\frac{\epsilon_{PC}}{\epsilon_{LC}}\right)}\right)\Delta z \tag{2.4.1}$$

$$R_{CPE} = \frac{\rho_{CPE}\Delta z}{h_E w_E} \tag{2.4.2}$$

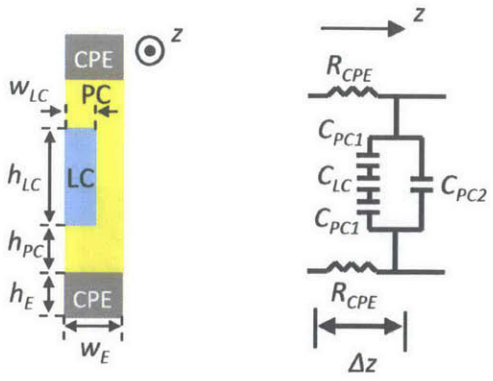

Figure 2.7: (Left) Cross-section schematic of the liquid crystal (LC) channel and neighboring electrodes (see Figure 2.2). (right) Equivalent circuit for a unit fiber segment length Δz used to analyze the frequency response. The structural and materials parameters used in this study are the following: $w_E = 30\mu m$, $w_{LC} = 17\mu m$, $h_{LC} = 35\mu m$, $h_{PC} = 14\mu m$, $h_E = 23\mu m$. The resistivity ρ of CPE is experimentally determined to be $\sim 1.1\Omega m$. The dielectric constants of the LC and PC are taken as $\epsilon_{LC} = 13$ and $\epsilon_{PC} = 3$.

By applying Kirchoff's laws to the distributed circuit along the fiber length, the electric potential along the electrodes a distance z away from the point where they are contacted can be expressed as [59]:

$$V(z) = \frac{V_0 \cosh\left(\frac{L-z}{\delta}\right)}{\cosh\left(\frac{L}{\delta}\right)} \tag{2.4.3}$$

with

$$\delta = \frac{\Delta z}{\sqrt{i4\pi f R_{CPE} C_{eq}}} = \sqrt{\frac{h_E w_E}{i4\pi f \rho_{CPE}\epsilon_{PC}\left(\frac{w_E}{2h_{PC}+h_{LC}} + \frac{h_{LC}\left(1-\frac{\epsilon_{PC}}{\epsilon_{LC}}\right)w_{LC}}{(2h_{PC}+h_{LC})\left(2h_{PC}+h_{LC}\frac{\epsilon_{PC}}{\epsilon_{LC}}\right)}\right)}} \tag{2.4.4}$$

where V_0 and f are, respectively, the amplitude and driving frequency (in Hz) of the applied voltage, while L is the length from the point of electrode contact to the end of the fiber. Since the transfer length δ depends on frequency, it follows that $V(z)$ and hence the light transmission at a particular location away from the point of electrical contact is also frequency dependent.

Figure 2.8 depicts a surface plot of the calculated voltage dependence on driving frequency and position along the axis of a 40-cm long fiber that is contacted at the 0-cm end[1].

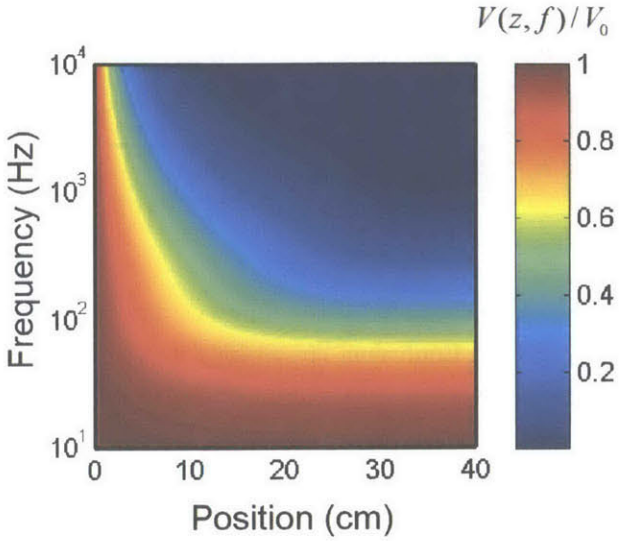

Figure 2.8: Surface plot of the calculated electric potential as a function of frequency and position along the fiber axis for a 40-cm long fiber that is contacted at the 0-cm side.

Evident in this plot is the voltage decay towards longer distances and higher frequencies, a consequence primarily of the high CPE resistivity ($\rho_{CPE} \approx 1.1\ \Omega.m$). While, on the one hand, this voltage drop limits the driving frequency on long fibers that are electrically contacted at one location, it presents an opportunity on the other. Since the CPE electrodes can be electrically contacted at multiple locations along their length, the rapid voltage decay at a typical LC driving frequency of 1 kHz actually facilitates independent and simultaneous control over multiple sections of the same LC channel, a function that is particularly useful for display applications. Note that if a uniform voltage is desired along the entire fiber length (which would be useful, for example, in the aforementioned waveguide implementation of the LC channel), metallic electrodes (such as, e.g., eutectic alloy $Bi_{58}Sn_{42}$ or indium) can be drawn in place of or

[1]Due to the dielectric anisotropy of the LC ($\epsilon_{\parallel} = 21.2$, $\epsilon_{\perp} = 4.7$), the value of ϵ in the direction orthogonal to the electrodes changes as a function of the LC director orientation. However, it is the ϵ_{PC} that plays the dominant role in the equivalent capacitance of the structure; hence, variations of ϵ_{LC} will only slightly affect the frequency response. For the calculations shown in Figure 2.8, the average value for ϵ_{LC} is used, i.e, $\epsilon_{LC} = 13$

in direct contact with the conductive polymer inside PC-clad fibers [9, 60]. Having a resistivity about 8 orders of magnitude lower than CPE, the metallic electrodes will maintain the same electric potential along the entire 40-cm fiber length at frequencies of 1 kHz and lower, as shown in Figure 2.9.

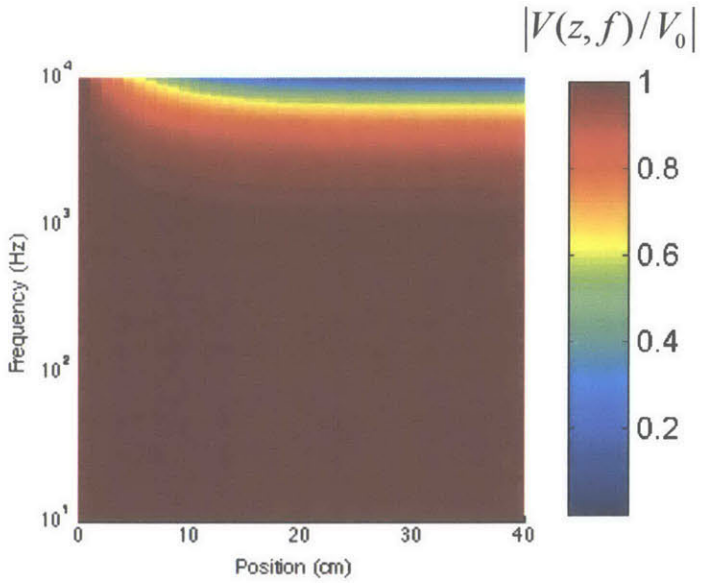

Figure 2.9: Surface plot of the calculated electric potential as a function of frequency and position along the length of a 40-cm long fiber contacted at the 0-cm side. The geometry used for this calculation is the same as in Figure 2.7; the resistivity of the CPE electrodes (1.1 Ωm) is replaced by the resistivity $Bi_{58}Sn_{42}$ (39x10^{-8} Ωm)). At a driving frequency of 1 kHz or lower, the electric potential is the same along the entire fiber length.

2.5 Experimental results

To demonstrate the driving frequency as a control knob for tuning the transmission intensity as a function of position, we contact an electrode pair of a 40-cm long fiber at three different locations as depicted in Figure 2.10.[2].

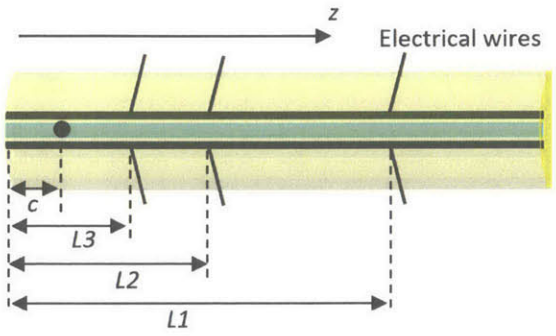

Figure 2.10: Schematic of the experiment used to test the model derived from the equivalent circuit in Figure 2.7. The distance between the point of electrical contact to the electrodes (denoted by a pair of slightly angled black lines) and the end of the fiber is 35 cm, 10.5 cm, and 7 cm, corresponding to L1, L2, and L3, respectively. The black dot (a distance c (1 cm) from the fiber end) corresponds to the location where the light transmission is measured in Figure 2.11.

For each of the three experiments ($L = L1, L2, L3$), 125 V are applied to the electrodes at point L, and the transmission intensity is recorded at point c as the frequency is varied in the range of 30 – 104 Hz. Figure 2.11 displays the measured frequency-dependent transmission (open circles); the calculated transmission curves (solid lines) based on our model agree well with the data. Note that at a driving frequency of 1kHz, the applied voltage at $L1$ has no influence over the transmission at point c, in contrast to applying the voltage at $L3$ and $L2$. As noted previously, this localized control over the LC response presents an intriguing opportunity for driving multiple sections of the same LC channel.

[2]Fixing the transmission location and varying its spacing from the point of electrode contact is equivalent to fixing the point of electrode contact and varying the position where transmission is measured. We find that the uniformity of the LC director alignment decreases with increasing distance away from the fiber facet (i.e., where the LC is introduced into the microchannel), therefore we perform the former experiment and choose a transmission location close to the fiber facet (1 cm away). Improved LC infiltration methods for realizing longer homogeneously aligned in-fiber LC cells are currently under investigation.

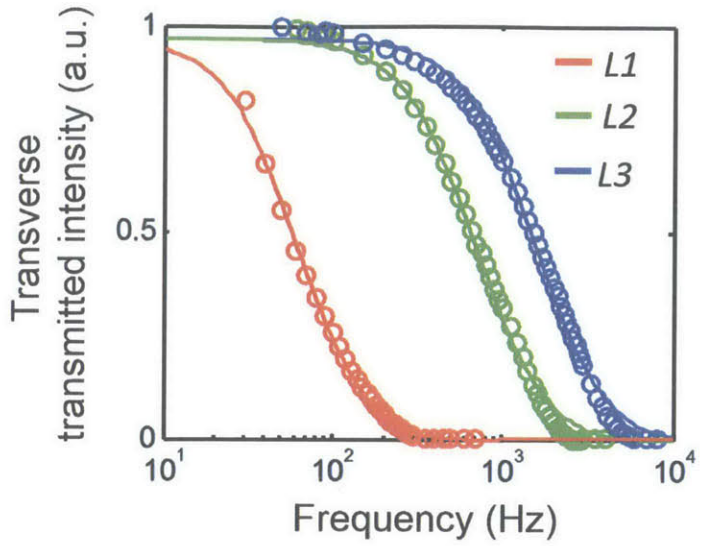

Figure 2.11: Transmission intensity measurements for driving the electrodes at positions L1, L2, and L3 as a function of frequency. Open circles and solid lines correspond to the measured and calculated values, respectively. To calculate the transmission as a function of frequency, (2.4.3) is first used to determine the voltage as a function of frequency at point c. The voltage is then converted into the corresponding transmission intensity by using the polynomial fit from the measurement depicted in Figure 2.10.

2.6 Conclusion

In summary, we have reported on an in-fiber LC structure designed for modulation of light incident transversely to its axis. Viscous conductive electrodes used to address the LC channel are built directly into the fiber cladding. We demonstrated the transverse-transmission intensity at a particular location along the LC channel could be controlled by the driving frequency of the applied voltage, which allows for localized light attenuation control along axially symmetric fibers.

Chapter 3

All-in-fiber chemical sensing

3.1 Abstract

A new all-in-fiber trace-level chemical sensing approach is demonstrated. Photoconductive structures, embedded directly into the fiber cladding along its entire length, capture light emitted anywhere within the fiber's hollow core and transform it directly into an electrical signal. Localized signal transduction circumvents problems associated with conventional fiber-optics, including limited signal collection efficiency and optical losses. This approach facilitates a new platform for remote and distributed photosensing.

3.2 Introduction

Optical fibers have been actively investigated for remote chemical sensing applications[61, 62, 63, 64, 65, 66, 67, 68, 69, 70, 71, 72, 73, 74, 75, 76, 77]. Of particular interest for detection of hazardous materials, such as explosives, are luminescence-based detection schemes[78, 79, 80, ?, 81], which can employ optical fibers for collecting and transmitting an emissive signal at one end of the fiber to an optical detector at the other. Inherent to this approach are several limitations. First, both the remoteness and sensitivity of detection are restricted by the fiber numerical aperture (NA), its transmission and bending losses, and the sensitivity of the detector. While the NA can be increased with hollow core photonic bandgap fibers [75, 77] and highly sensitive photodetectors can be implemented, the detection system is nonetheless limited so long as the

fiber is used for waveguiding. Second, with light emitted only at the end facet, distributed sensing over large areas is inefficient. Here we introduce and demonstrate an alternative materials system and approach for remote luminescence-based chemical detection that is inherently adaptable for distributed sensing and circumvents the aforementioned limitations. Rather than rely on the propagation of the optical signal to a distal external detector, we embed the photodetector along the entire length of the fiber itself. This approach maximizes signal collection efficiency, while eliminating the need to propagate the optical signal along the fiber. Previously reported metal-semiconductor-metal photodetecting fibers [3, 34, 8, 59] performed well under relatively high incident power (mW scale); however, their high noise equivalent power (NEP) precluded their use for chemiluminescent (CL) sensing applications, which require the detection of radiation at the nW scale. By optimizing the fiber materials architecture for chemical sensing and reducing the NEP by nearly two orders of magnitude compared to previous work [34], here we demonstrate trace-level detection limits of peroxide vapor down to 10 parts per billion (ppb), on par with current state-of-the-art hydrogen peroxide vapor sensors [82, 81]. Liquid peroxide-based explosives (PBE) have emerged as materials of choice for makeshift explosives. Indeed PBE have been used in a number of recent incidents involving bombing of mass transit systems[1], leading to world-wide restrictions on liquids carried on board aircraft that is still enforced today. The small footprint, potential for multiplexing, flexible form factor, scalable manufacturing, and compatibility with miniaturized electronics of the fiber architectures demonstrated here enable remote and distributed sensing schemes to meet current societal needs.

[1]Liquid PBE were used in several terrorist acts, including: (i) The attacks on the London transit system in 2005. (see "Report into the London Terrorist Attacks on 7 July 2005" http://www.official-documents.gov.uk/document/cm67/6785/6785.pdf (last accessed September 2012)) (ii) The foiled 2006 plot to blow up several airplanes (see http://www.usnews.com/usnews/news/articles/060810/10london.htm (last accessed September 2012))

3.3 Fiber design an fabrication

3.3.1 Design considerations

The design of the fiber structure dictates its detection capabilities. First, the azimuthal numerical aperture of the detectors should be maximized in order to collect as much of the isotropically emitted CL detection signal as possible. Second, the chosen chalcogenide glass should absorb at the detection wavelength, while remaining thermomechanically compatible for drawing with the other materials comprising the preform. The central wavelength emitted by the peroxide sensing material is 532 nm [77], which makes crystalline $Se_{97}S_3$ (E_g=1.74 eV) [83] a suitable candidate. This glass can be codrawn in its amorphous state with polysulfone (PSU) and crystalized post-draw, which makes PSU a good candidate for the polymer cladding material [11, 84]. Third, in order to be detectable, the small photocurrent signal resulting from the CL emission must be greater than the current noise level. For weak signals, this noise is proportional to the square root of the dark current [36], which should therefore be minimized to enhance the signal-to-noise ratio (SNR). Consequently, the appropriate geometry of the $Se_{97}S_3$ layer should be implemented [34]. Note also that if n identical photodetectors are connected in parallel, both I_{bright} and I_{dark} scale linearly with n. However, the noise only grows as $\sqrt{I_{dark}} \propto \sqrt{n}$, while the signal $I_{bright} - I_{dark}$ grows as n, and therefore the SNR scales as $\sqrt{n}$, which is an incentive to integrate multiple independent detectors into one fiber.

Taking into account the above design considerations, a hollow core rectangular preform was assembled and thermally consolidated as shown in Figure 3.1. In this design, two identical independent photodetecting structures were incorporated into the preform to demonstrate the aforementioned sensitivity enhancement. The aspect ratio for each of the photoconductive channels was maximized in order to increase the azimuthal numerical aperture while decreasing the dark conductance of each detector, which scales inversely with the layer thickness [34].

Additional preform materials design constraints emerge from the fact that drawing a thin and wide $Se_{97}S_3$ sheet is complicated by its tendency to undergo capillary break up into thin filaments while being thermally drawn [11, 84]. We found that controlling the surface roughness of the preform materials surrounding the $Se_{97}S_3$ layer was key to maintaining its continuity during the draw. Thus, the preform is designed in such a way that only laminar polymer surfaces are

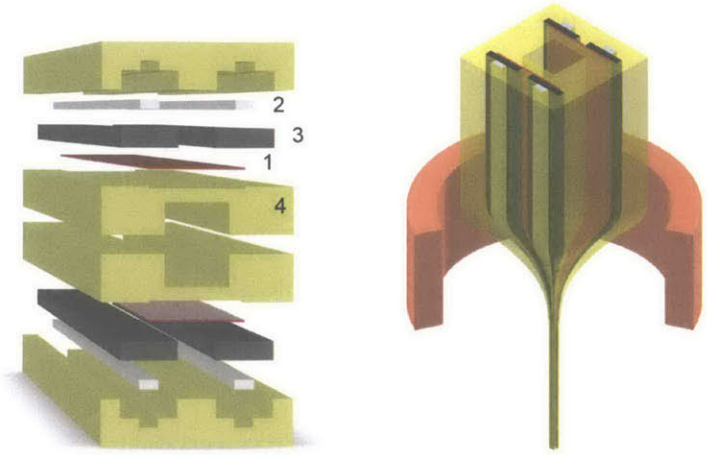

Figure 3.1: Left: schematic depiction of the preform assembly. (1) Thin PSU sheet (75 μm) with $Se_{97}S_3$ layer (35 μm) evaporated onto its laminar facet. (2) $Sn_{63}Pb_{37}$ electrodes and (3) CPC pads are incorporated in between (4) PSU plates, which are machined to encapsulate all of the components. The assembly is then thermally consolidated to form a monolithic macroscopic preform. Right: schematic depiction of the thermal drawing process showing the preform fed through the hot zone of a furnace (red ring) and drawn into a fiber.

in contact with the $Se_{97}S_3$ layer. Conductive polycarbonate (CPC) pads are inserted between the $Se_{97}S_3$ layer and the metal electrodes in order to decrease cross sectional discontinuity of interfacial tension and viscosity at the transition from the insulating to the conductive regions along the $Se_{97}S_3$ edge. These pads prevent shear flow of $Se_{97}S_3$ during the draw, further improving its continuity and uniformity.

3.3.2 Fabrication

The preform was thermally drawn at $\sim 265^oC$ at a stress of $\sim 650g.mm^{-2}$ into a fiber containing two independent photoconducting structures flanking opposite sides of the fiber as illustrated in Figure 3.1. Scanning electron microscopy (SEM) images of the fiber cross section, shown in Figure 3.2, reveal the continuous $Se_{97}S_3$ layer linking the CPC pads for each of the detecting structures. After the draw, the fiber was annealed under vacuum at 150^oC for two days in order to crystallize the $Se_{97}S_3$ layers for improved conductivity [84, 10].

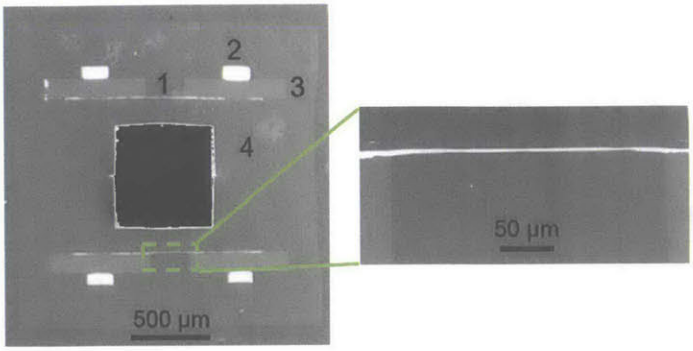

Figure 3.2: Cross sectional SEM micrograph of the resulting fiber. The (1) to (4) numbers refer to the components labeled in Figure 3.1.

3.4 Fiber optoelectronic properties

3.4.1 Fiber electronic equivalent circuit

We characterized the fiber's electronic and optoelectronic properties under AC driving conditions. The dependence of the impedance on the driving frequency was measured on one of the detectors inside a 7-cm long fiber using an LCR Meter (Hioki 3532-50) both in the dark and under illumination by an LED (Thorlabs, M530L2) from $\sim 10cm$ distance, as shown schematically in Figure 3.3(a). To explain the frequency-dependent impedance, we claim that the fiber's electronic behavior can be derived from the equivalent circuit suggested on Figure 3.3(b), which stems from the cross sectional geometry of the fiber.

The impedance Z of the circuit is given by:

$$Z = 2R_{contact} + \frac{2R_{CPC}}{1 + jR_{CPC}C_{CPC}\omega} + \frac{R_{Se}}{1 + jR_{Se}C_{Se}\omega} \tag{3.4.1}$$

where $R_{contact}$ is the fiber-to-setup contact resistance and C_{Se} the capacitance between the electrodes. R_{Se} is the $Se_{97}S_3$ layer resistance, where the most significant illumination-induced change is expected to occur. R_{CPC} and C_{CPC} are the effective resistance and capacitance of the CPC pads, respectively, which include contributions from the CPC-$Se_{97}S_3$ junctions that are also potentially affected by illumination. Figure 3.3(c) displays the measurement results together with the best fits from the suggested equivalent circuit.

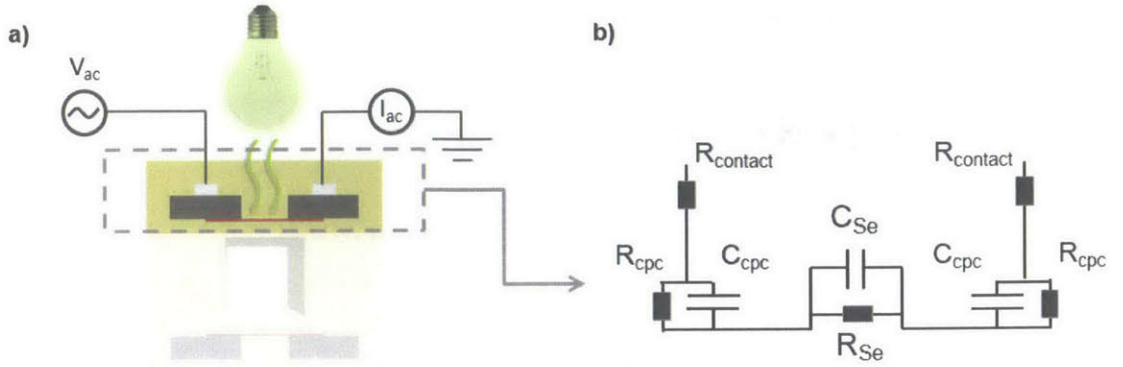

Figure 3.3: Characterization of the photodetecting structure: (a) Schematic of the optoelectronic characterization setup used to measure the current in the dark and under illumination for one of the fiber-embedded photodetecting structures. (b) Suggested equivalent circuit for the photodetecting structure.

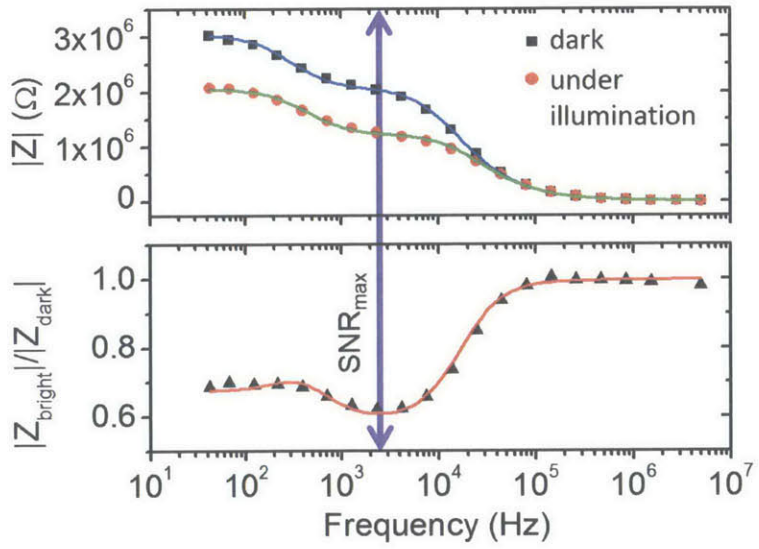

Figure 3.4: (Top) Fiber impedance frequency response (absolute value) in the dark - $|Z_{dark}|$ (black squares) and under illumination - $|Z_{bright}|$ (red circles), with the best fits to (3.4.1). (Bottom) $\left|\frac{Z_{bright}}{Z_{dark}}\right|$ (black squares) as a function of driving frequency, together with the ratio between the respective fits (red curve).

Note that while these measurements were performed with an external illumination source, we expect the photo-response to be the same for light generated inside the fiber since the optical losses of the PSU cladding are negligible over the distances considered here. The values of R and C_{Se} resulting from the fits were found to be 4 $k\Omega$ and 7 pF, respectively. R_{CPC}, C_{CPC} and R_{Se} were found to be 498 $k\Omega$, 1162 pF and 2031 $k\Omega$ in the dark and 422 $k\Omega$, 950 pF and 1196 $k\Omega$ under illumination, a photo-induced change of 15%, 18% and 41%, respectively. The quality of the fits stresses that the simple equivalent circuit suggested here accurately describes the detectors' optoelectronic frequency response. The optical bandwidth of this detector under a DC driving voltage and sinusoidally modulated optical source was measured to be 400 Hz, which is sufficient for recording CL signals resulting from intake of the analyte, having a typical rise time on the order of seconds [77].

3.4.2 Optimizing the operation frequency

Since the impedance of the detector depends on the driving frequency, we can obtain the frequency $f_{SNR_{max}}$ at which the SNR performance of the registration setup will be optimal. We notice from Figure 3.3(c) that the ratio of impedances under illumination and in the dark $\left|\frac{Z_{bright}}{Z_{dark}}\right|$ is minimized at $f_{\left|\frac{Z_{bright}}{Z_{dark}}\right|_{min}}$ = 2.3 kHz. At this frequency the photocurrent signal maximally contrasts the dark current background. Since the current noise (and thus the NEP) is strongly correlated to the dark current amplitude, the SNR is maximized at this frequency, i.e. $f_{SNR_{max}} = f_{\left|\frac{Z_{bright}}{Z_{dark}}\right|_{min}}$. Note that the same expression for $f_{SNR_{max}}$ can be derived by explicitly considering the scaling of the current noise. Indeed, we can explicitly consider the scaling of the noise to determine the optimal driving frequency. For small signal detection we can state that the noise current is proportional to the square root of the dark current $i_N \sim \sqrt{I_{dark}}$ [ref supp Rosencher]. In this case, $SNR \sim \delta I/\sqrt{I_{dark}}$ where δI is the small photocurrent we aim to detect. In the case of ohmic device behavior, which we confirmed independently by measuring a linear dark IV curve, $I \sim 1/Z$ and thus

$$\delta I \sim \delta(\frac{1}{Z}) = -\frac{\delta|Z|}{|Z|^2} \tag{3.4.2}$$

$$= \frac{|Z_{dark}| - |Z_{bright}|}{|Z_{dark}|^2} \tag{3.4.3}$$

and thus

$$SNR \sim \frac{|Z_{dark}| - |Z_{bright}|}{|Z_{dark}|^{\frac{3}{2}}} = \frac{1 - \left|\frac{Z_{bright}}{Z_{dark}}\right|}{\sqrt{Z_{dark}}} \tag{3.4.4}$$

In the range of frequencies in which $|Z_{dark}|$ is approximately constant, $SNR \propto 1 - \left|\frac{Z_{bright}}{Z_{dark}}\right|$. Noting that $|Z_{dark}|$ plateaus around the minimum of $\left|\frac{Z_{bright}}{Z_{dark}}\right|$, we conclude that $f_{SNR_{max}} = f_{\left|\frac{Z_{bright}}{Z_{dark}}\right|_{min}}$, which is the same as the conclusion derived from the simple heuristic explanation brought forth earlier.

3.4.3 Fiber responsivity

An important characteristic of this photodetector is its responsivity R, which we measured by illuminating the fiber with the aforementioned LED at a known optical intensity and recording the corresponding photocurrent through one of the photodetecting structures. This measurement was performed by driving the fiber and measuring its photo-response with a lock-in amplifier (Sanford Research System, SR810) at the optimal driving frequency (2.3 kHz) under driving voltage amplitudes ranging from 0 to 2 volts, for which R was found to be invariant when normalized to I_{dark}. Accordingly, we express the responsivity in terms of % of I_{dark} addendum to the photocurrent per unit of optical flux through the detector area, which we found to be $R = 0.090 \pm 0.003$ [in % of I_{dark}/nW]. This responsivity translates into 0.246 $nA.nW^{-1}$ for a typical dark current of 0.273 μA used in the subsequent CL measurements. Furthermore, noise current measurements for this range of driving voltages revealed that the sensitivity of our signal registration setup is limited to 0.1 nA by the lock-in amplifier resolution rather than by the fiber detector itself.

3.5 Chemical detection

3.5.1 Protocol

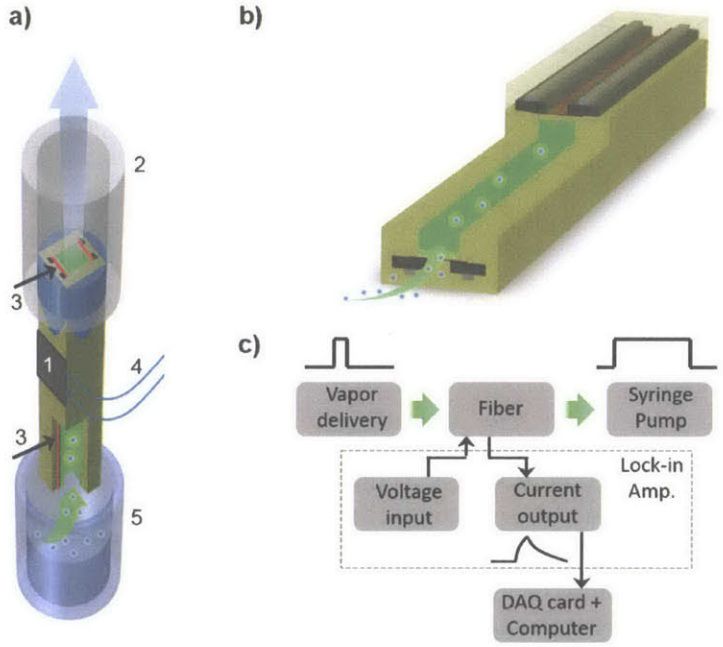

Figure 3.5: Chemiluminescent Measurement Setup and Results: (a) Schematic of the measurement scheme. (1) – The fiber is secured into (2) – an adapter connected to the flexible tubing of the syringe pump intake. PSU cladding is locally removed to expose the electrodes connected to (3) - the photodetector and (4) – external wires are connected to the individual electrodes. The fiber is inserted into the headspace of (5) – the vial containing the peroxide solution; (b) The fiber section schematic in greater detail. (c) Block diagram of the setup. The syringe pump delivers the peroxide vapor to the fiber inserted into the headspace of the vapor delivery vial. The photodetecting fiber structure is driven by a voltage input from the lock-in amplifier and the result of a sensing event is registered as a current output. The signal is then recorded by a DAQ card and buffered to computer.

The fiber is prepared for peroxide measurement by coating the inner surface with the sensing material [77] and hermetically sealing one end to tubing that is attached to a syringe pump. The optofluidic system and electronics setup is shown schematically in Figure 3.5(a-c). A standard measurement protocol is divided into a number of stages, each labeled by a

corresponding Roman numeral in Figure 3.6(d), which depicts a typical measurement.

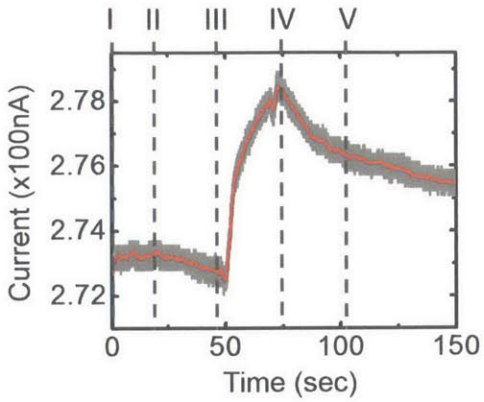

Figure 3.6: A typical photocurrent measurement resulting from the protocol described in the text.

First (I), the current in the fiber-embedded photodetector is recorded for 20 seconds in order to obtain the baseline. Second (II), the syringe pump is turned on at a flow rate of 50 $cc.min^{-1}$ and the fiber is purged for 30 seconds with air. During this phase the current slightly decreases due to the purging of the peroxide residue from the previous measurement. Third (III), the free fiber end is exposed to the headspace of a vial containing an aqueous peroxide solution of known peroxide concentration for 20 seconds. During this phase vapors of peroxide flow through the fiber core and interact with the sensing material which results in CL. This light is captured by the fiber embedded photodetecting structure, and the lock-in amplifier registers the resulting photocurrent as a current addendum to the baseline. Fourth (IV), the vial is removed while the pump continues to run for an additional 20 seconds. Finally (V), the pump is turned off and the current gradually returns to the baseline level.

3.5.2 Results

According to the protocol described above, photocurrent measurements were performed for liquid phase peroxide concentrations increasing from 1 to 35%, from which vapor phase concentrations were calculated using Henry's Law [85]. All measurements were performed at the driving frequency of 2.3 kHz while the dark current was 0.273 μA with a driving voltage of 0.5 V. The curve describing the photocurrent vs. vapor phase peroxide concentration resulting from these measurements has a slope of $0.043 \pm 0.001\ nA.ppm^{-1}$ and is shown on Figure 3.7(e) together with the noise current of 0.127 nA (standard deviation over a 1 second interval). Using the detector's responsivity and the above dark current, these measurements were translated into a sensitivity curve having a slope of $0.176 \pm 0.005\ nA.ppm^{-1}$ with a noise level of 0.517 nW corresponding to a NEP of $0.731\ nW.\sqrt{Hz}^{-1}$. The detection limit at SNR = 1 was found to be 3.0 ± 0.1 ppm for this sensitivity slope and noise level.

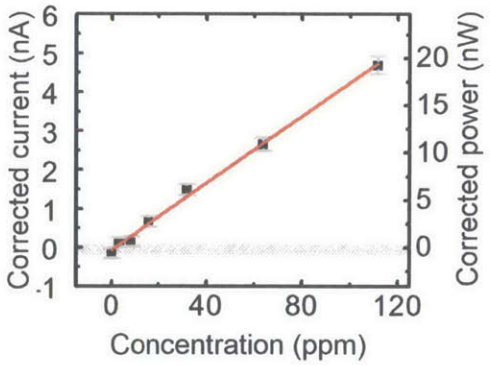

Figure 3.7: Peroxide sensitivity curve. Experimental points (black squares with error bars) are depicted with the linear fit (red solid line) and the noise level (patterned strip).

3.5.3 Performance of heated fiber detector

In order to increase the performance of the all-in-fiber chemical sensor, we integrated it into a system that provides heat to the peroxide sensing material ($\sim 80^oC$) in order to obtain optimal CL efficiency and uses a peristaltic pump at a continuous flow rate of 60 $cc.min^{-1}$ for analyte vapor delivery. The electronics for this setup were limited to operation at a DC voltage, which is not the optimal condition, as was shown earlier. Measurements were performed on a 7-cm section of fiber with a cross section similar to the one in Figure 3.2. The CL material was coated on the inner wall of a silica capillary of the same length as the fiber and was then inserted into the fiber's core. A voltage of 5V DC was applied across the photodetecting structures' electrodes contacted in parallel and the current was registered by an electrometer (Keithley 6517). Although heating the fiber from room temperature up to 80^oC reduced photoconductivity by a factor of three and slightly increases the noise due to a doubling of the dark current, in this configuration the photodetecting fiber was found to sense hydrogen peroxide vapor concentrations as low as 10 ppb as shown in Figure 3.8.

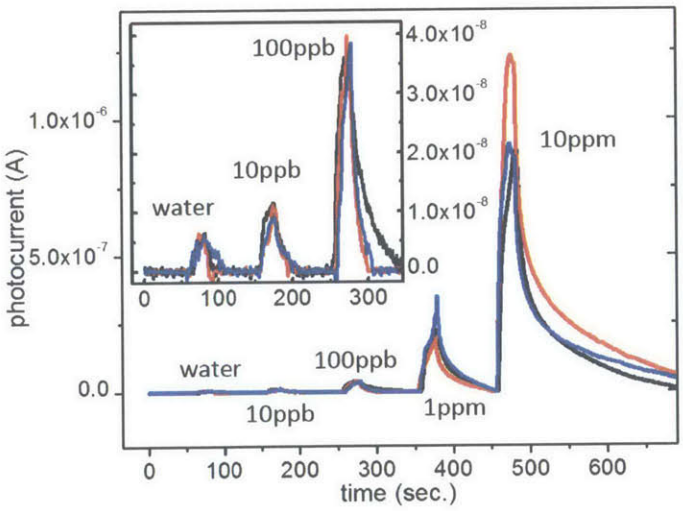

Figure 3.8: Sensitivity measurements for three fiber samples.

This detection limit is comparable to state-of-the-art commercially available systems and three orders of magnitude more sensitive than the performance depicted in Figure 3.7. About an order of magnitude in this increase is attributed to the higher driving voltage and the rest arises

from the enhancement in CL material sensitivity to peroxide at the elevated temperature [82]. Note that in the current measurements, a signal from water sets the detection limit. Importantly, this signal is not the result of an optical event, but arises from transient heating/cooling of the fiber when moisture-rich air from the headspace of a water-only vial passes through a heated inlet tip before entering the fiber. If eliminated, the prototype limit-of-detection would improve by another order of magnitude and would be able to measure single ppb level of peroxide vapor.

3.5.4 Practical considerations

We point out several practical considerations that are relevant in the design of a remote and/or distributed chemical sensing system using these fibers. First, unlike optical transmission fibers, photodetecting fibers are not immune to electromagnetic interference. This problem can be alleviated by using standard electronic filtering techniques and/or by engineering electromagnetic barriers for blocking particular radiation from reaching the photoconductive structure [3, 34]. Second, the dark current will scale linearly with fiber length if all of the chalcogenide glass is crystalized [34]. To circumvent the reduction in sensitivity associated with the increased dark current, the fiber may be selectively crystalized only at those axial locations where a sensing event is expected to occur. For example, in a remote sensing application, only the last few centimeters of a fiber can be coated with CL material and crystallized, in which case the sensitivity will not depend on the length of the remaining fiber segment. This length independence stems from the fact that the conductivity of the in-fiber crystallized $Se_{97}S_3$ is about 8 orders of magnitude higher than in the amorphous state [84]. A particular advantage of the extended photodetecting structure is the potential for distributed sensing, such as illustrated in Figure 3.9, where a periodic array of intake holes can be introduced along the fiber length for large area vapor sampling. As in the example with remote sensing, not the entire fiber but only short sections near the intake holes need to be crystallized. Moreover, the location of a peroxide vapor plume along the fiber axis could be determined by implementing this distributed sensing scheme with fiber architectures having the ability to axially resolve the optical detection event along their length as describe in [59].

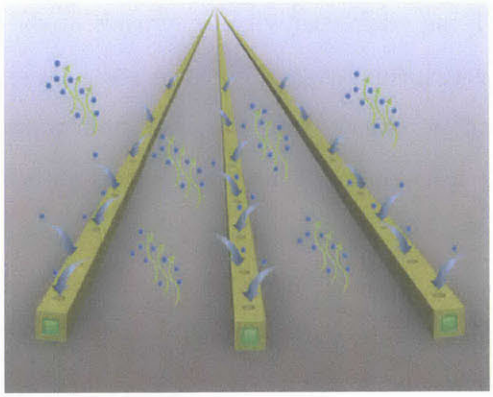

Figure 3.9: Concept drawing for remote and distributed sensing using hollow core photodetecting fibers. Slots can be introduced through the fiber cladding along its entire length to enable distributed, large area sample collection and measurement.

3.6 Conclusion

In conclusion, we have reported the fabrication and characterization of an all-in-fiber chemical sensor for detection of trace-levels of peroxide vapor down to 10 ppb. The sensing principle is based on fiber-embedded $Se_{97}S_3$ photoconductive structures that flank a hollow core and detect CL from the reaction of a sensing material with peroxide vapor flowing through the core. These photodetecting structures can extend hundreds meters in length, suggesting possible applications for remote and distributed sensing. In principle one can further improve the NEP of the device by employing an in-fiber photodiode structure as described in [13]. Furthermore, the ability to create multiple microfluidic channels in multimaterial fibers [45] paves the way towards intrafiber multianalyte detection.

Chapter 4

Piezoelectric Fibers for Conformal Acoustics

4.1 Abstract

Ultrasound transducers have many important applications in medical, industrial, and environmental settings. Large-active-area piezoelectric fibers are presented here, which can be woven into extended and flexible ultrasound transducing fabrics. This work opens significant opportunities for large-area, flexible and adjustable acoustic emission and sensing for a variety of emerging applications.

4.2 Introduction

4.2.1 Acoustic transduction background

The first modern ultrasound transducer was developed after the tragedy of the Titanic in 1912, when the need arose for an echolocating device to detect icebergs and, later on, submarines. The success of sonar technology stimulated research in this field and led to the development of a large number of important applications such as non-destructive testing (NDT) and medical imaging, with an ever higher accuracy both in direction and range. In recent years, new uses of ultrasound transducers have emerged, particularly in - but not limited to - the medical field, such as photoacoustic imaging of the brain [86], bone healing [87], focused ultrasound surgery

[88], and ocean observation [89]. These applications ideally require large-area, flexible, and addressable transducer arrays, where the amplitude and phase of each individual device can be independently controlled. Several approaches have been pursued to address this challenge. A specially active area of research has been electroactive polymers, which have been widely investigated as an alternative to piezoceramics [90]. In particular, the large values of piezoelectric constants for poly(vinylidene fluoride) (PVDF) and copolymers such as poly(vinylidene fluoride trifluoroethylene) (P(VDF-TrFE)), coupled with their mechanical compliance and processability make them particularly suited for large-area flexible applications. Furthermore, their large bandwidth and low acoustic impedance are an advantage for many medical uses. Another promising path involves capacitive micromachined ultrasonic transducers (CMUTs) [91]. These approaches, however, leave some key challenges unresolved: device reliability issues due to charge trapping, constraints on the device area due to wafer-based processes, acoustic cross-talk, and complex electronic integration [92].

4.2.2 Fiber flexible transducers

Recently developed multimaterial fibers present a number of attractive properties that can address these issues. The preform-based thermal drawing process offers a scalable means of producing kilometer-long fiber devices with submillimetric cross-sectional dimensions [7]. These long and flexible fibers can easily be assembled into large-scale conformal constructs, such as fabrics and sparse meshes [35]. Furthermore, monolithic integration of electrodes into the fiber enables straightforward electrical connection of the device to an external electrical circuit [7]. The latest advances in this field have led to the development of P(VDF-TrFE)-based piezoelectric fibers that are capable of acoustic emission and detection over a broad range of frequencies, from the tens of Hz to the tens of MHz [9]. While the small cross-sectional area of these fibers enables both miniaturization and flexibility, it seemingly involves an equally small active area that potentially limits the fiber performance. Here we introduce a new large-active-area fiber design that addresses a fundamental tradeoff between the requirement of maximizing the surface area of the acoustic device, and the inherent energy penalty associated with generating large area interfaces. This is achieved by confining the low viscosity crystalline ferroelectric medium between highly viscous boundaries, thus controlling the kinetics of the fiber thermal drawing

process. We perform interference experiments to show that this novel device is coherent in the axial dimension, and we demonstrate how the coherence property combined with the mechanical flexibility enables acoustic wavefront shaping through precise control over the fiber curvature. Although the single fiber itself presents unique opportunities for minimally invasive sensing and imaging, in this work we take it one step further and analyze collective effects in multiple fibers. Coherent interferences and beam steering capabilities of multi-fiber phased arrays are demonstrated, thus establishing the possibility of assembling large-scale fiber constructs such as fabrics and meshes.

4.3 Fiber design and fabrication

4.3.1 Design considerations

Piezoelectric transducers can be used both in emission and reception, depending on the application. When the transducer operates as a receiver, internal electrodes with a large surface area are desirable as they lead to a higher number of charges generated, and thus a better device sensitivity. As a transmitter, the fiber reaches maximal strain when the electric field is maximal, while remaining below the breakdown voltage. In these two regimes, the large-effective-area fiber design introduced in this paper enhances the transducer performance. Indeed, for a given cross-sectional area, a folded structure enables a several-fold increase in the electrode area and allows high electric fields without a high applied voltage since the piezoelectric layer is thinned down. This approach was developed for piezoceramic actuator stacks, and is of particular interest for use with our fabrication process. The fibers are produced by a thermal drawing technique from a macroscopic preform, which has the desired device structure and geometry but is much larger in its cross-sectional dimensions (see section 4.8.1). One of the appeals of this method is that the assembly of piezoelectric P(VDF-TrFE) layers and conductive polymer electrodes is done at the macroscopic level of the preform, which then yields tens of meters of fibers in a single draw. Therefore, the added cost and complexity of having multiple folded piezoelectric layers is minimal when compared to traditional layer-by-layer deposition techniques. Moreover, we expect the superior compliance and malleability of polymers over ceramics to reduce the risk of brittle failure and enable its use in tensile mode without preloading the device [93].

4.3.2 Challenges associated with the thermal-drawing process

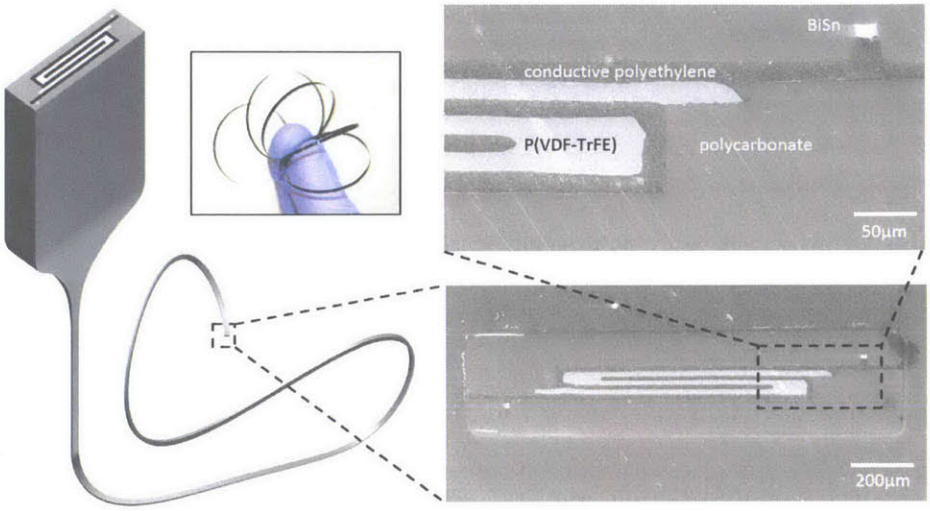

Figure 4.1: Schematic drawing of preform drawn into fiber along with SEM micrographs of piezoelectric fiber and magnification. Inset: Flexible piezoelectric-stack fiber.

As shown in Figure 4.1, the structure of the large-active-area piezoelectric fibers combines sharp corners and turns, numerous interfaces between materials, and large aspect-ratio geometries. Therefore, part of the challenge is to slow down the kinetics of surface energy driven phenomena during the draw, so as to prevent the fiber structure from evolving towards a more thermodynamically favorable geometry and to maintain a good structural integrity [11]. This is of particular importance here because the piezoelectric performance of ferroelectric devices relies critically on the success of electric poling and consequently the uniformity in the thickness of the ferroelectric layers. Typically, a strong electric field ($> 60MV.m^{-1}$), applied across the ferroelectric P(VDF-TrFE) layer through the internal electrodes, is required to permanently align the electric dipoles and achieve macroscopic polarization [94]. Given that the threshold of poling is close to the dielectric strength [95], fluctuations in the ferroelectric layer thickness will reduce the average poling fields, because the applied poling voltage is limited by the thinnest portions where the onset of dielectric break-down begins. Thicker portions experience incomplete poling which leads to an overall sub-optimal piezoelectric response, an effect further aggravated by the nonlinear relation between the remnant polarization and the external electric fields [96].

4.3.3 Materials selection

To address these issues, the fiber materials were carefully selected to meet precise thermo-mechanical and electrical criteria. Previous work has shown that P(VDF-TrFE) is particularly suited to the fiber fabrication process because it solidifies spontaneously from the melt in the ferroelectric β phase [9]. However, being a semi-crystalline polymer, P(VDF-TrFE) is drawn in a low-viscosity molten state and is particularly susceptible to capillary break-up. Therefore one of the key challenges was to identify an electrode material that would have a high viscosity (between 10^4-10^7 Poise) at the draw temperature, enabling it to be co-drawn with P(VDF-TrFE) in a high aspect-ratio geometry while resisting capillary break-up. Carbon-loaded polymers are good candidates for this role, although if their viscosity during the draw is too high, the carbon-black aggregates can undergo a high degree of breakdown resulting in a much-reduced conductivity [97]. Carbon-loaded polyethylene (CPE) was found to have a viscosity that is low enough to maintain a conductivity that is independent of the draw conditions, specifically the level of stress experienced by the fiber, while being high enough to avert capillary break-up (see Figure 4.2).

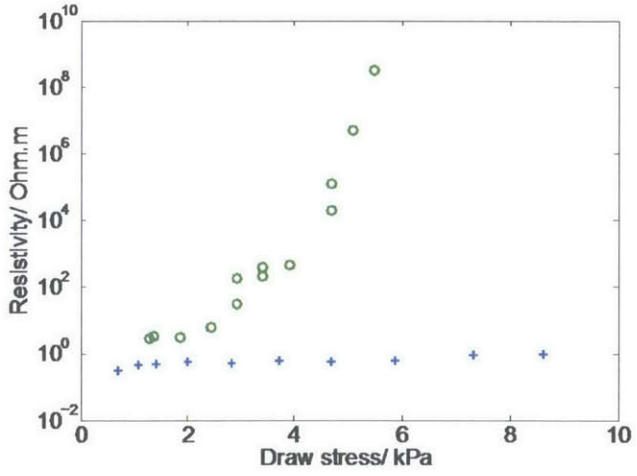

Figure 4.2: Measured resistivity of conductive polycarbonate (circles) and conductive polyethylene (crosses) in the fiber as a function of the draw stress. While conductive polycarbonate loses its conductivity with increased stress during the draw, conductive polyethylene displays a nearly stress-independent resistivity.

4.4 Fiber device acoustic and electronic properties

In order to gain more insight on the performance and limitations of individual fibers, in particular those associated with the new fiber geometry, we characterized their acoustic emission and electrical impedance, and compared the measurement with results from simulations.

4.4.1 Single-fiber acoustic emission profile

The acoustic characterization was performed in water, with a commercial piezoceramic transducer and the fiber transducers in immersion. A large water-tank (43cm x 33cm x 38cm) and time-gated signal processing were employed to minimize the interferences both from acoustic reflections on the walls of the water tank and electromagnetic coupling between the fiber and the transducer. To measure the angular emission pattern of a single fiber, we fixed the distance between the fiber and the ceramic transducer, and rotated the fiber sample a few degrees along its long axis between each measurement. Figure 4.3 a) shows the acoustic radiation pattern of the fiber transducer at 900kHz. The observed anisotropic angular emission along four axes displays a good fit with the simulations (Figure 4.3 b)). This clover-like pattern depends on the ratio of the outer dimensions to the acoustic wavelength, and on the design of the fiber transducer. Note how the angular widths of the lobes are inversely related to the length of the corresponding edge: the emission's directivity could thus be controlled by changing the fiber geometry.

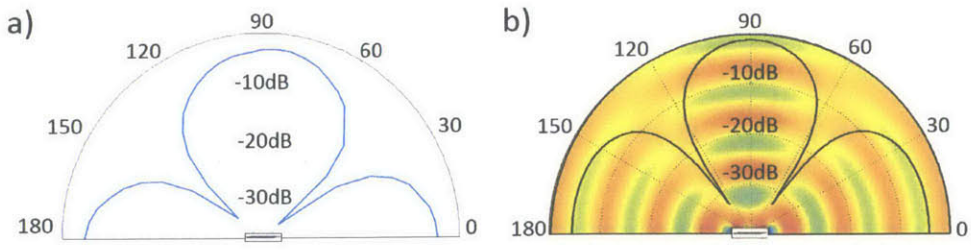

Figure 4.3: a) Acoustic radiation pattern of the piezoelectric fiber measured in water at 900kHz. b) Simulation of the far-field acoustic radiation pattern of a piezoelectric fiber in water at 900kHz.

4.4.2 Fiber electronic behavior and equivalent circuit

Another important property of a piezoelectric fiber is its electrical impedance at various frequencies: not only is its knowledge required when designing interface circuits to deliver optimal power-efficiency and sensitivity, but it is also useful in determining the upper limit for the operational frequency, beyond which the transducer sensitivity rolls off rapidly [9]. We use an impedance analyzer to measure the frequency response of this impedance from 42Hz to 5MHz . Figure 4.4 displays the equivalent circuit of a fiber under test connected to the impedance analyzer. In this simplified approach, the different parts of the fiber along the path of the current are connected in series and characterized by their electrical impedance: Z_{CPE} for the conductive electrodes, $Z_{P(VDF-TrFE)}$ for the piezoelectric layer and a purely resistive term $R_{contact}$ to take into account losses at the connection with the setup.

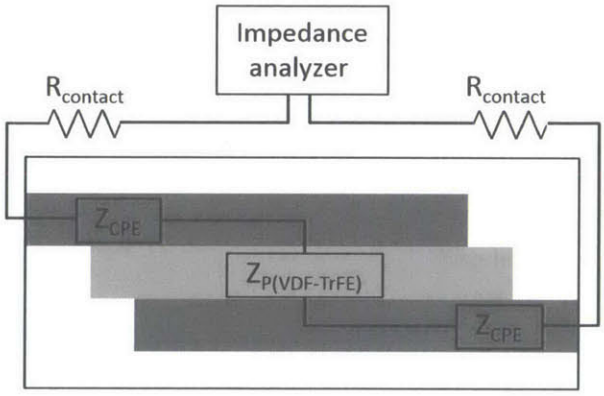

Figure 4.4: Equivalent circuit model of a piezoelectric fiber connected to an impedance analyzer.

It has been reported that the otherwise constant resistivity of CPE decreases at frequencies f above a critical frequency f_0 whose value highly depends on the polymer preparation [98]. We have repeatedly witnessed this effect in these fibers - with f_0 in the 0.5-10 MHz range - and have included it in our model by considering the following frequency dependence of $Z_{CPE}(f)$:

$$Z_{CPE}(f) = \frac{R_{CPE}}{1 + \frac{f}{f_0}} \tag{4.4.1}$$

where R_{CPE} is the low frequency resistance of the electrode. The impedance of the P(VDF-TrFE)

layer is calculated as that of a parallel plate capacitor, so that:

$$Z_{P(VDF\text{-}TrFE)}(f) = \frac{1}{j\frac{\epsilon_p S_p}{t_p} 2\pi f} \tag{4.4.2}$$

$$\text{with} \quad \epsilon_p = \epsilon_p' + j\epsilon_p'' \tag{4.4.3}$$

where S_p, t_p and ϵ_p are respectively the surface of ferroelectric polymer in contact with the electrodes, its thickness and its dielectric permittivity. ϵ_p has a real and imaginary part that are both considered as frequency independent in our approach. The overall impedance of the system is thus modeled as a function of the driving frequency f by adding its components:

$$Z_0(f) = 2R_{contact} + 2Z_{CPE}(f) + Z_{P(VDF\text{-}TrFE)}(f) \tag{4.4.4}$$

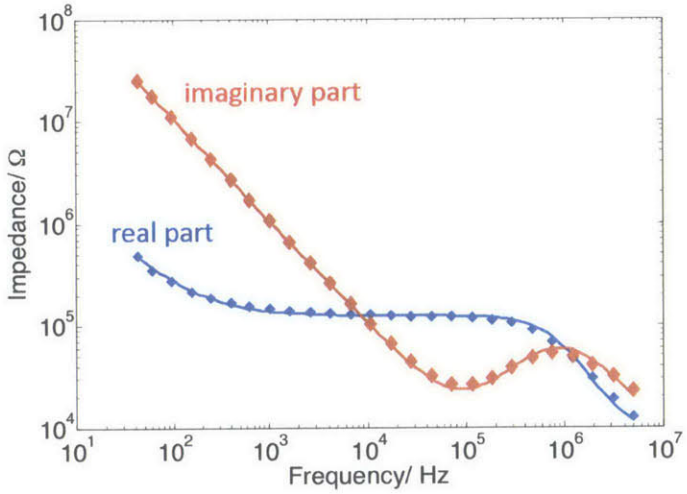

Figure 4.5: Measured (diamonds) and simulated (solid line) electrical impedance real and imaginary parts.

Figure 4.5 displays the real and imaginary parts (resp. blue and red dots) of the measured impedance spectrum for a 3-cm long piezoelectric fiber. Fitting the model derived from the equivalent circuit to these measurements leads to a set of retrieved values [$R_{contact} = 4k\Omega$, $R_{CPE} = 58k\Omega$, $f_0 = 890kHz$, $\epsilon_p' = 8.4\epsilon_0$, $\epsilon_p'' = -0.12\epsilon_0$] for which the theoretical $\mathcal{R}e(Z_0(f))$ and $\mathcal{I}m(Z_0(f))$ (solid lines in Figure 2d)) closely match the experimental data. Furthermore,

the values to which our model leads for ϵ_p' and ϵ_p'' are consistent with the literature [99]. When connected to a controlling circuit such as the one used in the following section, the fiber can therefore be replaced by its equivalent circuit for all predicting purposes regarding its electrical behavior in this broad range of frequencies.

4.5 Fiber arrays interference patterns

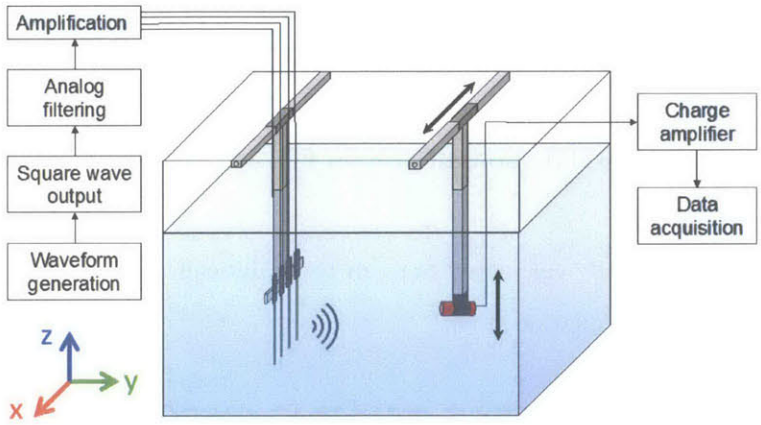

Figure 4.6: Schematic of under-water acoustic characterization set-up of a piezoelectric fiber array.

One of the interesting features of fiber transducers is that they can be assembled in dense arrays and woven into conformal fabrics. To illustrate this possibility, phased arrays of two and four piezoelectric fibers were constructed, and beam steering measurements were performed in water. Figure 4.6 shows the measurement setup in which fibers held parallel along a vertical (Z) axis and facing the same (Y) direction are driven at 600kHz with an adjustable phase difference between consecutive fibers. This frequency was selected because it lays in the overlapping region of the operational bandwidths of the commercial transducer and the analog chips used in the measurement (see section 4.8.2). The acoustic power pattern in the XZ plane is then measured with a commercial transducer at a fixed distance of 20 cm from the fibers. Figure 4.7 shows a simulated 2D map of the acoustic power generated by the interference between two piezoelectric fibers driven in phase.

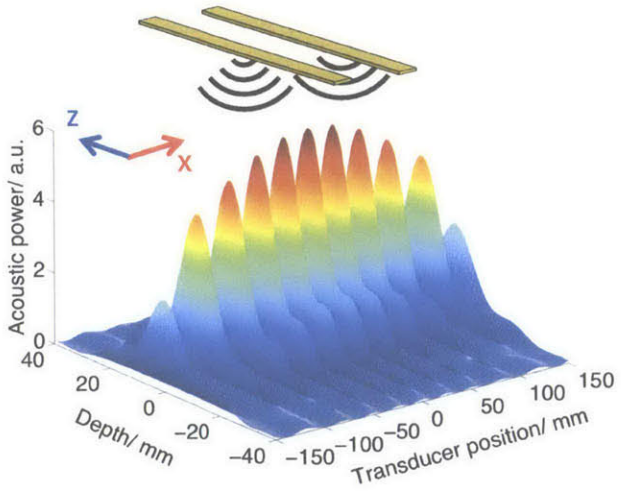

Figure 4.7: 3D representation of the acoustic pressure field of a two fiber array emitting in phase.

This pattern is numerically calculated but can be analytically described for small x and z by the following diffraction equation [100]:

$$P \propto sinc^2\left(\frac{\pi w x}{\lambda f}\right) sinc^2\left(\frac{\pi L z}{\lambda f}\right)\left(1 + cos\left(\frac{2\pi d x}{\lambda f}\right)\right) \tag{4.5.1}$$

where the width w and the length L of the fiber determine the slowly varying envelope of the radiation pattern in the X and Z directions respectively. The extended length of the fiber transducers (40mm for the tested device) results in a rapid decay of the acoustic power along Z, and a radiation pattern that is focused around the X-axis.

4.5.1 Two-fiber interferences

Figure 4.8 compares the measurements with the theory for this two-fiber array in the cases where the fibers are in phase ($\Delta\phi = 0$) and out of phase ($\Delta\phi = \pi$). These interference patterns show that the two fibers emit in a coherent manner, a proof of the fiber device uniformity over extended lengths. The differences between theoretical and experimental results can be attributed to variations in emitting power and orientation from one fiber to the other.

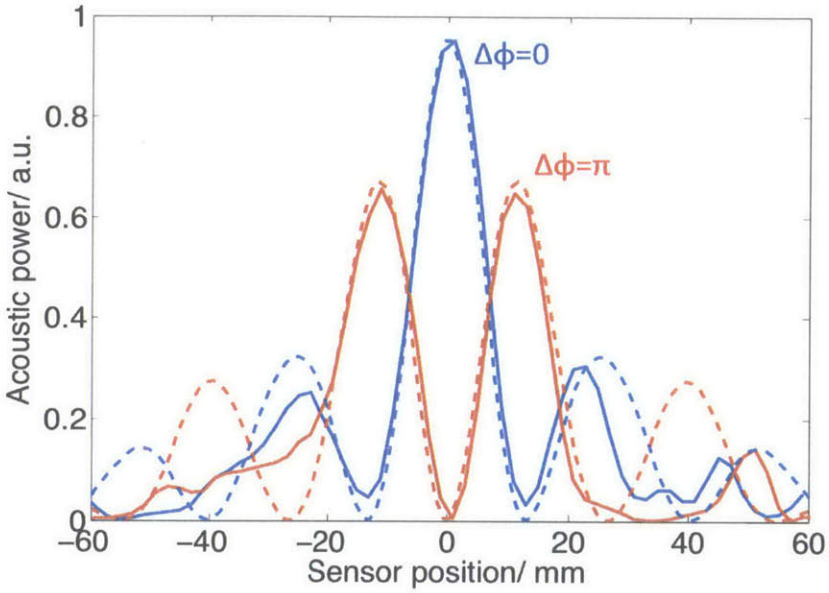

Figure 4.8: Two fiber array: measured (solid line) and simulated (dotted line) acoustic power along x at a distance of y=20mm from the array.

4.5.2 Four-fiber acoustic beam-steering

The ability to control and focus acoustic energy is further improved by increasing the number of fibers being independently driven in the phased array. For example, with four fibers, one can perform beam steering by applying a relative phase difference:

$$\Delta\phi = \frac{2\pi f d sin(\theta)}{c} \tag{4.5.2}$$

between adjacent fibers. Here f is the frequency, d the pitch (i.e. the distance between two consecutive fibers, along the X axis), c the speed of sound in water, and θ the desired steering angle. This measurement was carried out with steering angles from 0^o to 5^o (Figure 4.9). The inset shows that there is a very good fit between the expected and measured positions of the central lobe.

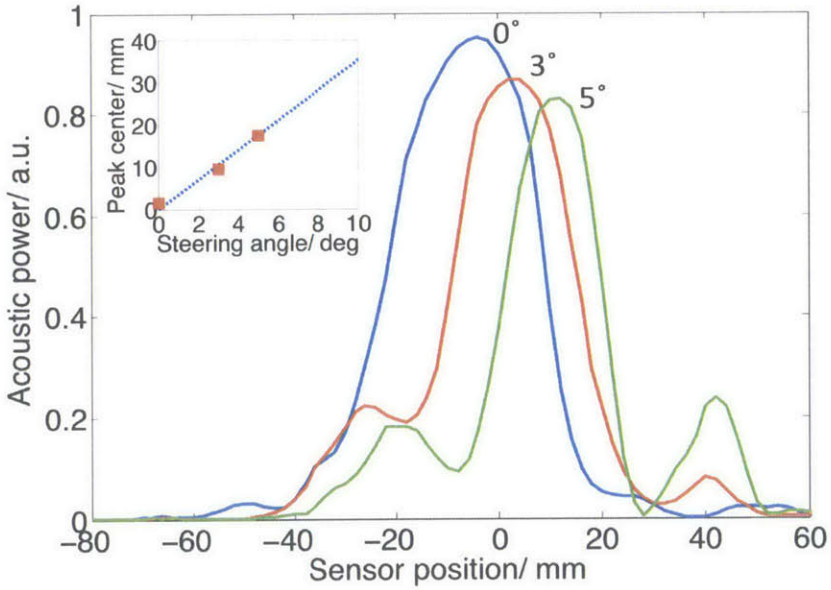

Figure 4.9: Four fiber array: measured acoustic power along x at a distance of y=20mm from the array. Inset : main peak position as a function of the steering angle from the measurements (rectangles) and the theory (dotted line).

4.6 Exploiting the fiber flexibility

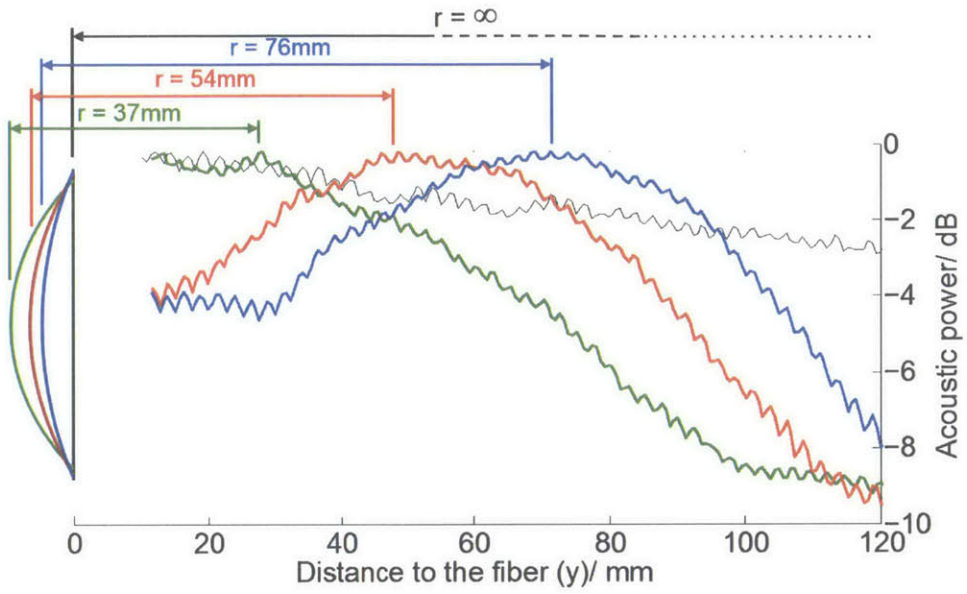

Figure 4.10: Measured acoustic power along the y-axis for different bending radii.

By applying a parabolic phase difference between transducers along the multi-fiber array, one could also focus the acoustic beam [100]. However, the mechanical flexibility of the piezoelectric fibers permits an alternative approach to beam focusing using a single fiber. Indeed, by controlling the bending radius of a piezoelectric fiber, one can focus the acoustic beam at a designated distance from the fiber center. As presented in Figure 4.10, the emission profile of a bent fiber transducer differs radically from that of a straight fiber. Simulations done for 5-cm long fibers emitting at 600kHz show in Figure 4.11 that when the fiber is straight, the near-field region extends beyond 200mm from the fiber. In contrast, with a bent fiber, the acoustic power is concentrated close to the fiber and is focused at a distance approximately equal to the bending radius.

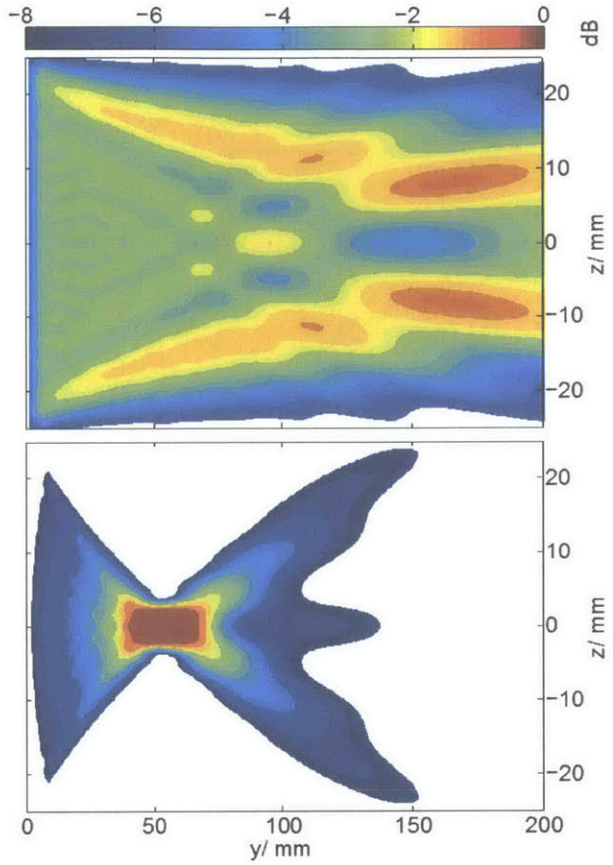

Figure 4.11: Simulation of the acoustic pressure field in the x=0 plane for a flat fiber (top) and for a fiber with bending radius equal to 54mm (bottom).

Measurements were performed using the same underwater set-up as shown in Figure 4.6, but with the piezoceramic transducer traveling along the Y axis, that is, varying its distance to the emitting fiber. The results are shown in Figure 4.10 for bending radii ranging from 37 to 76mm on a 5-cm long fiber, and compared to the emission profile of a straight fiber. These results demonstrate a clear effect of the fiber bending on the presence and location of the focal point, and illustrate the potential to construct flexible acoustic devices that have capabilities beyond those of their rigid counterparts.

4.7 Conclusion

In summary, we have demonstrated materials and structures that allow an enhancement of the performance of piezoelectric fibers through an increased effective area, and the associated large degree of freedom in controlling acoustic fields imparted by the mechanical flexibility. A new large-active-area structure was designed and fabricated and both acoustic and electrical characterization of this device was performed. As a proof-of-concept, two- and four-fiber phased arrays were assembled to show coherent interference and beam steering capabilities. Beam focusing through controlled bending of a single fiber gives a demonstration of the immense potential that lies in the ability of fibers to take arbitrary shapes. The combination of fiber tolerance to bending and twisting, anisotropic angular emission and possibility of assembly in multi-fiber phased arrays creates unprecedented opportunities in the design of large-area conformal acoustic devices. This work paves the way towards large-area, flexible and adjustable acoustic emission and sensing of complex, three-dimensional patterns for a variety of applications.

4.8 Experimental protocols

4.8.1 Preform Preparation and Fiber Drawing

$300\mu m$-thick P(VDF-TrFE) films were prepared from 70:30 molar ratio pellets (Solvey) melt-pressed at 180^oC and 100 bars. They were assembled with $300\mu m$-thick CPE layers (Measurement Specialities) and metallic electrodes ($Bi_{58}Sn_{42}$ eutectic alloy, Indium Corporation) in a polycarbonate bar cladding (McMaster). The preform was consolidated under vacuum at 185^oC for ~20 minutes to remove trapped gas. This final preform was 38mm wide, 11mm thick, and 200mm long. It was then thermally drawn in a three-zone vertical tube furnace with the top-zone temperature at 150^oC, the middle-zone temperature at 230^oC, and the bottom-zone temperature at 110^oC. With this procedure, meters of fibers were drawn with thicknesses ranging from 230 to $370\mu m$ (widths ranged from $800\mu m$ to 1.3mm).

4.8.2 Acoustic measurements

All acoustic measurements were performed in water, using an Olympus immersion transducer V303-SU centered at 1MHz and mounted on a linear motorized stage (Velmex Xslide with VXM stepping motor controller). For the radiation pattern characterization, a time-gate measurement algorithm was used to separate the acoustic signal from the electromagnetic interference, and to eliminate acoustic noise from reflections on the water-tank walls. The fiber device was mounted on a motorized rotational stage (Thorlabs CR1-Z7 with APT-dc servo controller). For the fiber array and flexed fiber measurements, a continuous wave measurement was performed, using silicone foam absorbers along the water-tank walls to minimize reflections. Results shown in Figure 4.10 are obtained by averaging the raw measured acoustic power over one wavelength (2.4mm at 600kHz underwater) around the sensor position and normalizing. Both motorized stages were controlled using a LABVIEW interface.

4.8.3 Electrical measurements

The electrical impedance characterization of the piezoelectric fibers was performed with a Hioki 3532-50 LCR HiTester impedance analyzer. Electrical contacts were made to the $Bi_{58}Sn_{42}$ electrodes by stripping away the polycarbonate cladding and attaching thin wires to the exposed electrodes with conductive silver paint.

4.8.4 Phased array

The digital waveforms used to control the fiber transducers were generated in MATLAB and, using LABVIEW, were loaded into a Byte Paradigm GP 24-100 digital signal generator delivering a square wave which was then filtered by an analog chip in order to remove unwanted higher order harmonics, leaving only the desired fundamental frequency [101]. These filtered waveforms were then amplified and applied to the fiber transducers forming the array.

Chapter 5

Fabrication and characterization of thermally drawn fiber capacitors

5.1 Abstract

We report on the fabrication of all-in-fiber capacitors with poly(vinylidene fluoride) (PVDF) as the dielectric material. Electrodes made of conductive polymer are separated by a PVDF thin film within a polycarbonate casing that is thermally drawn into multiple meters of light-weight, readily-functional fiber. Capacitive response up to 20 kHz is measured and losses at higher-frequencies are accounted for in a materials-based model. A multilayered architecture in which a folded PVDF film separates interdigitated electrodes over an increased area is fabricated. This structure greatly enhances the capacitance, which scales linearly with the fiber length and is unaffected by fiber dimension fluctuations.

5.2 Introduction

Poly(vinylidene fluoride) (PVDF) is a synthetic polymer used in a wide variety of applications [102], ranging from ultrasound transducers [103] to lithium ion batteries [104], thermal sensors [105], outdoor paints [106] and western blots [107]. In particular, it is an attractive dielectric material for polymer film capacitors because of its relatively high dielectric constant and strength [108] as well as its potential as matrix for high-permittivity nanocomposite polymers [109]. Such capacitors can achieve high energy densities [110] as well as high strain sensitivity [111], and the mechanical flexibility of PVDF in these devices presents a great potential for mobile, wearable sensors as well as electrolyte-free energy storage solutions. Yet, although these applications ideally span large areas, the flexibility of PVDF has thus far been exploited in small devices only [112]. The preform-to-fiber thermal-drawing process offers a scalable path to the generation of very large area devices [7], and recent developments in multi-material fiber fabrication have led to the successful inclusion of PVDF-based copolymers in piezoelectric fibers for acoustic transduction and optical modulation [9, 60]. This opens the way to thermal-drawing of high-permittivity polymer fiber capacitors, that are flexible and light-weight. Previous results on polymer fiber capacitors have been reported [113, 114], but the low permittivity of the polyethylene used limits the capacitance per unit volume of dielectric and the fibers lack a well-integrated metallization scheme. Here, we demonstrate the thermal drawing of a fully functional fiber design containing the dielectric layer as well as both metallic and viscous electrodes. We characterize the frequency response of the impedance and account for the observed capacitive behavior and its high-frequency limitations in a materials-based model. A multilayered design comprising a wider, folded PVDF film is then demonstrated and is shown to greatly enhance the capacitance, that scales linearly with the fiber length and is unaffected by possible dimension fluctuations during the draw process.

5.3 Fiber design and fabrication

5.3.1 Single-layer structure

The simplest capacitor architecture involves two planar parallel electrodes separated by an insulating material. In that case, the capacitance is given by:

$$C = \epsilon_d \frac{A}{t} \tag{5.3.1}$$

where ϵ_d is the absolute permittivity of the dielectric layer and t its thickness, while A is the area over which the electrodes are facing. Large capacitance is therefore obtained by placing a thin film of high-permittivity material between conductive domains over a wide surface. The thermal-draw process, in which a macroscopic preform can yield kilometers of axially invariant fiber, is well suited to achieve such large areas. Remarkably, the process leaves the cross-sectional aspect-ratio of all the fiber features unchanged. We therefore see from (5.3.1) that for a given length of fiber containing such a flat capacitor structure, the ratio A/t should not depend on the fiber's final dimensions. The capacitance per unit length is thus entirely set by the chosen dielectric film thickness and width in the preform, allowing the capacitance per unit volume - or per unit weight - of the fiber to be greatly increased as it is drawn thinner.

5.3.2 Materials selection

Thanks to its high permittivity as a polymer - around 10 ϵ_0 at room temperature and 1 kHz [99] - PVDF is a good candidate to achieve high capacitance. However, the choice of PVDF as dielectric material is a challenging one. Indeed, while most polymers routinely used in fiber drawing have high glass-transition temperature and a viscosity that continuously decreases with increased temperature [7], PVDF, a semi-crystalline polymer, melts at a temperature between 158^oC and 197^oC [115]. Such a material is traditionally challenging to draw as a thin layer within a fiber, since large-aspect-ratio, low-viscosity elements are subject to capillary instabilities due to surface tension and can ultimately break-up into smaller elements [11]. Successful drawing of a thin layer of PVDF thus necessitates its confinement within boundaries that remain viscous enough during the draw process. In a capacitor, these boundaries are the electrodes, which must therefore be both viscous and conductive. Commonly employed crystalline metals are thus

unsuitable, and we instead use a composite polymer loaded with carbon particles, Conductive Polyethylene (CPE). Its viscosity enables the drawing of large aspect ratio electrodes that can confine the liquefied PVDF.[9]

5.3.3 Fiber fabrication

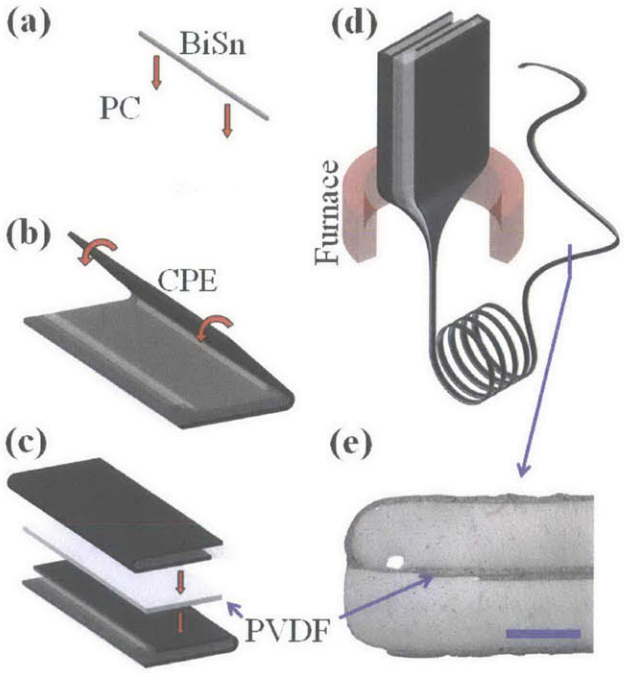

Figure 5.1: Fiber fabrication. (a-d) Fabrication process flow. (e) Optical micrograph of the fiber cross-section: the central PVDF layer is flanked by two layers of CPE (dark gray), wrapped around the surrounding PC (light gray) bars to cover the fiber sides (top and bottom). The $Bi_{58}Sn_{42}$ wire shows in white. Scale bar in (e) is 200 μm.

Figure 5.1(a-d) depicts the process of fabrication of a flat capacitor fiber by scaling down of a macroscopic preform using thermal drawing. Initially, a 5mm-thick bar of polycarbonate (McMaster) is milled to the proper shape and a strip of $Bi_{58}Sn_{42}$ (eutectic alloy, Indium Corporation) is inserted in it. A 400μm-thick CPE sheet (Measurement Specialities) is then wrapped around the rounded edge of the bar and the whole operation is repeated a second time. These two identically prepared elements are then stacked around a 300μm thick PVDF layer (Ajedium Film Group, Solef 10.0) and the structure is consolidated under vacuum at $\sim 185^oC$.

The obtained preform (38mm wide, 11 mm thick, and 200 mm long) is then thermally drawn at $\sim 230^oC$ into tens of meters of flexible fiber. The optical micrograph in Fig. 1(e) depicts the key elements of the fiber cross section: the flat central capacitor structure, the wrapped CPE layers allowing easy electrical connection from the outside and the integrated metallic bus, added to ensure good electrical conduction along potentially extended fiber lengths. Indeed, the conductivity of CPE (1-10 $S.m^{-1}$) [60], while well-suited for conduction within the millimetric fiber cross-section, is not sufficient to ensure a uniform electric potential along meters of fiber [59]. While this effect can be exploited in some cases [59, 116], here it would preclude long fibers from behaving as capacitors (see Figure 5.2).

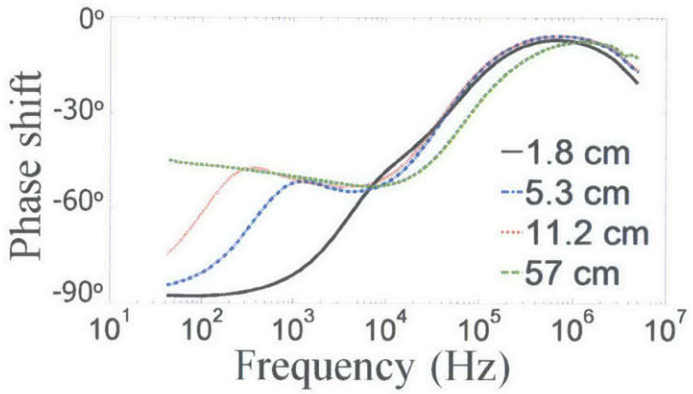

Figure 5.2: Degradation of the impedance phase as a function of frequency for four fibers of increasing lengths with no integrated metal $Bi_{58}Sn_{42}$ bus. The shortest fiber sample (1.8 cm-long, black solid line) has an acceptable capacitor behavior up to 1 kHz and the second shortest (5.3 cm-long, blue dash-dotted line) has losses rising at the lowest measured frequencies. The longer samples (11.2 cm-long, red dotted line; 57 cm-long, green dashed line) never achieve a phase near -90^o in the range of measured frequencies. This result illustrates how critical the presence of a highly-conductive element along the fiber axis is to the proper operation of the capacitor.

5.4 Fiber capacitor electronic properties

5.4.1 Fiber capacitive behavior

The fiber capacitive behavior can be demonstrated from the variations of the fiber complex impedance Z with f, the a.c. frequency of the applied voltage. Using a Hioki 3532-50 LCR HiTester impedance analyzer directly connected to the fiber sides, we record these variations over the [42Hz ; 5MHz] range. Figure 5.3 depicts both the measured modulus $|Z|$ and phase ϕ of Z as f varies.

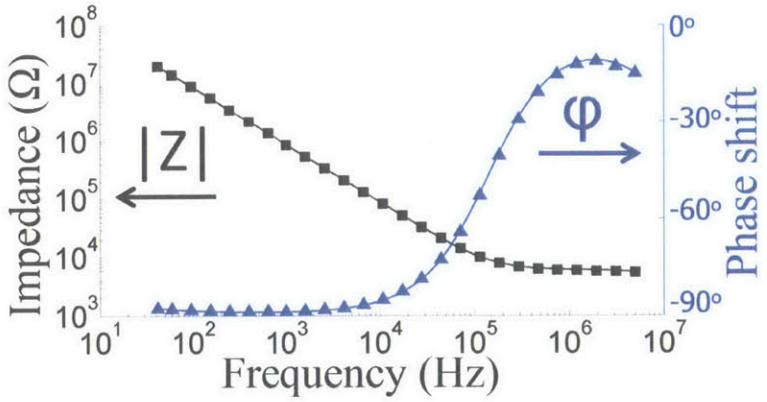

Figure 5.3: Frequency response of the impedance of a 2.4cm flat capacitor fiber sample. Black squares represent the measured complex impedance modulus (left axis), blue triangles its phase (right axis). Black and blue lines are resp. the modeled behavior of $|Z|$ and Φ using the model shown in Figure 5.4 and the polynomial functions obtained from Figure 5.5.

For an ideal capacitor, $|Z|$ would be inversely proportional to f, and ϕ, the phase shift between voltage and current, equal to -90^o at all frequencies. In practice however, capacitors depart from this ideal behavior because of their internal series resistance, which prevents $|Z|$ from dropping indefinitely with f and reduces ϕ, and because of current leakage through the dielectric material, which also impacts ϕ. The quality of the capacitor can be estimated by the dissipation factor DF, defined as [117]:

$$DF = tan(\phi + 90^o) \tag{5.4.1}$$

We see in Figure 5.3 that DF reaches 10% (for $\phi = 84^o$) at 20 kHz and 50% (for $\phi = 63^o$) around 100 kHz, beyond which $|Z|$ plateaus and ϕ drops significantly, setting the upper limit on the frequency of operation of the fiber as a capacitor.

5.4.2 Origin of the fiber limitations

In order to properly identify the origin of these limitations of the capacitor performances, we construct a model for Z that takes the different materials' behavior into account. Thanks to the conductive $Bi_{58}Sn_{42}$ elements, the fiber behaves like a simple series circuit as depicted schematically in Figure 5.4, in which Z is modeled as the sum of the impedances of the different parts of the system: Z_{CPE} for the polymer electrodes, Z_{PVDF} for the PVDF film and a purely resistive term $R_{contact}$ to take into account losses at the connection with the setup.

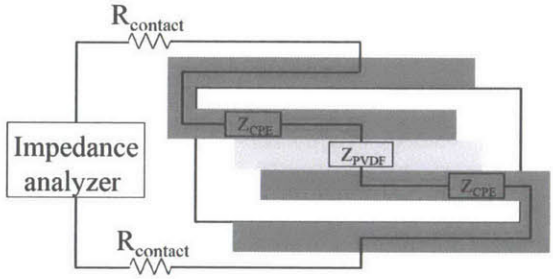

Figure 5.4: Schematic model of a fiber connected to an impedance analyzer.

It has been reported that because of its composite nature, the resistivity of CPE is stable at low frequency but decreases above a critical frequency f_0 whose value highly depends on the polymer treatment [98]. We take this into account by modeling the $Z_{CPE}(f)$ in the following way:

$$Z_{CPE}(f) = \frac{R_{CPE}}{1 + \frac{f}{f_0}} \tag{5.4.2}$$

where R_{CPE} is the low frequency resistance of the electrode. We have repeatedly witnessed this effect in fibers containing CPE and, because the thermal-drawing process itself can greatly impact the value of f_0, we take it as a parameter in this model. The impedance of the PVDF layer is calculated using (5.3.1):

$$Z_{PVDF}(f) = \frac{1}{j\frac{\epsilon_{pvdf}A}{t}2\pi f} \tag{5.4.3}$$

where A, t and ϵ_{pvdf} are respectively the surface area, thickness and dielectric permittivity of the PVDF film inside the fiber. The overall impedance of the system is obtained by summing its constituent parts:

$$Z_0(f) = 2R_{contact} + 2Z_{CPE}(f) + Z_{PVDF}(f) \tag{5.4.4}$$

As seen in (5.4.3), ϵ_{pvdf} is central in setting the capacitance of the fiber device and its variations with the frequency f are expected to impact the fiber response. We measure these variations by gold-coating both sides of a $1cm^2$ portion of a $300\mu m$-thick film of PVDF such as the one placed in the preform, and using the same impedance analyzer as previously. From measured data and (5.4.3), we retrieve the variations of ϵ_{pvdf} with f and show the obtained results in Figure 5.5 for ϵ' and ϵ'', respectively the real and imaginary parts of ϵ_{pvdf}, which are consistent with similar reported measurements [99]. Using MATLAB, the discrete data points obtained are modeled by two fourth-order polynomial functions, shown in solid lines on this same plot.

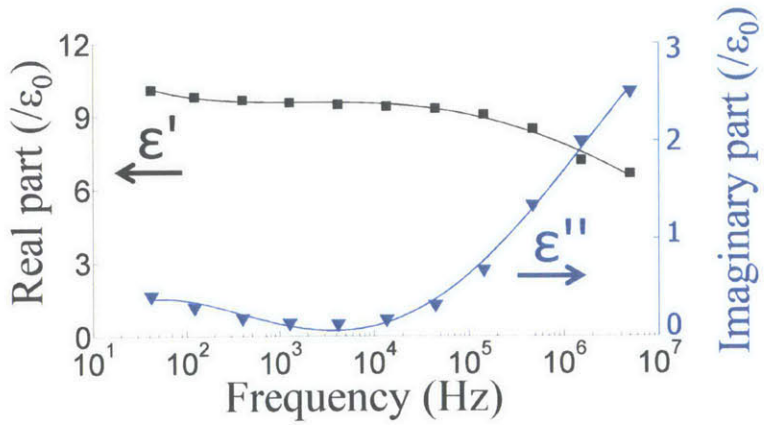

Figure 5.5: Frequency dependence of ϵ_{pvdf} of a $300\mu m$-thick film before thermal draw. Black squares represent the measured real part (left axis), blue triangles the measured imaginary part (right axis). Solid black and blue line are 4^{th} order polynomial approximations of these data.

Although these functions capture accurately the variations of ϵ' and ϵ'' over the range of frequencies of interest for the PVDF film used in the preform, the drawing process is likely to alter ϵ_{pvdf} as PVDF melts and recrystallizes [99]. In our model, we include this effect by keeping $\epsilon'(1kHz)$ and $\epsilon''(1kHz)$ as parameters, and variations of ϵ_{pvdf} with f are assumed to follow the polynomial functions obtained earlier, but scaled proportionally to the change of PVDF permittivity at 1 kHz from the preform to the fiber. The result of fitting (5.4.4) to the measured impedance of the fiber sample is displayed in Figure 5.3. The quality of the fit is excellent for $[R_{contact} = 2.8k\Omega,\ R_{CPE} = 3.0k\Omega,\ f_0 = 10.5MHz,\ \epsilon'(1kHz) = 12.7\epsilon_0, \epsilon''(1kHz) = 0.14\epsilon_0]$, a set of values consistent with previously reported results [60], that indicates a slight increase of the permittivity of PVDF induced by the draw process itself. This model shows that the plateau in $|Z|$ at high frequencies can be lowered by arranging the geometry of the fiber in order to reduce R_{CPE}, so that the ultimate limitation in this fiber is the increased dielectric loss ϵ'' in PVDF above 100 kHz.

5.5 Multilayered fiber internal architecture

5.5.1 Design and fabrication

To increase the fiber capacitance, the dielectric constant of the dielectric layer could be modified. Indeed, nanocomposite materials using PVDF or its co- or ter-polymers as matrix, filled with various ceramic, metallic or organic particles are the center of an active area of research [109], and dielectric constants in the hundreds have already been achieved [118, 119, 120]. However, the fillers in such composites do not only impact the permittivity but also the dielectric strength and, importantly, the mechanical properties of the polymer. Identifying nanocomposite polymers with high permittivity and dielectric strength that remain compatible with the thermal-drawing process calls for a wide-scale study that is beyond the scope of this paper. Nonetheless, other strategies can be developed to enhance the fiber capacitance without replacing the dielectric material. A thinner layer of PVDF can be used, although its low viscosity during the draw makes thinning it down below a few microns challenging. A more efficient strategy consists in increasing the electrodes' surface area per unit length of fiber, by expanding the fraction of fiber volume taken by the capacitive structure. We demonstrate here an evolved

fiber design, in which the internal architecture of the fiber is made of interdigitated CPE electrodes, separated by a folded PVDF film. This structure is inspired from Multi-Layered Ceramic Capacitors [121], as it yields large effective electrode area per unit volume and can easily be reproduced with polymer films.

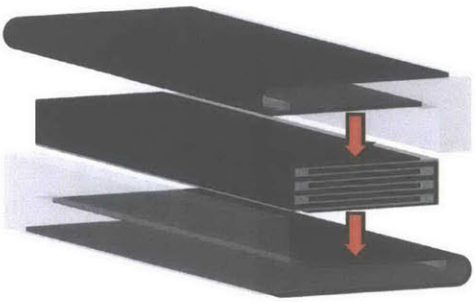

Figure 5.6: A multilayered structure of interdigitated CPE layers separated by a PVDF thin-film replaces the single layer of PVDF of Figure 5.1(c) in the fabrication process, otherwise unchanged.

As shown in Figure 5.6, the fabrication process differs from the one shown in Figure 5.1 only in the fact that a multilayered structure is now placed between the prepared PC bars instead of a single layer of PVDF. The rest of the fiber fabrication process is identical, and a typical cross-section of the obtained fiber is shown in Figure 5.7 for a structure where the PVDF layer is folded 6 times.

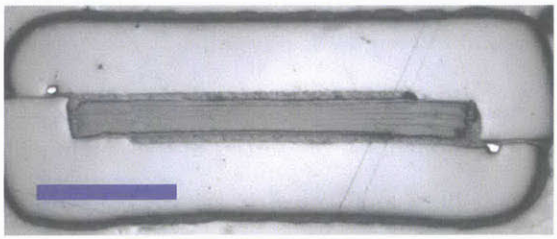

Figure 5.7: Optical micrograph of a fiber cross-sectional structure containing a 6-fold PVDF structure as depicted in Figure 5.6. Scale bar is 300 μm.

Figure 5.8 shows the tip of the CPE "fingers" and demonstrates that PVDF successfully maintains its structural integrity during the draw. With this approach, fiber capacitors with much greater internal surface area of electrode can be produced, and the active volume inside the fiber is increased as well.

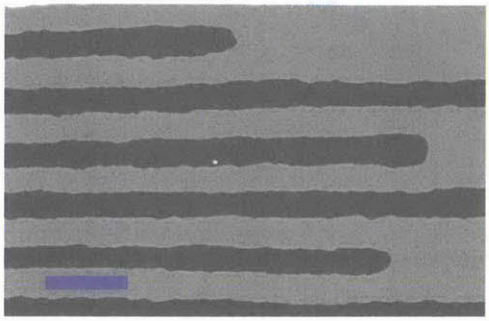

Figure 5.8: SEM micrograph of the layered structure: the CPE "fingers" (dark gray) are separated by the folded PVDF layer (light gray). Scale bar is 20 μm.

5.5.2 Experimental results

To demonstrate the efficiency of this strategy in enhancing the fiber capacitance, three preforms with different architectures were fabricated and drawn into fibers. The first contained a single 300 μm-thick PVDF film as depicted in Figure 5.1, with CPE electrodes facing over 18 mm in the preform cross-section. The second one had a twice-folded 225 μm-thick PVDF film, separating a width of 60 mm of CPE electrodes. The last was the one depicted in Figure 5.7, with a six-times-folded 300 μm-thick PVDF film, spanning 126 mm in electrode width. Using (5.3.1) and the in-fiber PVDF dielectric constant of 12.7 ϵ_0 obtained from the previous model at 1 kHz yields expected capacitance per unit length values of respectively 6.7 $nF.m^{-1}$, 30 $nF.m^{-1}$ and 47 $nF.m^{-1}$ for these three fibers. In Figure 5.9, we display the measured capacitance of fiber samples as a function of their length for these three architectures.

The values obtained from the linear fit to the data points are respectively 6 $nF.m^{-1}$, 32 $nF.m^{-1}$ and 49 $nF.m^{-1}$, in excellent agreement with the predictions, which indicates limited variations in the way PVDF crystallizes at the end of the drawing process from one fiber to the next and a maintained aspect ratio of the drawn PVDF film from preform to fiber. Indeed,

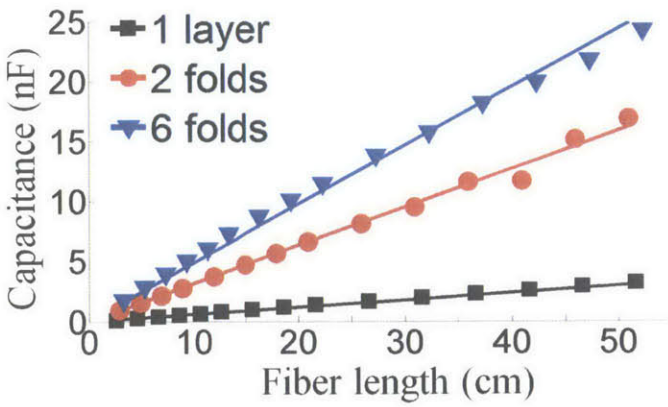

Figure 5.9: Measured capacitance of fiber samples as a function of the fiber length for 3 different designs: single-layer (black squares), twice-folded (red circles) and six-times-folded (blue triangles) PVDF thin-film. The straight lines are linear fits to the data, with slopes of 6 $nF.m^{-1}$, 32 $nF.m^{-1}$ and 49 $nF.m^{-1}$, respectively.

for each fiber, the tested samples had variable cross-sectional dimensions, and these measurements validate the independence of the linear capacitance on these fluctuations. The result on Figure 5.9 demonstrates the validity of the multilayered approach in enhancing the fiber capacitance, as this method can be scaled so as to increase even more the active volume within the fiber.

5.6 Conclusion

In summary, we have demonstrated an all-in-fiber capacitor using poly(vinylidene fluoride) (PVDF) as dielectric material. The low-loss capacitive behavior up to 20 kHz of the device is established and the high-frequency behavior is accounted for by the materials properties. Using CPE, a viscous conductive material for the electrodes, multilayered structures comprised of high aspect ratio films are successfully drawn and yield high capacitance that scales linearly with the fiber length.

Chapter 6

In-silica-fiber silicon spheres and devices via thermal-gradient-induced capillary instabilities

6.1 Abstract

The ability to produce small scale, crystalline silicon spheres is of significant technological and scientific importance yet scalable methods for doing so have remained elusive. A continuous silica cladded silicon core fiber with diameters down to 340nm is continuously fed into a flame which defines an axial thermal gradient. A cross sectional melting plane and a short axial molten silicon section develop, which in-turn undergoes capillary breakup resulting in the formation of spheres internal to the fiber. The continuous formation of spheres whose size is controlled by the feed speed is demonstrated. In particular, spheres of diameter < 500nm smaller than those produced under isothermal heating conditions are shown and analyzed. A silicon-in-silica fiber with dual cores: p-type and n-type silicon is drawn and processed into spheres. Spatially coherent breakup leads to the joining of the spheres into a bi-spherical silicon "pn molecule". The resulting device is measured to reveal a rectifying I-V curve consistent with the formation of a pn junction.

6.2 Introduction

Silicon spheres have been the subject of recent investigations in a broad range of fields spanning mechanics [122], biotechnology [123], photonics [124] and green energy [125]. A variety of bottom-up [126, 127, 128] and top-down [124, 129, 130] methods have been developed to address the need for silicon spheres ranging in size from the nm to mm scale. However, to date, no single fabrication methodology exists that is simultaneously scalable in size and quantity over the full spectrum of radii. Recent breakthroughs [131, 12, 11, 132] in harnessing fluidic instabilities for nanofabrication define a promising direction towards new and scalable methods, but are currently restricted because of the isothermal profile. For example in cases involving high viscosity-contrast materials systems [133, 134, 135] such as silicon in silica, the isothermal breakup condition [134] would dictate a large breakup wavelength λ_T and correspondingly large particles.

Here, we report on a method for producing silicon spheres in a silica fiber [136] in which capillary breakup is controlled by an axial thermal gradient and a controlled feed speed. In our process, the fiber is fed into a spatially localized flame at a controlled rate, so that melting of the silicon occurs at a fixed location in space, beyond which a molten silicon cylinder cladded by softened silica develops. Capillary instability causes the core to break up into a sphere in order to reduce its surface energy. A close analogy is the use of flow rate to control droplet formation in dripping faucets [137, 138]. By continuously feeding the fiber into the flame a string of particles emerges, the size of which is below that of an isothermal process and approaches the fundamental diameter limit.

6.3 Results

6.3.1 Challenges in entering the micron-pitch break-up regime

The generation of submicron silicon spheres via a fluid instability mechanism requires very small core diameters to begin with, since the size of the sphere cannot be smaller than $\sqrt[3]{\frac{3\pi}{2}}D$ (correspondent to wavelength πD - the wavelength equal to the core circumference), where D is the diameter of the core. To generate small cores a multistep process is developed: A 2 mm thick silicon rod clad by an 8 mm thick silica tube is thermally drawn to a silicon core size of 130 μm and redrawn to achieve a core size of 4 μm (see section 6.5, Figures 6.19 and 6.20 for details) , as shown in Figure 6.1.

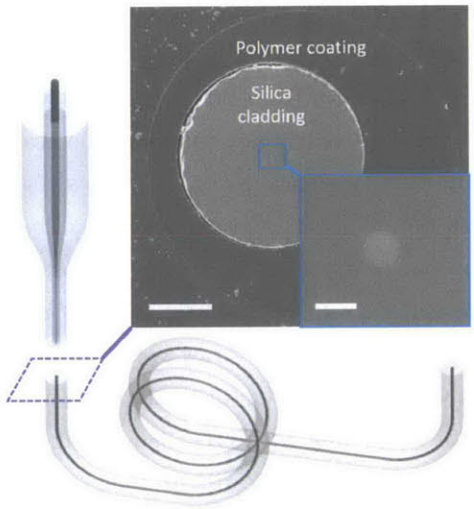

Figure 6.1: Schematic representation and experimental results of a redrawn silicon-core fiber. (Scale bars: left = 100 μm, right (inset) = 5 μm).

The resulting twice-drawn fiber is redrawn under high tension in a hydrogen flame. A relatively fast feed speed (3 mm/min) and relatively slow draw speed (15 mm/min) scales the fiber by a factor of $\sqrt{5}$ while keeping the silicon core intact and without inducing any cracking. This step can be repeated multiple times until the desired silicon-core diameter is obtained (see section 6.5 for details), and the results are depicted in Figure 6.2. Starting with a 4 micron silicon-core fiber, a triple rescaling leads to a continuous silicon-core fiber with a diameter of

(340 ± 15) nm.

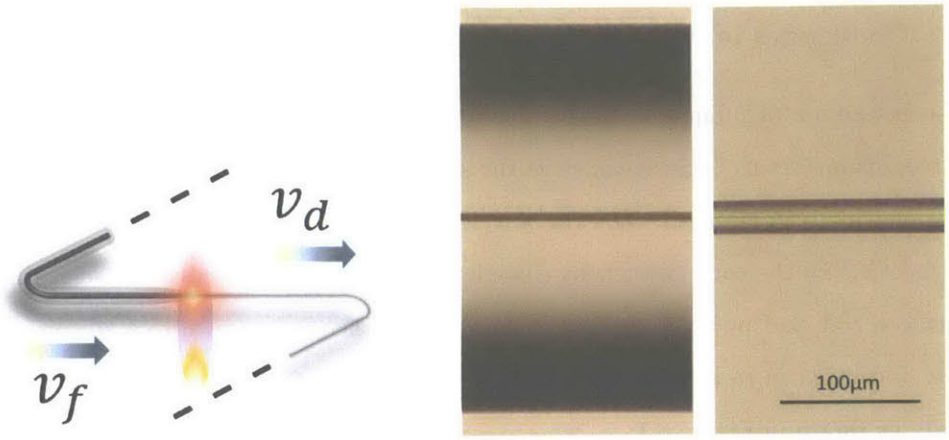

Figure 6.2: Left: Schematics of a high-tension redraw process that allows, upon repeated application, continuous reduction of the silicon-core towards the deep submicron regime; Center and Right: side views of the fiber used for torch-scaling process with OD=280 μm and D=4 μm (center) and the side view of the fiber after the triple-iteration scaling (right). This is a typical result of the fiber high-tension low-ratio downscaling using a hydrogen torch. The scaling process here is applied to a fiber with outer diameter of the silica cladding of OD=280 μm and a core diameter of D=4 μm and consists of 3 scaling redraw iterations. The first redraw is conducted using a heating flame resulting from a hydrogen flow of 0.23 $l.min^{-1}$, second of 0.21 $l.min^{-1}$ and third of 0.19 $l.min^{-1}$. Feed speed v_f and draw speed v_d were chosen to be 0.05 $mm.s^{-1}$ and 0.25 $mm.s^{-1}$, respectively. The scaling factor of the fiber cross section resulting from one iteration is $n = \sqrt{v_d/v_f} = \sqrt{5}$. Beginning with OD=280 μm after a triple-iteration process we should end with OD′=OD x $5^{-\frac{3}{2}}$=25 μm. We estimate geometrically from those pictures, given OD=280 μm and D=4 μm for the original fiber, that the resulting OD′=(24 ± 1) μm, assuming that the cross sectional geometry of the fiber is preserved, which is a reasonable assumption for the high tension draw process. The resulting core size is expected to be D′=(340 ± 15) nm.

In the isothermal regime, perturbations to an infinitely long cylinder of diameter D develop into periodic breakup, resulting in a chain of spheres [133]. In the treatment of this problem by Tomotika [134], an instability growth rate $\sigma(\lambda)$ is associated with each perturbation wavelength $\lambda \in [\pi D; \infty]$, the wavelength λ_T with the fastest growth rate sets the observed breakup period. λ_T depends on the materials' viscosity ratio, and thus should vary with the chosen temperature. However, for any temperature above the silicon melting (1,414 ^{o}C) this ratio remains in the 10^8

– 10^{12} range, resulting in $\lambda_T \gg \pi D$ (see Figure 6.3).

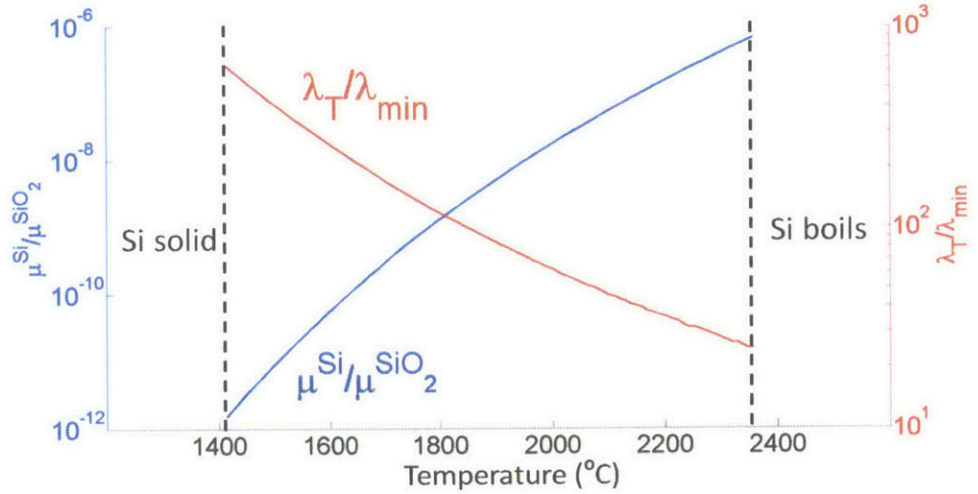

Figure 6.3: Viscosity ratio $\frac{\mu^{Si}}{\mu^{SiO_2}}$ (solid blue line - left axis) and resulting dominant period λ_T as a function of uniform heating temperature T [139, 140]. λ_T is displayed relative to its minimal possible value, $\lambda_{min} = \pi D$ (solid red line - right axis), and the ratio is thus independent of the core size. Despite its large variations with T, $\frac{\mu^{Si}}{\mu^{SiO_2}}$ remains very small, which means that the dominant wavelength λ_T is always tens to hundreds of times larger than the smallest physically achievable breakup period, λ_{min} Since the final sphere size is tied to the breakup period via volume conservation, the naturally dominant long breakup periods under uniform heating make this method unsuitable to yield submicron spheres.

What will happen if the cylinder is neither infinite nor uniformly heated, but instead is dynamically fed into a flame causing the cylinder to melt? We argue that under this condition, droplet formation will occur at the cylinder tip, and that spheres will break off it with a period that is set by the feed speed, as schematically represented in Figure 6.4.

If this speed is slow enough, much smaller spheres than those obtained via uniform heating are expected to be formed. Based on this insight, we developed a process in which the fiber is fed through the hot spot of a hydrogen/oxygen flame at a constant speed v_f. As predicted, we observed that silicon spheres break off of the fiber core one by one at regular intervals, as shown in Figure 6.5.

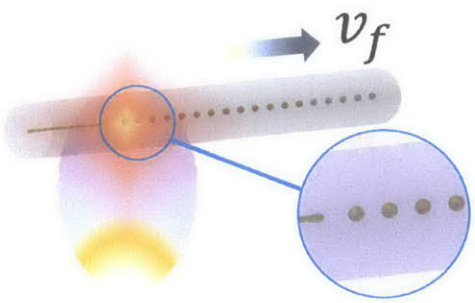

Figure 6.4: Schematics of the gradual liquefaction technique.

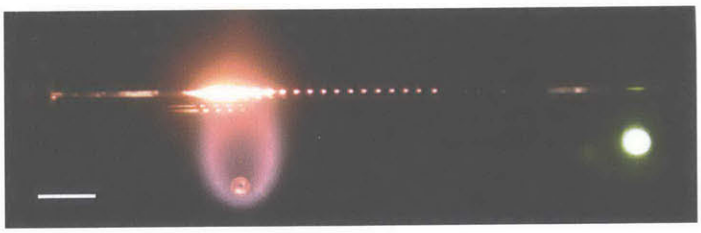

Figure 6.5: Photograph of a typical break-up experiment of 4 μm silicon-core fiber under pure hydrogen flow of 0.8 $l.min^{-1}$ and v_f of 10 $\mu m.s^{-1}$ (scale bar, 5 mm). The break-up period is 1.2mm and the resulting sphere size is 31 μm

Figure 6.6 show, for a $4\mu m$ silicon-core fiber, how slower feed speeds successfully induce the formation of smaller silicon spheres. A simple dimensional analysis can account for this scaling of the observed "dominant" breakup period λ_d with v_f. Indeed, for a given feed speed and in steady state, spheres detach from the silicon core at a fixed location in space: the pinch-off point $x = x_p$. As schematically depicted in Figure 6.7 (where x=0 corresponds to the silicon melting front), the silicon/silica interfacial tension γ_p at $x = x_p$ drives the core pinching with a characteristic velocity $u_p \sim \frac{\gamma_p}{\mu_p^{SiO_2}}$, where $\mu_p^{SiO_2}$ is the local silica viscosity (see section 6.5 for details).

Therefore, λ_d is the length of silicon fed during the time $\frac{D}{2u_p}$ needed for the core to pinch-off, and we can thus write $\lambda_d \sim v_f \frac{D\mu_p^{SiO_2}}{2\gamma_p}$. This expression seemingly implies a linear scaling of λ_d with v_f, but in reality, x_p depends on the feed speed: as v_f is increased, pinch-off occurs deeper into the flame, where the higher temperature in turn yields faster pinching speeds. This explains the sub-linear trend of $\lambda_d(v_f)$ displayed in Figure 6.6c. Importantly, with the new technique,

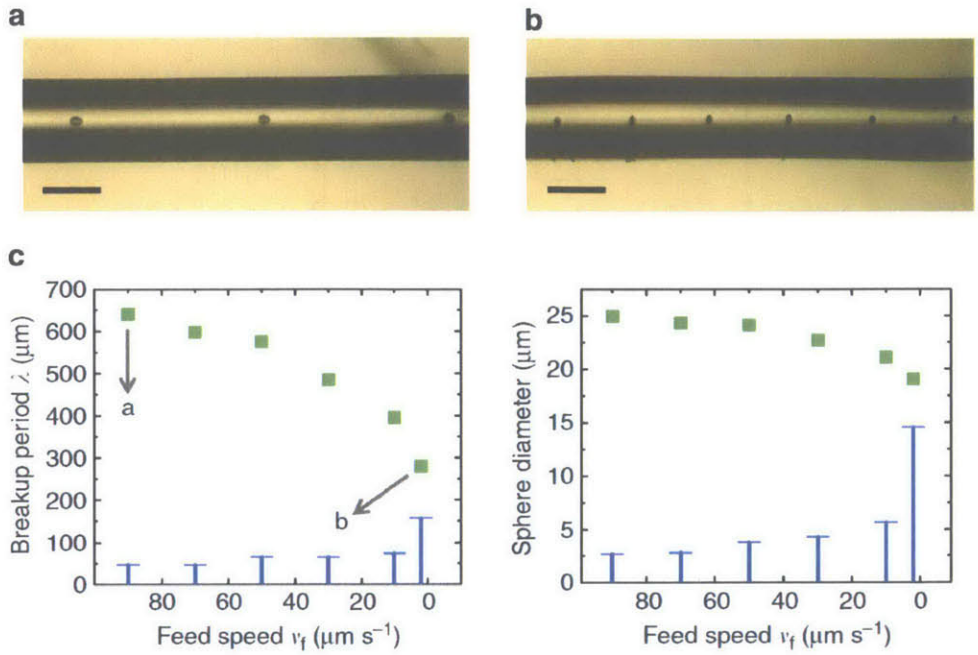

Figure 6.6: (a) Typical high feed speed ($v_f = 90\,\mu m.s^{-1}$) break-up result in 4 μm silicon-core fiber (scale bar, 200 μm). (b) Typical low feed speed ($v_f = 2\,\mu m.s^{-1}$) break-up result in 4 μm silicon-core fiber (scale bar, 200 μm). (c) Break-up periods and corresponding sphere diameters (squares) as a function of the feed speed for the 4 μm silicon-core fiber shown together with the magnified graphs of standard deviation values (bars) as they appear within each one of the samples. fiber sections were fed through the hot zone of the hydrogen/oxygen flame at flows of 0.3 and 0.1 $l.min^{-1}$, respectively. In each experiment only the feed speed of the fiber through the flame is varied. The standard deviation values in the break-up periods are shown 10-fold magnified while in sphere diameters—1,000-fold magnified.

the control over v_f provides an additional independent knob for tuning the breakup period much more practical than varying the temperature to change the viscosity contrast. This novel control enables, as illustrated in Figure 6.6c for this particular example, to reduce the breakup period by a factor of 2 by varying v_f, which in turns reduces the spheres diameter by 20%.

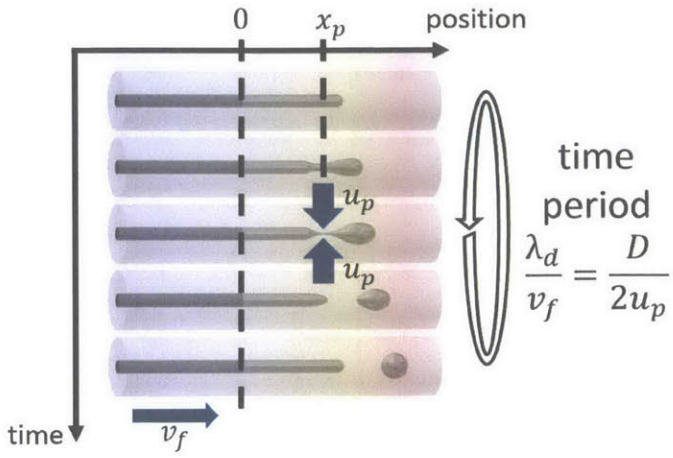

Figure 6.7: Schematic of the step-by-step formation of a sphere and dimensional analysis: in the time it takes to go over one full cycle of sphere formation, in which a length λ_d is fed at speed v_f, the core of diameter D is pinched at a speed u_p.

6.3.2 Patterning of the core into a necklace of submicron beads

Fabrication of 100 nm-scale silicon spheres is achieved by first fabricating a fiber with a 23 μm diameter silica cladding and 325 nm diameter silicon core. This fiber is then fed at 10 $\mu m.s^{-1}$ through the hot zone of the hydrogen/oxygen flame, while the gas flow rates are set to 0.17 and 0.08 $l.min^{-1}$, respectively. The typical fiber-embedded silicon sphere chain imaged using an optical confocal microscope is shown in Figure 6.8.

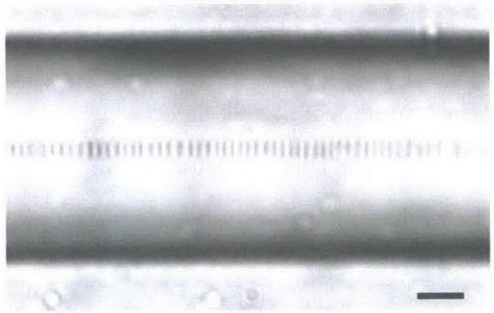

Figure 6.8: Spheres embedded in a silica fiber as observed using a confocal microscope in transmission mode (scale bar, 5 μm).

The spheres are actually imaged as narrow crosses rather than circular disk patterns. Interestingly, this pattern arises from the astigmatism imposed by the cylindrical lens formed by the fiber surface [141, 142]. Note, that the method is not limited to fabrication of submicron spheres but is actually widely scalable as is demonstrated in Figure 6.9.

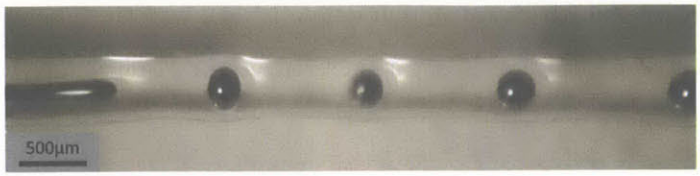

Figure 6.9: Largest spheres produced: the frame shows optical microscope snapshot in a reflection mode of a 100 μm core fiber breaking up into 250 μm spheres. Breakup conditions are: hydrogen flow – 0.47 $l.min^{-1}$, oxygen flow – 0.31 $l.min^{-1}$, feed speed 10 $\mu m.s^{-1}$. This proves the scalability in size of the sphere fabrication process over 3 orders of magnitude between the scales of hundreds of nanometers to hundreds of microns.

The spheres are released from the silica by etching out the fiber cladding using hydrofluoric acid (HF) and imaged using the scanning electron microscope (SEM) as shown in Figure 6.10.

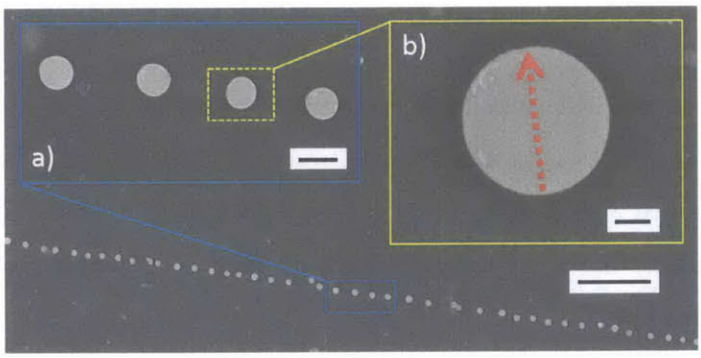

Figure 6.10: The spheres released from the fiber land at the bottom of the container while maintaining the location where they are released. Thus, the resulting chain of spheres mimics the axis of the original fiber (scale bar, 5 μm). Insets depict: (a) Enlarged section of the chain giving a sense of the sphere diameter uniformity (scale bar, 0.5 μm). (b) Individual sphere image giving a sense of the sphere shape quality. The dashed red line depicts the meridian along which seven (roughly equally spaced) 20 keV EBSD measurements were performed on a similar sphere. The beginning of the line and arrow tip refer to the location of the first and last measurement, respectively (scale bar, 100 nm).

Statistical analysis on SEM-imaged spheres reveals that the diameter distribution fits to a normal distribution centered at (460 ± 24) nm, with an average pitch of (1.4 ± 0.3) μm, which is uniform over a cm length scale. Note, that this pitch size is closely approaching the ultimate limit achievable by capillary breakup phenomena - $\lambda = \pi D = 1\mu m$, which is unapproachable by isothermal breakup. Electron backscatter diffraction (EBSD) on a single sphere surface shows a diffraction pattern across the entire sphere meridian suggests the sphere is composed of diamond cubic silicon, as seen in Figure 6.11.

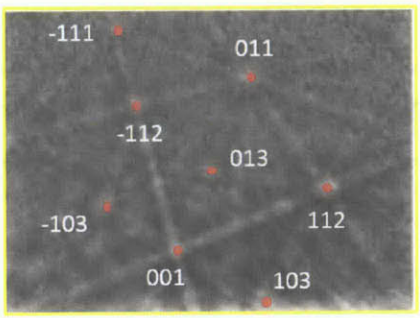

Figure 6.11: Diffraction pattern averaged from five EBSD measurements (excluding edges) shows good agreement with diamond cubic silicon.

To obtain an in-depth understanding of the structure of the silicon sphere, a cross sectional sample was prepared for transmission electron microscopy (TEM) using focused ion beam (FIB) (Figure 6.12). Selected area electron diffraction (SAD) of the core of the representative silicon sphere reveals that the silicon is diamond cubic and multi-crystalline, with several grains comprising the bulk of the volume.

It is well established that the oxygen solubility in equilibrium diamond cubic silicon does not exceed fractions of a percent [143, 144] and that the main origin of oxygen in polycrystalline silicon is oxide formation at the grain boundaries [145, 146, 147]. To investigate the possible oxide formation at the grain boundaries, we use energy dispersive x-ray spectroscopy (EDX) to qualitatively map the distribution of oxygen within the sphere core (Figure 6.12b). EDX line scan does not reveal any increase in the oxygen signal at grain boundaries, indicating that that the oxygen content in the silicon core is below the detection limit of EDX [148, 149] and that the multi-crystalline silicon spheres may be sufficiently pristine for electronic applications. An

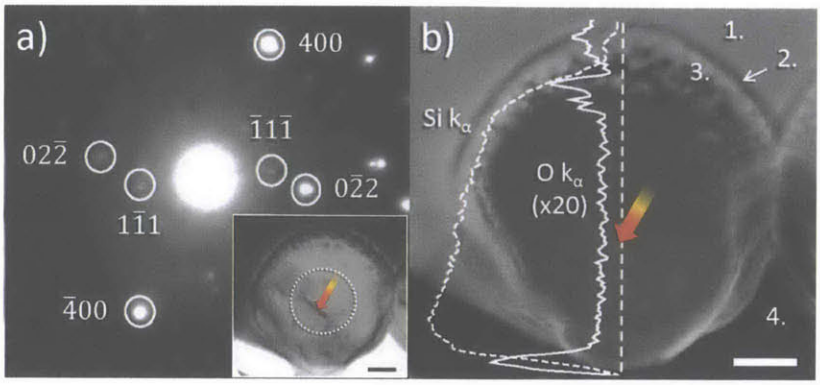

Figure 6.12: (a) Selected area electron diffraction pattern, from the region indicated by the dashed circle on the inset, confirming that the core is composed of multiple diamond cubic silicon grains. Indexed 400, 022 and 111 spots highlight three distinct grains within the selected region. The inset shows cross-sectional bright-field TEM image of silicon sphere prepared using focused ion beam. (b) Dark-field STEM image of the silicon sphere cross-section with overlaid EDX line scan. EDX is unable to detect increased oxygen concentration in the silicon-core or at the grain boundary (indicated by flame-coloured arrows) visible in the inset of **a** (scale bar, 100 nm). Labels indicate deposited protective layers (1: Pt, 2: C, 3: Au and Pd) and 4: voids milled by focused ion beam.

increase in oxygen is observed on the surface of the sphere, supporting the previous observation of an oxide-rich shell forming on the surface, but the deposition of a protective layer of Au-Pd on the surface inhibits further structural characterization of the porous silicon on the surface.

TEM was used to better elucidate the microstructure of the whole silicon spheres in addition to SEM imaging in Figure 6.10. A TEM micrograph of a single sphere, shown in Figure 6.13a, gives evidence of a porous shell on the sphere surface. The shell is composed of crystalline silicon 'fingers' (Figure 6.13b) protruding from the core and is presumably where an interpenetrated silicon/silica mixture formed at the interface between the silicon sphere and the silicon cladding. The material forming the 'fingers' was confirmed to be silicon by obtaining its lattice constant [37] based on high-resolution TEM images (Figure 6.13b (inset)). We hypothesize that these interpenetrated fingers are either a result of the silicon expansion upon crystallizing in a silica cavity of dimensions that correspond to the liquid silicon, in which case the fingers provide a mechanism for stress release, or a result of diffusion of silicon into surrounding silica [150]

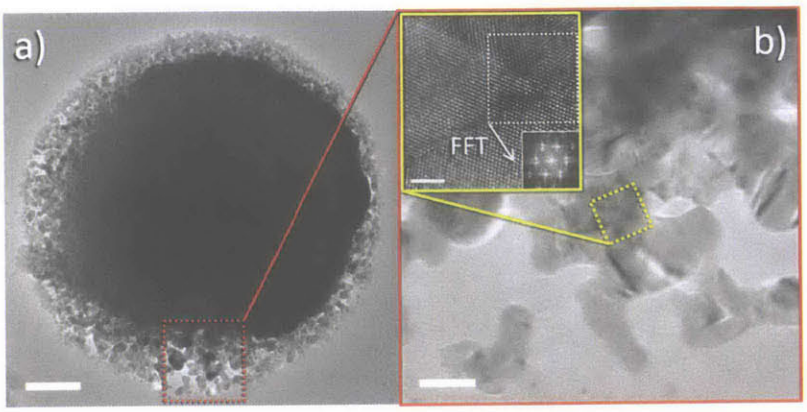

Figure 6.13: (a) Bright-field TEM image of a silicon sphere, which reveals the core-shell structure (scale bar, 100 nm). (b) Zoomed view of the shell section showing individual silicon 'fingers' (scale bar, 20 nm). Inset: high-resolution TEM of silicon fingers (scale bar, 2 nm). FFT confirms crystallinity and detects multiple grains of diamond cubic silicon oriented on the [110] zone axis. The measured lattice constant is (0.538 ± 0.008) nm, which is consistent with the literature value 0.543 nm [37].

with consequent precipitation of it into silicon nano-clusters [151] due to prolonged thermal treatment, or a combination of both.

6.3.3 Contact-by-break-up for fabrication of electronic devices

6.3.3.1 Fabrication

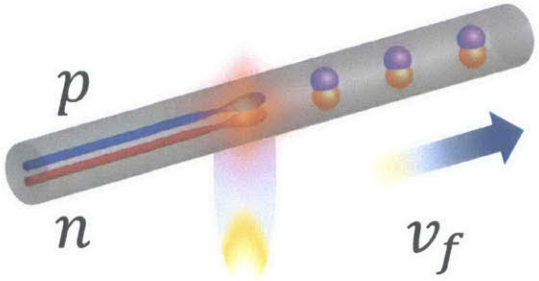

Figure 6.14: Schematics of break-up of a double-core fiber into bispherical clusters (p- and n-type cores are shown in blue and red, respectively).

In addition to the utility of the gradual-heating approach for nanosphere fabrication, this technique facilitates multi-core breakup as a device fabrication tool. In contrast to the uniform-heating method [131, 12], which spatially initiate breakup randomly, the local gradual liquefaction inherent to the novel method homogenizes the structural imperfections of the fiber, thus enabling the simultaneous breakup of multiple equal-diameter cores at the same axial position. This allows coherent patterning of multi-cored fibers, in which detachment of droplets from each core occurs in unison. Since by conservation of volume the diameter of a sphere is always larger than the cylinder from which it breaks, spheres detaching from multiple closely-separated cores can come in contact to form multi-spherical clusters as shown in Figure 6.14 schematically for a dual core silicon fiber and confirmed experimentally as shown in Figure 6.15. Specifically, if the distance between multiple cores is smaller than the diameter of the generated spheres, complex structures made of partially merged spheres can be formed, a process we coin contact-by-breakup (CBB).

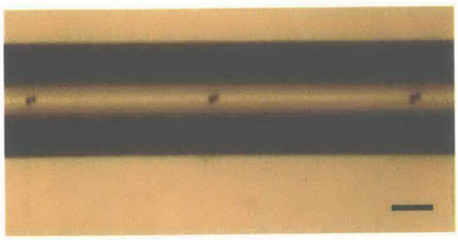

Figure 6.15: The resulting chain of bispherical particles as an outcome of process in Figure 6.14 (scale bar, 100 μm).

As a proof-of-concept of the viability of CBB, we fabricate a chain of bispherical pn particles from the breakup of a dual-core fiber comprised of an p-type and an n-type core. Surprisingly, even though the dwell time of the paired pn cluster in the hot zone is much longer than the typical breakup time, we experimentally observe that upon formation, the cluster, as seen in Figure 6.16, does not reshape into a single large sphere. Instead, it remains in the form of a bispherical cluster. This likely results from the presence of the aforementioned mixture layer membrane on the contact surface between the merged spheres, in analogy to the case where two occasionally touching soap bubbles merge into a single "double bubble" with a thin membrane in between [152].

6.3.3.2 Identification of the p-n junction and IV-curve analysis

When inducing simultaneous breakup of parallel silicon cores containing dopants of different natures and concentration, physical contact between the formed spheres can be achieved as is illustrated and demonstrated in Figure 6.15. However, because of the chances of partial mixing of the liquid silicon as well as possible inter-sphere dopant diffusion during the cooling down or on the contrary, the possibility that poor bonding of the two spheres at their shared interface might prevent an electrical contact to be formed, electrical measurements are required to properly establish the existence of a p-n junction. Figure 6.16 schematically depicts the testing setup for the formed devices, after HF acid etching.

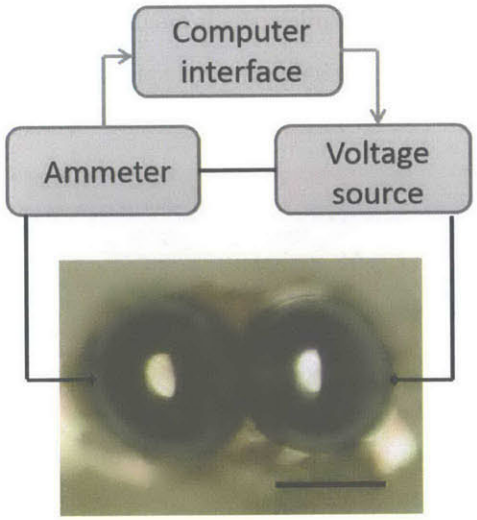

Figure 6.16: Block diagram together with a bispherical pn cluster composed of n- and p-type spheres, fused together by the simultaneous break-up of two closely separated cores. p-type core has acceptors concentration $N_A = 6.9\text{x}10^{18} cm^{-3}$ and the n-type core has donors concentration $N_D = 1.6\text{x}10^{19} cm^{-3}$. High dopants concentrations were chosen so as to ensure satisfactory current conduction through direct contact using tungsten needles (scale bar, $50\mu m$).

Figure 6.17 displays the current-voltage characteristics of a p-n diode, which clearly displays rectifying behavior, consistent with the polarity of the device. The membrane of interpenetrated silicon/silica composite between the p- and the n- halves of the merged cluster could act as a diffusion barrier for dopants, thus allows maintaining electronic properties of the junction. With-

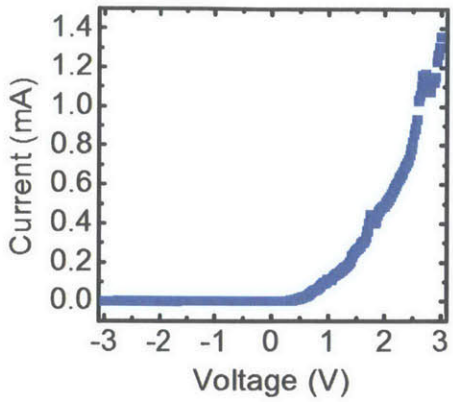

Figure 6.17: I–V curve for the pn diode.

out this layer, the dopants would likely completely homogenize over the entire cluster volume. At the same time, this layer remains electrically conductive due to sufficient concentration of crystalline silicon.

For practical reasons due to the atypical geometries of the globular structures we fabricate, ion implantation or other techniques of heavy-doping of the silicon outer surface (such as spin-on-dopant) are not readily available to us. For this reason, in this proof of concept we have chosen to use n- and p- silicon with the highest concentrations of dopants available to us, in order to enable direct electrical probing using tungsten needles. Ideally, degenerate silicon elements would be employed to that effect, namely n-type silicon with an electron donors' concentration N_D in excess of $2.86\text{x}10^{19}cm^{-3}$ and p-type- silicon with an electron acceptors' concentration N_A in excess of $3.1\text{x}10^{19}cm^{-3}$, but such high concentrations were not available in the 2mm-diameter rods format used in the initial step of our process. While the n-type silicon used in this experiment was close to degenerate level ($N_D = 1.6\text{x}10^{19}cm^{-3}$), the p-type silicon had a dopant concentration nearly one order of magnitude below optimum ($N_A = 6.9\text{x}10^{18}cm^{-3}$), which calls for a verification that contacts with external tungsten needles are not themselves rectifying. This is done by testing, for the p-n junction disclosed in this work, that current can flow both ways through each sphere when probed individually, with satisfactory levels of conduction. Figure 6.18 displays the current-voltage characteristics obtained when both probes were sitting on either sphere, as well as the IV curve obtained when applying a voltage across

the interface between the spheres (i.e. the same IV curse as depicted in Figure 6.17, except in semilog scale this time).

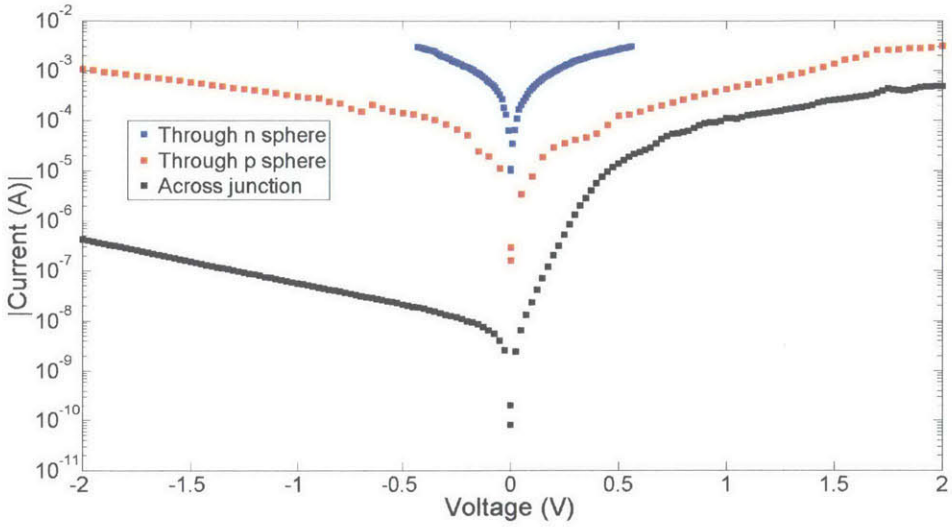

Figure 6.18: Current-voltage characteristics (semilog) of the pn-diode (black) and of its constituent p-type silicon (red) and n-type silicon (blue) spheres. Current was capped at 3 mA to prevent possible damages to the structure, limiting the range of voltages applied to the most conductive n-type sphere.

When testing the conduction through each sphere individually, the external probe tips were between 10 and 30 μm apart, while both types of silicon have a rather small bulk resistivity ($\rho_n = 4\text{x}10^{-3}\ \Omega.cm$ for the n-type and $\rho_p\text{x}10^{-2}\ \Omega.cm$ for p-type, as specified by the supplier). This yields expected resistances of the conduction paths within silicon that, although dependent on the exact positions of the probes, are in the order of 1 to 10 Ω (for n-type and p-type respectively). The data displayed in Figure 6.18 is however consistent with series resistances comprised between 180Ω and 300Ω for the n-type sphere and between 0.65$k\Omega$ and 8$k\Omega$ for the p-type sphere. Note that we give ranges to account for the small non-linearity of these characteristics, a consequence of the dopants concentrations being below the degenerate levels - as mentioned above.

The conclusion that we can draw from this analysis is that for both the n-type silicon and the p-type silicon used in this study, it is the contact properties between the external probes

and the spheres - rather than the distance between the probe-tips itself - that sets the dominant series resistance. We can therefore readily compare the different curves shown in Figure 6.18, regardless of the small differences in probe tips locations between measurements. While at first we could try to account for the effective blocking of the reverse current across the junction (black squares) by invoking the presence of a highly resistant path (with a resistance superior to $10M\Omega$) between the spheres, this hypothesis does not hold when considering the much smaller overall resistance (down to a few $k\Omega$) measured in the forward regime. The electrical behavior of the structure we have fabricated is clearly rectifying, a property that can only be explained by the presence of a p-n junction at the interface between the two spheres. This also indicates that the silicon/silica mixture shells surrounding the spheres upon formation (as seen in Figure 6.13), while apparently acting as barriers to dopants diffusion and silicon mixing, do not prevent electrical conduction.

The largest effect of external contacts non-idealities on the measured behavior of the junction can be found where the characteristics of the overall diode structure comes closest to that of one of its constituent part. We see in Figure 6.18 that this is in the forward regime, where the contribution of the external contact to the p-doped sphere to the overall series resistance is the less negligible. From this analysis we can expect that this global series resistance contains a term that varies by a few $k\Omega$ over the range of voltages of interest.

While the previous demonstration proves that we have discovered a new approach to the fabrication of functional silicon devices, the displayed IV-curve parts from the ideal diode case in ways that we can readily account for. The most obvious non-ideality is the slow-rising current that indicates the presence of a sizable series resistance in the circuit. From our previous considerations, we expect this resistance to be the sum of a constant term (the internal resistance of the junction) and a term that varies of a few $k\Omega$ with voltage, due to the non-ideal external contact to the p-type sphere, these two terms being of comparable importance. However, a series resistance defined this way fails to properly account for the slow rise of current with forward voltage, and cannot account for the second most striking non-ideality of the structure, the growing reverse current with absolute voltage. These trends are the result of a different common phenomenon in p-n structures: the trap-assisted generation and recombination of carriers within the depletion region of the diode. As shown all throughout this study, it is indeed expected that

the interface between the two spheres is populated with a large concentration of crystalline defects that can act as carrier traps. While modelling this effect rigorously is rather involved, we can derive an analytical expression for it that accounts for most of our observations, using a standard derivation based on a few simplifying approximations and the Shockley-Read-Hall model [37]. These consist in noting that the net carrier recombination rate U_{trap} associated with trap-assisted mechanisms is dominated by traps located in the middle of the bandgap, and that within the depletion region of a p-n junction, the product of the carriers' concentrations is set by the applied bias V, following:

$$np = n_i^2 exp\left(\frac{qV}{kT}\right) \tag{6.3.1}$$

where n and p are the concentrations in electrons and holes respectively, n_i the electron concentration in intrinsic silicon at the considered temperature T, with q the charge of an electron and k the Boltzmann constant. U_{trap} can then be written in the simplified form:

$$U_{trap}(n,p) = \frac{n_i^2\left(exp\left(\frac{qV}{kT}\right) - 1\right)}{\tau_{h0}n + \tau_{e0}p + (\tau_{h0} + \tau_{e0})n_i} \tag{6.3.2}$$

where τ_{e0} and τ_{h0} are the electron and hole lifetime, respectively. An approximation of the total current flowing through the junction can then be obtained by integrating the maximum value of U_{trap} over the entire depletion region. This value is obtained when $\tau_{h0}n = \tau_{e0}p$ and yields:

$$I(V) = \frac{CV_{dep}qn_i}{\sqrt{\tau_{h0}\tau_{e0}}}\left(exp\left(\frac{qV}{2kT}\right) - 1\right) \tag{6.3.3}$$

where V_{dep} is the volume of the depleted region inside the junction and C is a dimensionless constant that depends on the interface geometry. This derivation accounts for both effects mentioned above. Indeed, where an ideal diode has a saturation current that does not depend on the bias, here the prefactor in the expression $I(V)$ is proportional to V_{dep}, a depleted volume that grows with the reverse voltage applied to the junction, accounting for the current increase with the negative voltage in Figure 6.18. It also explains the slow forward current rise with V, since it calls for a growth in $exp\left(\frac{qV}{2kT}\right)$ instead of the $exp\left(\frac{qV}{kT}\right)$ expected in a defect-less diode.

6.4 Discussion

Post processing of silicon-in-silica multimaterial fibers [7, 153] using the gradual liquefaction approach enables controlled and scalable production of uniform silicon spheres which can be used on fibers with a wide range of internal core dimensions so as to yield particles from hundreds of nanometers to hundreds of microns. This approach allows to selectively produce spheres that are much smaller than their counterpart obtained under uniform heating, despite the large disparity between core and cladding viscosities. These spheres are shown to be comprised of polycrystalline silicon with low oxygen content and are surrounded by a porous silicon shell. To demonstrate the generality of our approach, a dual-core silicon-in-silica fiber with p- and n-type cores is drawn and processed into spheres. The controlled feeding of the fiber in the heat source induces spatially coherent breakup which leads to the joining of the spheres into a bi-spherical silicon "p-n molecule". The resulting junction is measured to reveal a rectifying I-V curve consistent with the formation of a p-n junction.

6.5 Methods

6.5.1 Preform fabrication and fiber drawing

For a preform preparation we use fused quartz tubes and rods by Technical Glass Products and silicon rods by Lattice Materials. Typical preform assembly scheme is shown in Figure 6.19. First, a silicon rod with the diameter of 2 mm is sleeved into a preform with the silica cladding of 8mm and drawn at 2,130 ^oC with $v_f = 1.2\ mm.min^{-1}$ and $v_d = 0.3\ mm.min^{-1}$. This yields a silicon-core fiber with the core diameter of 130 μm and the outer diameter of 500 μm. It is then fed into a new preform having silica cladding diameter of 12mm and redrawn at 2,095 ^oC and $v_f = 1.2\ mm.min^{-1}$, $v_d = 2\ mm.min^{-1}$ in order to reduce the silicon-core thickness to 4 μm. A typical preform assembly scheme for fiber redraw is shown in Figure 6.19.

At the redraw stage, in order to avoid the break-up of the core material inside the preform before its descent into the fiber, the preform should be fed as fast as possible and drawn as fast as possible, thus shortening the dwell time of silicon in the hot zone of the furnace. The fact that only 100–200 μm in the center of the active part of the preform contain material different

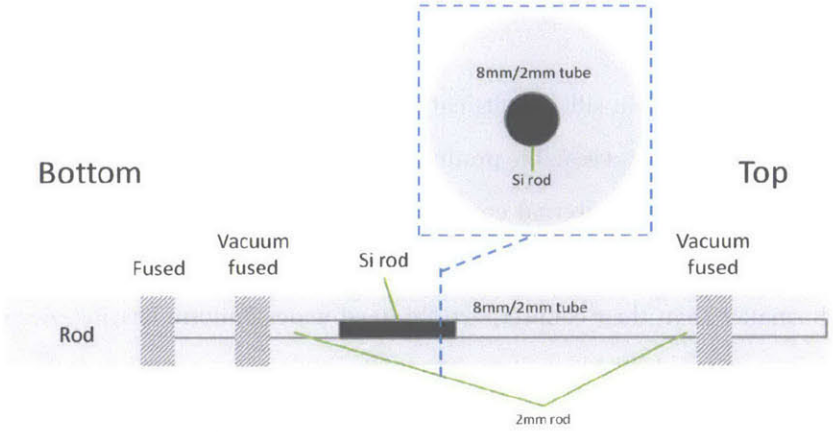

Figure 6.19: Typical assembly scheme for fabrication of silicon core preform. **1.** – 60 cm long 8 mm / 2 mm, and 15 cm section of 2 mm rod are sleeved and fused with a thick rod to seal the bottom. **2.** – 10 cm long silicon rod is inserted into the pocket. The bottom is vacuum fused to ensure hermetic closure. **3.** – 35 cm long 2 mm rod is inserted to close the pocket and the structure is vacuum fused on the top.

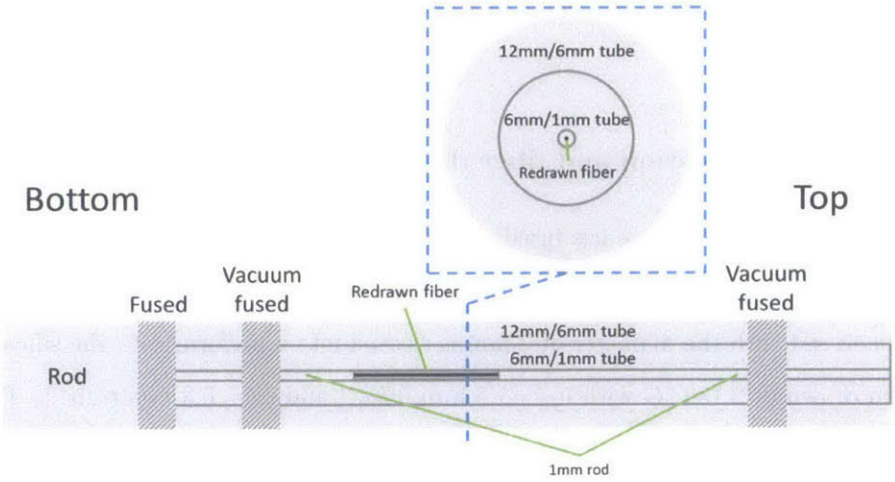

Figure 6.20: Typical assembly scheme for fabrication of preform for fiber redraw. **1.** – 60 cm long 12 mm / 6 mm, 6mm / 1mm tubes and 15 cm section of 1mm rod are sleeved and fused with a thick rod to seal the bottom. **2.** – 12 cm long fiber section is inserted into the pocket. The bottom is vacuum fused to ensure hermetic closure. **3.** – 33 cm long 1mm rod is inserted to close the pocket and the structure is vacuum fused on the top.

than silica, allows doing so, while still maintaining a crack-free draw. The feed speed and the draw speed are $v_f = 1.2\ mm.min^{-1}$, $v_d = 2\ mm.min^{-1}$, respectively. The fiber is drawn at lowest possible temperature providing crackless draw (2,095 ^oC), that is, at the highest possible tension. The fiber is protected by an in-line ultraviolet curable coating system. The coating layer is 'DSM Desotech 3471-3-14(941–314) Desolite single coat coating' with a thickness of 20–40 μm.

The redraw of the fiber with a 130-μm silicon-core in the conditions described above resulted in 60-m-long continuous section of silicon-core fiber, starting from a thin core in the beginning (thinnest sampled was 0.5 μm thick) growing in a few metres and stabilizing at (4 $\pm$ 5 %) μm. This is roughly the thinnest stably drawable and controllably scalable core size, while using conventional draw process. The redraw of the fibers with ~100 μm silicon-core at the conditions described above resulted in continuous-core sections of tens of metres with core sizes of (1.7 $\pm$ 50 %) μm, and the redraw of the fibers with ~70 mm silicon-core has failed to give significantly long sections of fiber with continuous core; these fibers were mostly blank, indicating that the break-up of the core occurred in the preform. Scaling of the fiber core to the nano-metric regime is thus challenging to achieve using conventional fiber-draw techniques [154, 155].

Conventional techniques are characterized by a ratio of preform feed speed v_f to fiber drawing speed v_d ranging from two to four orders of magnitude resulting in a typical preform to fiber cross-sectional scaling ratios of few tens to few hundreds. When producing silica fibers, such a $\frac{v_f}{v_d}$ ratio requires the draw to be performed at relatively low viscosity of silica in order to avoid cracking of the fiber during the draw due to the viscous rupture phenomenon [156]. On the other hand, practical range of scaling ratios limits the core in the preform to diameters that are large enough to prevent the silicon break-up to occur in the drawing cone before descending into the fiber, the more so that the high interfacial tension γ between the core and the cladding [157] speeds up the break-up process. The last would result in a fiber with uneven silicon-core of random diameter. Faster feed speed would compensate over this break-up partially, by shortening the dwell time of silicon in the drawing cone, where it is sensitive to the capillary instabilities. Unfortunately, this would result in a decreased cross-section scaling ratio, providing a thicker fiber core. To maintain the core thickness unchanged, the draw speed in that case should be increased, which would require an additional decrease in silica viscosity for crack-free fibers.

6.5.2 Torch scaling

During the first scaling process the fiber is placed in the hot spot of the flame resulting from the burning of hydrogen flowing at the rate of 0.23 $l.min^{-1}$ through the aperture of the torch outlet having a small diameter of 0.020". Such a small diameter of the outlet aperture is picked in order to focus the flame and to prevent flashback explosion at such a law gas flow. The 4 μm silicon-core fiber was rescaled through the flame 3 times. At each re-scaling iteration, the hydrogen flow is reduced by 0.02 $l.min^{-1}$ in order to compensate over the decrease in a heat capacity of the scaled fiber, so that high tension can be maintained.

6.5.3 Details on the dimensional analysis of gradual-heating break-up

As shown in Figure 6.7, when break-up is induced under gradual-heating conditions, the final sphere size can be seen as the result from the competition between the feed speed v_f and the velocity up of the silicon/silica interface at the location xp where the core periodically pinches-off. We give here more details on how the expression of u_p given in Section 6.3.1 is obtained.

We can approach the question of the velocity of the interface through dimensional analysis and scaling of the governing fluid mechanics equations. Fluid flow in the system is predominantly forced by interfacial tension; therefore, the relevant boundary condition to focus on is the normal stress balance at the silicon/silica interface, which writes:

$$n \cdot T^{SiO_2} \cdot n - n \cdot T^{Si} \cdot n = \gamma \left(\nabla \cdot n \right) \tag{6.5.1}$$

where T^{SiO_2} and T^{Si} are the stress tensors in silica and silicon, respectively, and γ is the silicon/silica interfacial tension. The components of the stress tensor in silicon are:

$$T_{ij}^{Si} = -p^{Si}\delta_{ij} + \mu^{Si}\left(\frac{\partial v_i}{\partial x_j} + \frac{\partial v_j}{\partial x_i}\right) \tag{6.5.2}$$

where v_i are the components of the velocity field in silicon, and p^{Si} is the pressure field in silicon. A similar expression holds for silica.

Assuming low-Reynolds number flows in both silicon and silica, and noting that the characteristic length scale in the problem is the silicon-core diameter D, we conclude that the charac-

teristic pressures at the pinch-off location are $p^{Si} \sim \left(2\mu_p^{Si}/D\right) \cdot u_p$ and $p^{SiO_2} \sim \left(2\mu_p^{SiO_2}/D\right) \cdot u_p$, respectively, in silicon and silica. At that point, the stress balance condition can be rewritten:

$$\left(\mu_p^{SiO_2} - \mu_p^{Si}\right) \frac{u_p}{D} \sim \frac{\gamma_p}{D} \tag{6.5.3}$$

As shown in Figure 6.3, under all practical temperatures, $\mu_p^{SiO_2} \gg \mu_p^{Si}$, which allows us to simplify the previous equation and obtain the expression for u_p used in section 6.3.1:

$$u_p \sim \frac{\gamma_p}{\mu_p^{SiO_2}} \tag{6.5.4}$$

From this approach, we can compute Reynolds numbers for silicon and silica: $Re^{Si} = (\rho^{Si} a/\mu^{Si}) \cdot (\gamma/\mu^{SiO_2})$ and $Re^{SiO_2} = (\rho^{Si} a/\mu^{SiO_2}) \cdot (\gamma/\mu^{SiO_2})$. For any practical pair (D,T) considered, these Reynolds numbers are both always orders of magnitude below unity, which validates the approximation of Stokes flow regime leading to the scaling of characteristic pressure in the fluids made above.

6.5.4 TEM sample preparation and TEM measurements details

Investigation of the sphere structure included the inspection of the bare spheres directly released on the Cu-frame carbon membrane TEM grid. To prepare the sample the fiber section is immobilized on CF300-CU CARBON FILM on 300 Cu mesh copper grid by Electron Microscopy Sciences (3mm in diameter), then immersed in HF. It allowed an observation of core-shell structure comprising the sphere shown in Figure 6.13.

6.5.5 Bispherical p–n junction fabrication

First, a preform containing two separated silicon rods was prepared and drawn into a double-core fiber. One p-type silicon rod (electron acceptors concentration $N_A = 6.9\text{x}10^{18} cm^{-3}$) and one n-type silicon rod (electron donors concentration $N_D = 1.6\text{x}10^{19} cm^{-3}$) with 2mm diameter were sleeved into a preform with a silica cladding of 12 mm, and drawn at 2,130 ^oC with feed speed $v_f = 0.6\ mm.min^{-1}$ and draw speed $v_d = 0.6\ m.min^{-1}$.

Then a section of the resulting fiber was incorporated into a new preform in a similar fashion as described in Figure 6.20. The preform was then drawn with the feed speed $v_f = 1.2\ mm.min^{-1}$ and the draw speed $v_d = 1.2\ mm.min^{-1}$ at the draw temperature of 2,085 ^oC. The resulting fiber cross-section is shown in Figure 6.21. The cross-sectional geometry is maintained exactly as in the preform. The core separation is preserved, and both cores have the same diameter of 23 μm.

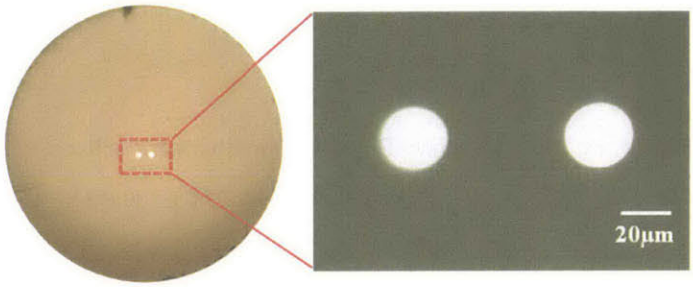

Figure 6.21: Optical microscope images of a dual-core fiber, one core is p-type silicon, and the other core is n-type silicon.

A section of a dual-core fiber underwent the gradual-heating break-up at a feed speed $v_f = 20\ \mu m.s^{-1}$ using a flame resulting from gas flows of hydrogen and oxygen of 0.42 $l.min^{-1}$ and 0.20 $l.min^{-1}$, respectively, resulting in a chain of in-fiber bispherical p–n junctions in a similar manner as shown in Figure 6.15. The bispherical p–n junctions were released from the fiber by dissolving silica cladding in HF acid as appear in Figure 6.16.

6.5.6 Current-voltage characteristics measurement of the p–n junction

After a two-sphere particle is released out of the fiber cladding using HF acid, two tungsten needles (2.4 μm, Cascade Microtech, PTT-24-25) are brought in contact with the spheres' surface using manual probe positioners (Cascade Microtech). Voltage is applied between the probes by a Keithley 6517A Electrometer while current is measured by a Keithley 6487 Picoammeter, both units controlled via a LABVIEW custom interface.

Chapter 7

Suggested future work and conclusions

7.1 Selective break-up for in-fiber photosensing pixels

While the demonstration of the contact-by-breakup principle in section 6.3.3 is groundbreaking, the devices formed this way are not readily usable. Ideally, discrete devices in fibers should be addressable electrically so as to be functional within the fiber, with no etching or post-processing needed. Not only the path from fabrication to utilization would be much simplified, but such a new structure would bring a radically new concept for functional fibers: the embedding of discrete, addressable micro-devices evenly spaced along unlimited fiber lengths. In Figure 7.1, we illustrate how such a structure could be fabricated, building on the knowledge presented in chapter 6.

In this example, discrete - but electrically addressable - photosensing structures would be formed in a 2-step operation:

- First, a preform containing a central semiconducting core flanked by two metal cores, isolated by a suitably thick silica membrane would be drawn into a fiber.

- Second, the fiber would be towed through a flame at a carefully selected temperature and speed, so as to induce the breakup of the central semiconducting core into spheres just large enough to come into contact with the still-solid metal conducts.

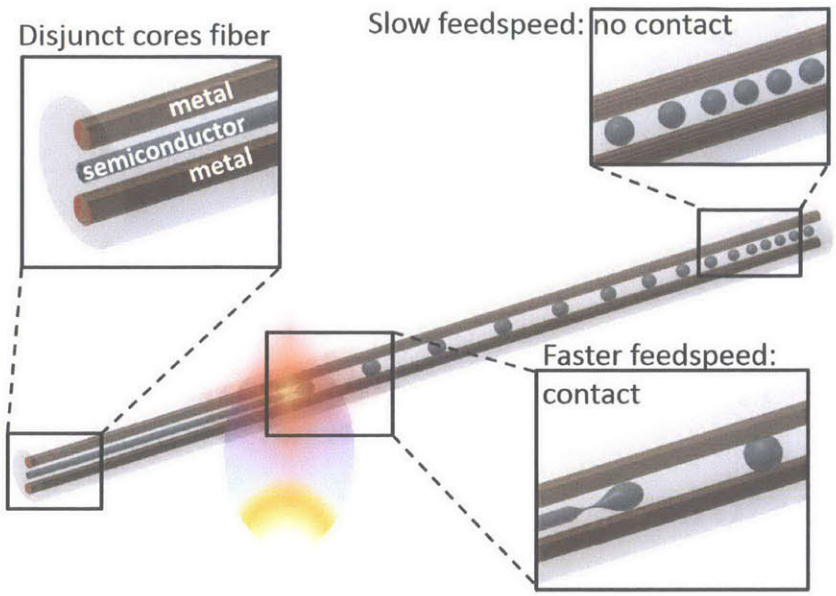

Figure 7.1: Concept for the fabrication of discrete photosensing devices addressed by continuous metal conducts: starting from a silica fiberr with a central core of semiconductor (such as Ge or Si) surrounded by two metal filaments, we propose to find the proper parameters to induce breakup selectively in the central element. From an initial feed speed for which the resulting spheres are smaller than the space between the metal buses, we propose to increase the feed speed until the formed spheres reach the exact dimension of the gap and establish contact with both metal filaments.

Provided these two steps were successfully executed, the end result should be a line of discrete semiconducting spheres, evenly spaced, electrically connected to two metal conduct, with the overall structure embedded in silica over arbitrary lengths. In principle, this approach is simple enough to be very promising. However, there are constraints on the selection of the materials that arise from the relatively extreme treatment that they are subject to, from the preform to the final pixelized fiber. The constraints are of various types:

- First, all materials embedded in silica must be drawable at around $2,150^{o}C$ without chemically reacting with the silica, degrading, transforming or changing phase. It is assumed that the preform-to-fiber step is more extreme from the chemical reactivity standpoint that the subsequent flame treatment, and that elements should not react within the flame if they have not reacted in the drawing furnace.

- Second, the thermal expansion or contraction of all the materials involved must be compatible, in the sense that the fiber must remain intact through the various heating and cooling steps it is subject to throughout the process. While a number of materials can be co-drawn with silica under the right conditions, the implementation of 3 or more materials within a single fiber complicates the picture. Besides, it has been observed than embedded non-spherical structure (such as the p-n particle of section 6.3.3) can induce crack or even shattering of the surrounding silica upon cooling after their formation. It is possible that the spheres-in-contact-with-wires geometry would also induce such fragility in the resulting fiber.

- Third, the metal(s) used in for the buses must have a melting temperature sitting between the flame temperature and the drawing temperature. The flame-temperature is not fully known but it can be estimated to be at least $1,700^oC$ when inducing breakups. Therefore, the metal(s) melting temperature(s) must be in the $1,700^oC$ to $2,100^oC$ range, which considerably limits the choice.

- Fourth, the electrical behavior of the metal-semiconductor contacts must be consistent, and at least one of the two has to be ohmic for the devices to be functional. If the two contacts on the sphere sides are ohmic, the semiconductor can act as a photoconductor. If only one is ohmic, the other rectifying (for instance by using two different metals), a photodiode could be formed.

This set of constraints makes this simple approach actually challenging and to date, no metal has been identified as a suitable candidate. However, there are a number of options unexplored yet, such as the drawing of platinum, or metal alloys.

Finally, it is important to note that the concept illustrated in Figure 7.1 is only an example, that would act as a great proof-of-concept. This approach is not limited to a single core of semiconductor, and more cores could be placed between the metal conduct. An isothermal breakup approach could also be pursued if the proper parameters were identified.

7.2 Diffusion-enabled in-silica copper contacts

It has been repeatedly witnessed that, during high-temperature, low-viscosity fiber drawing, thin portions of silica between the preform domains could be further thinned-down, to the point where they would sometimes fully retract. This interesting phenomenon, combined with the high diffusivity of copper in silica [158] lead us to examine the possibility of establishing acceptable electrical conduction between two domains that remain separated by a thinned-down silica membrane. Preliminary measurements of conduction through an in-fiber thin membrane of silica have shown that the conductivity of the silica was enhanced by annealing the fiber.

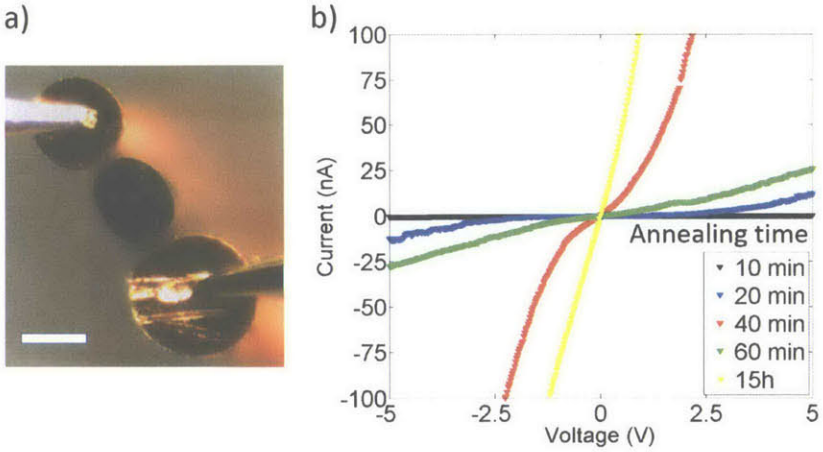

Figure 7.2: a) Optical micrograph of the central part of the cross-section of a silica fiber containing a central silicon core flanked by two copper domains, each contacted by tungsten microprobes and physically separated from the silicon core by silica. Scale bar is 50 μm. b) IV curves for 6 different adjacent portions of the fiber described in a) with electrical probes placed on the copper elements. The 6 samples have been annealed after the draw at a temperature of 900°C for the time indicated in the legend.

Adjacent portions of a silica fiber containing a silicon core flanked by two copper domains separated from the core by thin silica membranes have been annealed post-draw at 900°C for various durations, and the resulting IV measurements from one copper element to the other are displayed in Figure 7.2. Annealing is thought to be responsible for the sharp increase in conductivity of the samples that have been annealed for the longest time, over that of other

samples. In future work, this phenomenon should be further investigated. First, in order to specifically characterize the conduction through silica and how it is impacted by the diffusion of copper, fibers with only two elements of copper should be tested. Indeed, the conduction from copper-doped silica to an in-fiber silicon element is likely to have its own non-trivial electrical behavior and therefore it is preferable to start with a simpler system. Besides, it is preferable to study the impact of annealing on a sample tested as drawn and after various annealing times, instead of testing adjacent fiber samples, that my not be strictly identical.

The results displayed in Figure 7.2 are very encouraging, and future work will tell whether this approach can become a reliable way to ensure electrical conduction across adjacent domains in a silica fiber, while keeping these domains separated and unmixed.

7.3 Composite dielectric for ultracapacitive fibers

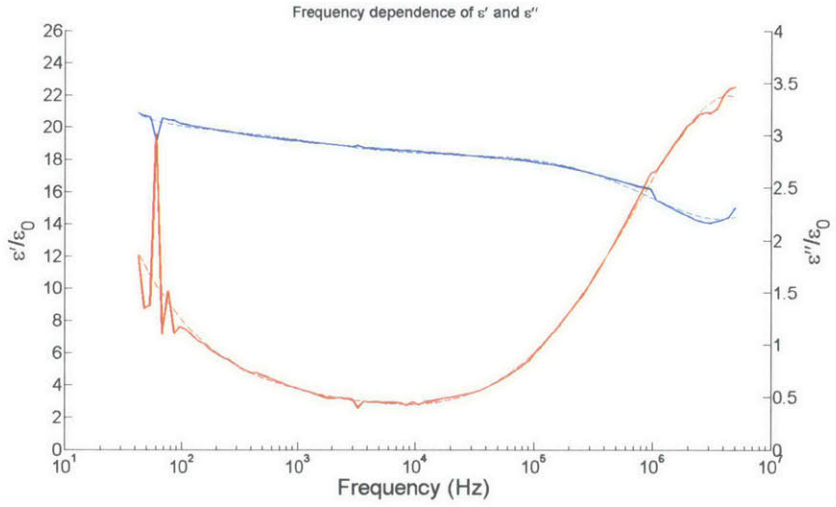

Figure 7.3: Frequency dependence of $\epsilon_{pvdf-Ni}$ of a $390\mu m$-thick film before thermal draw. The solid blue line represents the measured real part (left axis), the solid red line the measured imaginary part (right axis). Dashed blue and red lines are 4^{th} order polynomial approximations of these data.

As mentioned in section 5.5.1, nanocomposite materials using PVDF or its co- or ter-polymers as matrix, filled with various ceramic, metallic or organic particles are the center of an active area of research [109], and dielectric constants in the hundreds have already been achieved [118, 119, 120]. While no demonstration of a PVDF-composite-based fiber capacitor has been done, some promising results have been obtained and are worth pursuing in the future. Indeed, with the proper protocol - either by mixing and pressing powder, or by dissolving PVDF and mixing it with the proper particles, films of PVDF-composites can readily be fabricated, with various concentrations of different fillers.

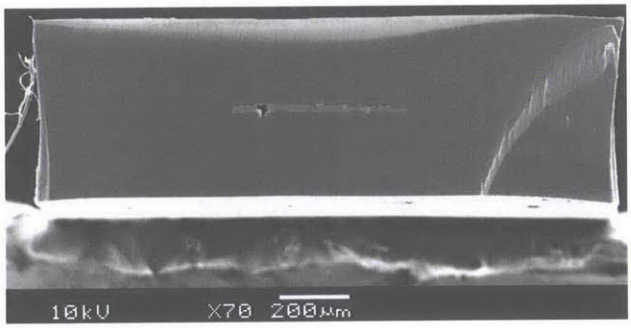

Figure 7.4: SEM micrograph of a PSU-clad thermally-drawn Ni-filled PVDF film. The central layer is not fully uniform but its thin-film shape proves that the materials can be co-drawn under the right conditions.

In Figure 7.3 we show the freqency response of both real and imaginary parts of the dielectric permittivity of a 390-μm thin film of Ni-loaded PVDF (15 % volume) obtained by mixing and pressing powders at 200^oC and 100 bars. While the mimimum dielectric losses are higher than that of pure PVDF (as shown in Figure 5.5), the permittivity of this composite is twice as high, which illustrates the potential of composite materials to greatly increase the capacitance of fibers. The Ni-loaded PVDF, unlike other ceramic-filled polymers (like $BaTiO_3$-filled PVDF) proved thermally-drawable within a PolySulfone preform at about 300^oC. The resulting fiber was far from perfect but the materials did flow together, as the SEM view in Figure 7.4 allows to judge.

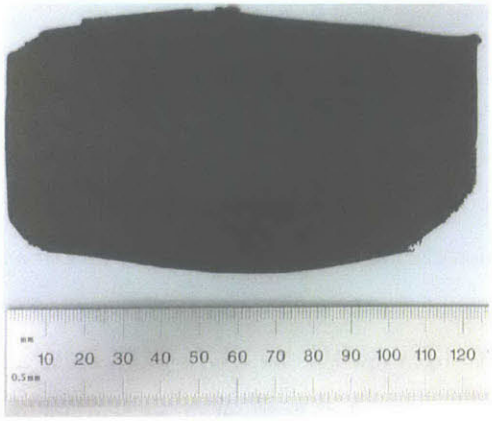

Figure 7.5: Optical micrograph of the Ni-loaded PVDF film obtained by mixing PVDF and Ni powders and later pressing the mix. To the naked eye, the resulting polymer looks uniform, and also displays good flexibility, comparable to that of a pure PVDF film.

However, while the pressed composite looks uniform to the eye (see Figure 7.5), nickel aggregates are visible on the close-up view in Figure 7.6, which indicates that the powder mixing might not be the most appropriate technique to obtain homogeneous concentrations of fillers in PVDF. Dissolving the PVDF in a solvent and then incorporating and sonicating the powder filler seems like a better approach but only very preliminary tests were carried in that direction, which should be explored in future work.

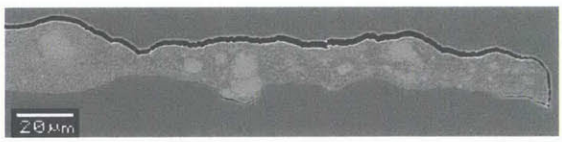

Figure 7.6: Close-up view of the SEM micrograph shown in Figure 7.4. At this magnification, nickel aggregates are clearly visible, indicating that the powder mixing did not ensure a perfect spread of the nickel-filler within the PVDF.

7.4 Conclusions

Throughout this thesis, we have demonstrated multiple new designs, integration schemes, structures and processes that push the boundaries of what can be achieved with electronic multimaterial fibers. We have demonstrated that the axial uniformity of these fibers was not preventing the sensing or modulation of signals along their length and that their flexibility and easy assembly into arrays could enable 3-dimensional signal-shaping (and conversely, sensing) in a very simple fashion. We have opened the way towards energy-storage in thermally-drawn fibers, a path that is the object of a lot of attention at the moment of writing of this thesis, and that could address the increasing demand of energy on the go as the use of mobile devices soars. Finally, implementing a novel process that leverages capillary instabilities in fiber systems with large viscosity contrasts between materials, we have demonstrated a path towards the fabrication of silicon microelectronic devices in silica-fibers. As we have shown, this discovery is likely the most significant of this entire thesis work, as it paves the way towards fully-integrated, electrically-addressable discrete silicon devices in arbitrarily-long silica fibers.

Bibliography

[1] B. Temelkuran, S.D. Hart, G. Benoit, J.D. Joannopoulos, and Y. Fink. Wavelength-scalable hollow optical fibres with large photonic bandgaps for CO2 laser transmission. *Nature*, 420(6916):650–3, December 2002.

[2] S.D. Hart, G.R. Maskaly, B. Temelkuran, P.H. Prideaux, J.D. Joannopoulos, and Y. Fink. External reflection from omnidirectional dielectric mirror fibers. *Science*, 296(5567):510–3, April 2002.

[3] M. Bayindir, F. Sorin, A.F. Abouraddy, J. Viens, S.D. Hart, J.D. Joannopoulos, and Y. Fink. Metal–insulator–semiconductor optoelectronic fibres. *Nature*, 431(7010):826–829, 2004.

[4] M. Bayindir, O. Shapira, D. Saygin-Hinczewski, J. Viens, A.F. Abouraddy, J.D. Joannopoulos, and Y. Fink. Integrated fibres for self-monitored optical transport. *Nature Materials*, 4(11):820–825, 2005.

[5] M. Bayindir, A.E. Abouraddy, J. Arnold, J.D. Joannopoulos, and Y. Fink. Thermal-sensing fiber devices by multimaterial codrawing. *Advanced Materials*, 18(7):845–+, 2006.

[6] O. Shapira, K. Kuriki, N.D. Orf, A.F. Abouraddy, G. Benoit, J.F. Viens, A. Rodriguez, M. Ibanescu, J.D. Joannopoulos, Y. Fink, and M.M. Brewster. Surface-emitting fiber lasers. *Optics Express*, 14(9):3929–35, May 2006.

[7] A.F. Abouraddy, M. Bayindir, G. Benoit, S.D. Hart, K. Kuriki, N. Orf, O. Shapira, F. Sorin, B. Temelkuran, and Y. Fink. Towards multimaterial multifunctional fibres that see, hear, sense and communicate. *Nature Materials*, 6(5):336–347, 2007.

[8] F. Sorin, O. Shapira, A.F. Abouraddy, M. Spencer, N.D. Orf, J.D. Joannopoulos, and Y. Fink. Exploiting collective effects of multiple optoelectronic devices integrated in a single fiber. *Nano Letters*, 9(7):2630–2635, 2009.

[9] S. Egusa, Z. Wang, N. Chocat, Z. M. Ruff, A. M. Stolyarov, D. Shemuly, F. Sorin, P.T. Rakich, J.D. Joannopoulos, and Y. Fink. Multimaterial piezoelectric fibres. *Nature Materials*, 9(8):643–648, 2010.

[10] S. Danto, F. Sorin, N.D. Orf, Z. Wang, S.A. Speakman, J.D. Joannopoulos, and Y. Fink. Fiber field-effect device via in situ channel crystallization. *Advanced Materials*, 22(37):4162–+, 2010.

[11] D.S. Deng, N.D. Orf, A.F. Abouraddy, A.M. Stolyarov, J.D. Joannopoulos, H.A. Stone, and Y. Fink. In-fiber semiconductor filament arrays. *Nano Letters*, 8(12):4265–4269, 2008.

[12] J.J. Kaufman, G. Tao, S. Shabahang, E.-H. Banaei, D.S. Deng, X. Liang, S.G. Johnson, Y. Fink, and A.F. Abouraddy. Structured spheres generated by an in-fibre fluid instability. *Nature*, pages 1–5, July 2012.

[13] N. Orf, O. Shapira, F. Sorin, S. Danto, M.A., J.D. Joannopoulos, and Y. Fink. Fiber draw synthesis. *Proceedings of the National Academy of Sciences*, 108(12):4743–7, 2011.

[14] C. Hou, X. Jia, L. Wei, A.M. Stolyarov, O. Shapira, J.D. Joannopoulos, and Y. Fink. Direct atomic-level observation and chemical analysis of ZnSe synthesized by in situ high-throughput reactive fiber drawing. *Nano letters*, 13(3):975–9, March 2013.

[15] F. Yu and S Yin. *Fiber Optic Sensors*. 2008.

[16] K.T.V. Grattan and B.T. Meggitt. *Optical Fiber Sensor Technology, Fundamentals*. 2000.

[17] A. Rogers. Distributed optical-fibre sensing. *Measurement Science and Technology*, 10:R75–99, 1999.

[18] A. Othonos and K. Kalli. *Fiber Bragg Gratings - Fundamentals and Applications in Telecommunications and Sensing*. 1999.

[19] M.K. Barnoski and S.M. Jensen. Fiber waveguides: a novel technique for investigating attenuation characteristics. *Applied Optics*, 15(9):2112–5, September 1976.

[20] A.J. Rogers. Polarization-optical time domain reflectometry: a technique for the measurement of field distributions. *Applied Optics*, 20(6):1060–74, March 1981.

[21] A.H. Hartog. A distributed temperature sensor based on liquid-core optical fibers. *Lightwave Technology, Journal of*, 1983.

[22] J.P. Dakin, D.J. Pratt, G.W. Bibby, and J.N. Ross. Distributed optical fibre Raman temperature sensor using a semiconductor light source and detector. *Electronics Letters*, 21(13):569–570, 1985.

[23] T. Kurashima, T. Horiguchi, and M. Tateda. Distributed-temperature sensing using stimulated Brillouin scattering in optical silica fibers. *Optics Letters*, 15(18):1038–40, September 1990.

[24] C.I. Merzbacher, A.D. Kersey, and E.J. Friebele. Fiber optic sensors in concrete structures: a review. *Smart materials and structures*, 5:196, 1996.

[25] X. Bao, D.J. Webb, and D.A. Jackson. Combined distributed temperature and strain sensor based on Brillouin loss in an optical fiber. *Optics Letters*, 19(2):141, January 1994.

[26] P. J. A. Sazio, A. Amezcua-Correa, C. E. Finlayson, J. R. Hayes, T. J. Scheidemantel, N. F. Baril, B. R. Jackson, D. J. Won, F. Zhang, E. R. Margine, V. Gopalan, V. H. Crespi, and J. V. Badding. Microstructured optical fibers as high-pressure microfluidic reactors. *Science*, 311(5767):1583–1586, 2006.

[27] T.T. Larsen, A. Bjarklev, D.S. Hermann, and J. Broeng. Optical devices based on liquid crystal photonic bandgap fibres. *Optics Express*, 11(20):2589–2596, 2003.

[28] B. O'Connor, K.H. An, Y. Zhao, K.P. Pipe, and M. Shtein. Fiber shaped organic light emitting device. *Advanced Materials*, 19(22):3897–+.

[29] B. O'Connor, K.P. Pipe, and M. Shtein. Fiber based organic photovoltaic devices. *Applied Physics Letters*, 92(19), 2008.

[30] M. Fokine, L. E. Nilsson, A. Claesson, D. Berlemont, L. Kjellberg, L. Krummenacher, and W. Margulis. Integrated fiber mach-zehnder interferometer for electro-optic switching. *Optics Letters*, 27(18):1643–1645, 2002.

[31] M.A. Schmidt, L.N. Prill Sempere, H.K. Tyagi, C.G. Poulton, and P.St J. Russell. Waveguiding and plasmon resonances in two-dimensional photonic lattices of gold and silver nanowires. *Physical Review B*, 77(3), 2008.

[32] H.K. Tyagi, M.A. Schmidt, L.N. Prill Sempere, and P.St J. Russell. Optical properties of photonic crystal fiber with integral micron-sized ge wire. *Optics Express*, 16(22):17227–17236, 2008.

[33] M. Bayindir, A.F. Abouraddy, O. Shapira, J. Viens, D. Saygin-Hinczewski, F. Sorin, J. Arnold, J.D. Joannopoulos, and Y. Fink. Kilometer-long ordered nanophotonic devices by preform-to-fiber fabrication. *Ieee Journal of Selected Topics in Quantum Electronics*, 12(6):1202–1213, 2006.

[34] F. Sorin, A.F. Abouraddy, N. Orf, O. Shapira, J. Viens, J. Arnold, J.D. Joannopoulos, and Y. Fink. Multimaterial photodetecting fibers: a geometric and structural study. *Advanced Materials*, 19(22):3872–+, 2007.

[35] A.F. Abouraddy, O. Shapira, M. Bayindir, J. Arnold, F. Sorin, D.S. Hinczewski, J.D. Joannopoulos, and Y. Fink. Large-scale optical-field measurements with geometric fibre constructs. *Nature Materials*, 5(7):532–536, 2006.

[36] E. Rosencher and B. Vinter. *Optoelectronics*. 2002.

[37] S.M. Sze. *Semiconductor Devices: Physics and Technology*. 2001.

[38] R.H. Kingston. *Detection of Optical and Infrared Radiation*. 1978.

[39] E. K. Sichel, J. I. Gittleman, and P. Sheng. Electrical properties of carbon - polymer composites. *Journal of Electronic Materials*, 11(4):699–747, 1982.

[40] Z.U. Borisova. *Glassy Semiconductors*. 1981.

[41] H. Kawamoto. The history of liquid-crystal displays. *Proceedings of the Ieee*, 90(4):460 500, 2002.

[42] R. Ozaki, T. Matsui, M. Ozaki, and K. Yoshino. Electrically color-tunable defect mode lasing in one-dimensional photonic-band-gap system containing liquid crystal. *Applied Physics Letters*, 82(21):3593–3595, 2003.

[43] B. Maune, M. Loncar, J. Witzens, M. Hochberg, T. Baehr-Jones, D. Psaltis, A. Scherer, and Y. M. Qiu. Liquid-crystal electric tuning of a photonic crystal laser. *Applied Physics Letters*, 85(3):360–362, 2004.

[44] G. Strangi, V. Barna, R. Caputo, A. De Luca, C. Versace, N. Scaramuzza, C. Umeton, R. Bartolino, and G. N. Price. Color-tunable organic microcavity laser array using distributed feedback. *Physical Review Letters*, 94(6), 2005.

[45] A.M. Stolyarov, L. Wei, O. Shapira, F. Sorin, S.L. Chua, J.D. Joannopoulos, and Y. Fink. Microfluidic directional emission control of an azimuthally polarized radial fibre laser. *Nature Photonics*, (March):1–5, 2012.

[46] G.D. Love. Wave-front correction and production of zernike modes with a liquid-crystal spatial light modulator. *Applied Optics*, 36(7):1517–1524, 1997.

[47] N. Konforti, E. Marom, and S. T. Wu. Phase-only modulation with twisted nematic liquid-crystal spatial light modulators. *Optics Letters*, 13(3):251–253, 1988.

[48] J.S. Patel, M.A. Saifi, D.W. Berreman, C.L. Lin, N. Andreadakis, and S.D. Lee. Electrically tunable optical filter for infrared wavelength using liquid-crystals in a fabry-perot etalon. *Applied Physics Letters*, 57(17):1718–1720, 1990.

[49] H. Meyer, W. Thust, E. Schroder, K.P. Schmidt, U.J. Schmidt, D. Riekmann, and M. Rahlff. Design and performance of a 20-stage digital light-beam deflector. *Applied Optics*, 11(8):1732, 1972.

[50] S. Sato. Liquid-crystal lens-cells with variable focal length. *Japanese Journal of Applied Physics*, 18(9):1679–1684, 1979.

[51] A. Fratalocchi, G. Assanto, K. A. Brzdakiewicz, and M. A. Karpierz. Discrete propagation and spatial solitons in nematic liquid crystals. *Optics Letters*, 29(13):1530–1532, 2004.

[52] M. Humar, M. Ravnik, S. Pajk, and I. Musevic. Electrically tunable liquid crystal optical microresonators. *Nature Photonics*, 3(10):595–600, 2009.

[53] M. Ohe and K. Kondo. Electro-optical characteristics and switching behavior of the in-plane switching mode. *Applied Physics Letters*, 67(26):3895–3897, 1995.

[54] T. T. Alkeskjold, J. Laegsgaard, A. Bjarklev, D. S. Hermann, Anawati, J. Broeng, J. Li, and S. T. Wu. All-optical modulation in dye-doped nematic liquid crystal photonic bandgap fibers. *Optics Express*, 12(24):5857–5871, 2004. Wu, Shin-Tson/K-7886-2013.

[55] F. Du, Y.Q. Lu, and S.T. Wu. Electrically tunable liquid-crystal photonic crystal fiber. *Applied Physics Letters*, 85(12):2181–2183, 2004.

[56] M. W. Haakestad, T. T. Alkeskjold, M. D. Nielsen, L. Scolari, J. Riishede, H. E. Engan, and A. Bjarklev. Electrically tunable photonic bandgap guidance in a liquid-crystal-filled photonic crystal fiber. *Ieee Photonics Technology Letters*, 17(4):819–821, 2005.

[57] T.T. Alkeskjold, L. Scolari, D. Noordegraaf, J. Laegsgaard, J. Weirich, L. Wei, G. Tartarini, P. Bassi, S. Gauza, S.-T. Wu, and A. Bjarklev. Integrating liquid crystal based optical devices in photonic crystal fibers. *Optical and Quantum Electronics*, 39(12-13):1009–1019, 2007.

[58] P. Yeh and C. Gu. *Optics of Liquid Crystal Displays*. 2010.

[59] F. Sorin, G. Lestoquoy, S. Danto, J.D. Joannopoulos, and Y. Fink. Resolving optical illumination distributions along an axially symmetric photodetecting fiber. *Optics express*, 18(23):24264–24275, November 2010.

[60] N. Chocat, G. Lestoquoy, Z. Wang, D.M. Rodgers, J.D. Joannopoulos, and Y. Fink. Piezoelectric fibers for conformal acoustics. *Advanced materials*, pages 5327–5332, July 2012.

[61] O.S. Wolfbels. Fiber-optic chemical sensors and biosensors. *Analytical Chemistry*, 80(12):4269–4283, 2008.

[62] T.M. Monro, W. Belardi, K. Furusawa, J.C. Baggett, N.G. R. Broderick, and D.J. Richardson. Sensing with microstructured optical fibres. *Measurement Science and Technology*, 12(7):854–858, 2001.

[63] S.O. Konorov, A.M. Zheltikov, and M. Scalora. Photonic-crystal fiber as a multifunctional optical sensor and sample collector. *Optics Express*, 13(9):3454–3459, 2005.

[64] H. Tai, H. Tanaka, and T. Yoshino. Fiberoptic evanescent-wave methane-gas sensor using optical-absorption for the 3.392 μm line of a he-ne laser. *Optics Letters*, 12(6):437–439, 1987.

[65] K. Chan, H. Ito, and H. Inaba. Remote-sensing system for near-infrared differential absorption of ch_4 gas using low-loss optical fiber link. *Applied Optics*, 23(19):3415–3420, 1984.

[66] G. Stewart, W. Jin, and B. Culshaw. Prospects for fibre-optic evanescent-field gas sensors using absorption in the near-infrared. *Sensors and Actuators B: Chemical*, 38(1-3):42–47, 1997.

[67] J. Heo, M. Rodrigues, S.J. Saggese, and G.H. Sigel. Remote fiberoptic chemical sensing using evanescent-wave interactions in chalcogenide glass-fibers. *Applied Optics*, 30(27):3944–3951, 1991.

[68] Y.L. Hoo, W. Jin, H.L. Ho, D.N. Wang, and R.S. Windeler. Evanescent-wave gas sensing using microstructure fiber. *Optical Engineering*, 41(1):8–9, 2002.

[69] J. A. Harrington. A review of ir transmitting, hollow waveguides. *Fiber and Integrated Optics*, 19(3):211–227, 2000.

[70] T.M. Monro, D.J. Richardson, and P.J. Bennett. Developing holey fibres for evanescent field devices. *Electronics Letters*, 35(14):1188–1189, 1999.

[71] T. Ritari, J. Tuominen, H. Ludvigsen, J.C. Petersen, T. Sorensen, T.P. Hansen, and H.R. Simonsen. Gas sensing using air-guiding photonic bandgap fibers. *Optics Express*, 12(17):4080–4087, 2004.

[72] A. Yildirim, M. Vural, M. Yaman, and M. Bayindir. Bioinspired optoelectronic nose with nanostructured wavelength-scalable hollow-core infrared fibers. *Advanced Materials*, 23(10):1263–+, 2011.

[73] T.M. Freeman and W.R. Seitz. Chemiluminescence fiber optic probe for hydrogen peroxide based on the luminol reaction. *Analytical Chemistry*, 50(9):1242–46, 1978.

[74] T.A. Dickinson, J. White, J.S. Kauer, and D.R. Walt. A chemical-detecting system based on a cross-reactive optical sensor array. *Nature*, 382(6593):697–700, 1996.

[75] S. Smolka, M. Barth, and O. Benson. Highly efficient fluorescence sensing with hollow core photonic crystal fibers. *Optics Express*, 15(20):12783–12791, 2007.

[76] S. Afshar V, S.C. Warren-Smith, and T.M. Monro. Enhancement of fluorescence-based sensing using microstructured optical fibres. *Optics Express*, 15(26):17891–17901, 2007.

[77] A.M. Stolyarov, A. Gumennik, W. McDaniel, O. Shapira, B. Schell, F. Sorin, K. Kuriki, G. Benoit, A. Rose, J.D. Joannopoulos, and Y. Fink. Enhanced chemiluminescent detection scheme for trace vapor sensing in pneumatically-tuned hollow core photonic bandgap fibers. *Optics Express*, 20(11):12407–12415, 2012.

[78] M.S. Meaney and V.L. McGuffin. Luminescence-based methods for sensing and detection of explosives. *Analytical and Bioanalytical Chemistry*, 391(7):2557–2576, 2008.

[79] R. Schulte-Ladbeck, M. Vogel, and U. Karst. Recent methods for the determination of peroxide-based explosives. *Analytical and Bioanalytical Chemistry*, 386(3):559–565, 2006.

[80] R.M. Burks and D.S. Hage. Current trends in the detection of peroxide-based explosives. *Analytical and Bioanalytical Chemistry*, 395(2):301–313, 2009.

[81] J.C. Sanchez and W.C. Trogler. Polymerization of a boronate-functionalized fluorophore by double transesterification: applications to fluorescence detection of hydrogen peroxide vapor. *Journal of Materials Chemistry*, 18(42):5134–5141, 2008.

[82] R. Deans, A. Rose, K.M. Bardon, L.F. Hancock, and T.M. Swager. Detection of explosives and other species. *U.S. Patent*, 7799573(B2), 2010.

[83] A.K. Bhatnagar, K.V. Reddy, and V. Srivastava. Optical energy gap of amorphous selenium - effect of annealing. *Journal of Physics D-Applied Physics*, 18(9):L149–L153, 1985.

[84] D.S. Deng, N.D. Orf, S. Danto, A.F. Abouraddy, J.D. Joannopoulos, and Y. Fink. Processing and properties of centimeter-long, in-fiber, crystalline-selenium filaments. *Applied Physics Letters*, 96(2), 2010. Abouraddy, Ayman/I-7963-2012.

[85] J.A. Lind and G.L. Kok. Henry law determinations for aqueous-solutions of hydrogen-peroxide, methylhydroperoxide, and peroxyacetic acid. *Journal of Geophysical Research-Atmospheres*, 91(D7):7889–7895, 1986.

[86] J. Gamelin, A. Aguirre, A. Maurudis, F. Huang, D. Castillo, L.V. Wang, and Q. Zhu. Curved array photoacoustic tomographic system for small animal imaging. *Journal of biomedical optics*, 13(2):024007, 2008.

[87] L.A. Cornejo, B. Jadidian, A.A. Winde, and A. Safari. Large-area flexible-array piezoelectric ceramic/polymer composite transducer for bone healing acceleration. *Applications of Ferroelectrics, 11th IEEE Symposium, 1998*, pages 0–4, 1998.

[88] G.T. Clement, J. White, and K. Hynynen. Investigation of a large-area phased array for focused ultrasound surgery through the skull. *Physics in medicine and biology*, 1071, 2000.

[89] B.M. Howe, Y. Chao, P. Arabshahi, S. Roy, T. Mcginnis, and A. Gray. A Smart Sensor Web for Ocean Observation: Fixed and Mobile Platforms, Integrated Acoustics, Satellites and Predictive Modeling. *IEEE Journal Of Selected Topics In Applied Earth Observations And Remote Sensing*, 3(4):507–521, 2010.

[90] E. Fukada. History and recent progress in piezoelectric polymers. *Transactions on ultrasonics, ferroelectrics, and frequency control*, 47(6):1277–1290, 2000.

[91] O. Oralkan, A.S. Ergun, J.A. Johnson, M. Karaman, U. Demirci, K. Kaviani, T.H. Lee, and B.T. Khuri-Yakub. Capacitive micromachined ultrasonic transducers: Next-generation arrays for acoustic imaging? *Ieee Transactions on Ultrasonics Ferroelectrics and Frequency Control*, 49(11):1596–1610, 2002.

[92] J. Chen. Capacitive micromachined ultrasonic transducer arrays for minimally invasive medical ultrasound. *Journal of Micromechanics and Microengineering*, 20(2), 2010.

[93] E. Flint, C. Liang, and A.C. Rogers. Power flow analysis of piezoelectric stack active members. *Proceedings of the 2nd International Conference on Intelligent Materials*, pages 534–545, 1994.

[94] K. Kimura and H. Ohigashi. Ferroelectric properties of poly (vinylidenefluoride-trifluoroethylene) co-polymer thin-films. *Applied Physics Letters*, 43(9):834–836, 1983.

[95] V. Giurgiutiu and S.E. Lyshevski. *Introduction to Mechatronic Systems.* Micromechatronics: Modeling, Analysis, and Design with Matlab, Second Edition. 2009.

[96] T. Furukawa. Ferroelectric properties of vinylidene fluoride copolymers. *Phase Transitions*, 18(3-4):143–211, 1989.

[97] N.C. Das, T.K. Chaki, and D. Khastgir. Effect of axial stretching on electrical resistivity of short carbon fibre and carbon black filled conductive rubber composites. *Polymer International*, 51(2):156–163, 2002.

[98] *Carbon Black–Polymer Composites: The Physics of Electrically Conducting Composites* edited by H. Kawamoto and E.K. Sichel (Marcel Dekker New York). pages 135–162, 1982.

[99] R. Gregorio and E.M. Ueno. Effect of crystalline phase, orientation and temperature on the dielectric properties of poly (vinylidene fluoride)(PVDF). *Journal of materials science*, 34(18):4489–4500, 1999.

[100] A. Ghatak. *Optics.* Tata McGraw-Hill Education. 2005.

[101] D.M. Rodgers. *M.Eng Thesis.* Massachusetts Institute of Technology. 2010.

[102] S.B. Lang and S. Muensit. Review of some lesser-known applications of piezoelectric and pyroelectric polymers. *Applied Physics A: Materials Science & Processing*, 85(2):125–134, September 2006.

[103] Q.X. Chen and P.A. Payne. Industrial applications of piezoelectric polymer transducers. *Measurement Science and Technology*, 6:249–267, 1995.

[104] J.Y. Song, Y.Y. Wang, and C.C. Wan. Review of gel-type polymer electrolytes for lithium-ion batteries. *Journal of Power Sources*, 77(2):183–197, February 1999.

[105] N. Fujitsuka, J. Sakata, Y. Miyachi, K. Mizuno, K. Ohtsuka, Y. Taga, and O. Tabata. Monolithic pyroelectric infrared image sensor using PVDF thin film. *Sensors and Actuators A: Physical*, 66(1-3):237–243, April 1998.

[106] J. Faucheu, K.A. Wood, L.P. Sung, and J.W. Martin. Relating gloss loss to topographical features of a PVDF coating. *JCT Research*, 3(1):29–39, 2006.

[107] P. Matsudaira. Sequence from picomole quantities of proteins electroblotted onto polyvinylidene difluoride membranes. *The Journal of biological chemistry*, 262(21):10035–8, July 1987.

[108] T. R. Jow and P. J. Cygan. Dielectric breakdown of polyvinylidene fluoride and its comparisons with other polymers. *Journal of Applied Physics*, 73(10):5147, 1993.

[109] P. Barber, S. Balasubramanian, Y. Anguchamy, S. Gong, A. Wibowo, H. Gao, H.J. Ploehn, and H.-C. zur Loye. *Polymer Composite and Nanocomposite Dielectric Materials for Pulse Power Energy Storage*, volume 2. October 2009.

[110] B. Chu, X. Zhou, K. Ren, B. Neese, M. Lin, Q. Wang, F. Bauer, and Q. M. Zhang. A dielectric polymer with high electric energy density and fast discharge speed. *Science*, 313(5785):334–6, July 2006.

[111] K.I. Arshak, D. McDonagh, and M.A. Durcan. Development of new capacitive strain sensors based on thick film polymer and cermet technologies. *Sensors and Actuators A: Physical*, 79(2):102–114, February 2000.

[112] K. Arshak, D. Morris, A. Arshak, O. Korostynska, and K. Kaneswaran. Investigation into the pressure sensing properties of PVDF and PVB thick film capacitors. *29th International Spring Seminar on Electronics Technology*, pages 334–339, May 2006.

[113] J.F. Gu, S. Gorgutsa, and M. Skorobogatiy. Soft capacitor fibers for electronic textiles. *Applied Physics Letters*, 97(13):133305, 2010.

[114] J.F. Gu, S. Gorgutsa, and M. Skorobogatiy. Soft capacitor fibers using conductive polymers for electronic textiles. *Smart Materials and Structures*, 19(11):115006, November 2010.

[115] *Modern Fluoropolymers* edited by D.A. Seiler and J. Scheirs (Wiley New York). pages 487–506, 1997.

[116] A.M. Stolyarov, L. Wei, F. Sorin, G. Lestoquoy, J.D. Joannopoulos, and Y. Fink. Fabrication and characterization of fibers with built-in liquid crystal channels and electrodes for transverse incident-light modulation. *Applied Physics Letters*, 101(1):011108, 2012.

[117] R. Kotz and M. Carlen. Principles and applications of electrochemical capacitors. *Electrochimica Acta*, 45:2483–2498, 2000.

[118] Z.-M. Dang, Y.-H. Lin, and C.-W. Nan. Novel Ferroelectric Polymer Composites with High Dielectric Constants. *Advanced Materials*, 15(19):1625–1629, October 2003.

[119] M. Arbatti, X. Shan, and Z.-Y. Cheng. Ceramic–Polymer Composites with High Dielectric Constant. *Advanced Materials*, 19(10):1369–1372, May 2007.

[120] Q.M. Zhang, H. Li, M. Poh, F. Xia, Z.Y. Cheng, H. Xu, and C. Huang. An all-organic composite actuator material with a high dielectric constant. *Nature*, 419(September):284–287, 2002.

[121] H. Kishi, Y. Mizuno, and H. Chazono. Base-Metal Electrode-Multilayer Ceramic Capacitors: Past, Present and Future Perspectives. *Japanese Journal of Applied Physics*, 42(Part 1, No. 1):1–15, January 2003.

[122] D. Chrobak, N. Tymiak, A. Beaber, O. Ugurlu, W. Gerberich, and R. Nowak. Deconfinement leads to changes in the nanoscale plasticity of silicon. *Nature Nanotechnology*, 6(8):480–4, August 2011.

[123] J.H. Park, L. Gu, and G. von Maltzahn. Biodegradable luminescent porous silicon nanoparticles for in vivo applications. *Nature Materials*, 8(4):331–336, 2009.

[124] T. van Buuren, L. Dinh, L. Chase, W. Siekhaus, and L. Terminello. Changes in the Electronic Properties of Si Nanocrystals as a Function of Particle Size. *Physical Review Letters*, 80(17):3803–3806, April 1998.

[125] K. Taira and J. Nakata. Silicon cells: Catching rays. *Nature Photonics*, 4(9):602–603, September 2010.

[126] N.P. Rao, N. Tymiak, J. Blum, A. Neuman, H.J. Lee, S.L. Girshick, P.H. McMurry, and J. Heberlein. Hypersonic plasma particle deposition of nanostructured silicon and silicon carbide. *Journal of aerosol science*, 29(5/6):707–720, 1998.

[127] H. Kohno and S. Takeda. Self-organized chain of crystalline-silicon nanospheres. *Applied Physics Letters*, 73(21):3144, 1998.

[128] R. Fenollosa, F. Meseguer, and M. Tymczenko. Silicon Colloids: From Microcavities to Photonic Sponges. *Advanced Materials*, 20(1):95–98, January 2008.

[129] S.-C. Hung, S.-C. Shiu, C.-H. Chao, and C.-F. Lin. Fabrication of crystalline Si spheres with atomic-scale surface smoothness using homogenized KrF excimer laser reformation system. *Journal of Vacuum Science & Technology B: Microelectronics and Nanometer Structures*, 27(3):1156, 2009.

[130] D.E. Witter and J.D. Levine. Process for producing crystalline Silicon spheres, 1987.

[131] S. Shabahang, J.J. Kaufman, D.S. Deng, and A.F. Abouraddy. Observation of the Plateau-Rayleigh capillary instability in multi-material optical fibers. *Applied Physics Letters*, 99(16):161909, 2011.

[132] D.S. Deng, J.C. Nave, X. Liang, S.G. Johnson, and Y. Fink. Exploration of in-fiber nanostructures from capillary instability. *Optics Express*, 19(17):219–222, 2011.

[133] Lord Rayleigh. On the stability of jets. *Proceedings of the London Mathematical Society*, 10:4–13, 1878.

[134] S. Tomotika. On the Instability of a Cylindrical Thread of a Viscous Liquid Surrounded by Another Viscous Fluid. *Proceedings of the Royal Society A: Mathematical, Physical and Engineering Sciences*, 150(870):322–337, June 1935.

[135] X. Liang, D. S. Deng, J. C. Nave, and Steven G. Johnson. Linear stability analysis of capillary instabilities for concentric cylindrical shells. *Journal of Fluid Mechanics*, 683:235–262, 2011.

[136] J. Ballato, T. Hawkins, P. Foy, R. Stolen, B. Kokuoz, M. Ellison, C. McMillen, J. Reppert, A.M. Rao, M. Daw, S.R. Sharma, R. Shori, O. Stafsudd, R.R. Rice, and D.R. Powers. Silicon optical fiber. *Optics Express*, 16(23):18675–83, November 2008.

[137] K. Dreyer and F. R. Hickey. The route to chaos in a dripping water faucet. *American Journal of Physics*, 59(7):619–627, 1991.

[138] R.F. Calahan, H. Leidecker, and G.D. Calahan. Chaotic rhythms of a dripping faucet. *Computers in Physics*, 4:368–382, 1990.

[139] Y. Sato, Y. Kameda, T. Nagasawa, T. Sakamoto, S. Moriguchi, T. Yamamura, and Y. Waseda. Viscosity of molten silicon and the factors affecting measurement. *Journal of Crystal Growth*, 249(3-4):404–415, March 2003.

[140] Robert H. Doremus. Viscosity of silica. *Journal of Applied Physics*, 92(12):7619, 2002.

[141] M. Born and E. Wolf. *Interference and Diffraction of Light.* 1990.

[142] T. Tanaka and S. Yamamoto. Comparison of aberration between axicon and lens. *Optics Communications*, 184(1-4):113–118, 2000.

[143] J.C. Jr Mikkelsen. The diffusivity and solubility of oxygen in silicon. *Materials Research Society Symposium Proceedings*, 59:19–30, 1986.

[144] H. Okamoto. O-si (oxygen-silicon). *Journal of Phase Equilibria and Diffusion*, 28(3):309–310, 2007.

[145] J. Ni and E. Arnold. Electrical-conductivity of semi-insulating polycrystalline silicon and its dependence upon oxygen-content. *Applied Physics Letters*, 39(7):554–556, 1981.

[146] S. Lombardo and S.U. Campisano. Electrical and structural properties of semi-insulating polycrystalline silicon thin films. *Physical Review B*, 47:561–567, 1993.

[147] P. Bruesch, T. Stockmeier, F. Stucki, and P.A. Buffat. Physical-properties of semiinsulating polycrystalline silicon .1. structure, electronic-properties, and electrical-conductivity. *Journal of Applied Physics*, 73(11):7677–7689, 1993.

[148] T.K. Sham, S.J. Naftel, P.S.G. Kim, R. Sammynaiken, Y.H. Tang, I. Coulthard, A. Moewes, J.W. Freeland, Y.F. Hu, and S.T. Lee. Electronic structure and optical properties of silicon nanowires: A study using x-ray excited optical luminescence and x-ray emission spectroscopy. *Physical Review B*, 70(4), 2004.

[149] M. Nishimura, S. Yoshino, H. Motoura, S. Shimura, T. McHedlidze, and T. Hikone. The direct observation of grown-in laser scattering tomography defects in czochralski silicon. *Journal of the Electrochemical Society*, 143(10):L243–L246, 1996.

[150] R.A.B. Devine, D. Mathiot, and W.L. Warren. *Proceedings of the Third International Symposium on the Physics and Chemistry of SiO2 and Si-SiO2 Interface*, 1996.

[151] G. B. Ghislotti. *Proceedings of the Third International Symposium on the Physics and Chemistry of SiO2 and Si-SiO2 Interface*, 1996.

[152] M Hutchings, F. Morgan, M. Ritoré, and A. Ros. Proof of the double bubble conjecture. *Annals of Mathematics*, 6(00):45–49, 2002.

[153] J. Ballato, T. Hawkins, P. Foy, B. Yazgan-Kokuoz, C. McMillen, L. Burka, S. Morris, R. Stolen, and R. Rice. Advancements in semiconductor core optical fiber. *Optical Fiber Technology*, 16(6):399–408, December 2010.

[154] U. C. Paek and R. B. Runk. Physical behavior of neck-down region during furnace drawing of silica fibers. *Journal of Applied Physics*, 49(8):4417–4422, 1978.

[155] D. H. Smithgall. Application of optimization theory to the control of the optical fiber drawing process. *Bell System Technical Journal*, 58(6):1425 1435, 1979.

[156] S. R. Choudhury and Y. Jaluria. Practical aspects in the drawing of an optical fiber. *Journal of Materials Research*, 13(2):483–493, 1998.

[157] P. Kroll and H.J. Schulte. Nano-sized crystals of silicon embedded in silica glass: large scale models and aspects of the electronic structure. *Materials Research Society Symposium Proceedings*, 958:0958–L07–16, 2007.

[158] I. Fisher and M. Eizenberg. Copper ion diffusion in porous and nonporous SiO2-based dielectrics using bias thermal stress and thermal stress tests. *Thin Solid Films*, 516(12):4111–4121, April 2008.